Lawrence Berkeley National Laboratory

Title
EXPERIMENTAL STUDY OF A CHEMICALLY REACTING TURBULENT BOUNDARY LAYER

Permalink
https://escholarship.org/uc/item/8q38j7nn

Author
Ng, T-M T.

Publication Date
1981-09-01

Lawrence Berkeley Laboratory
UNIVERSITY OF CALIFORNIA

ENERGY & ENVIRONMENT DIVISION
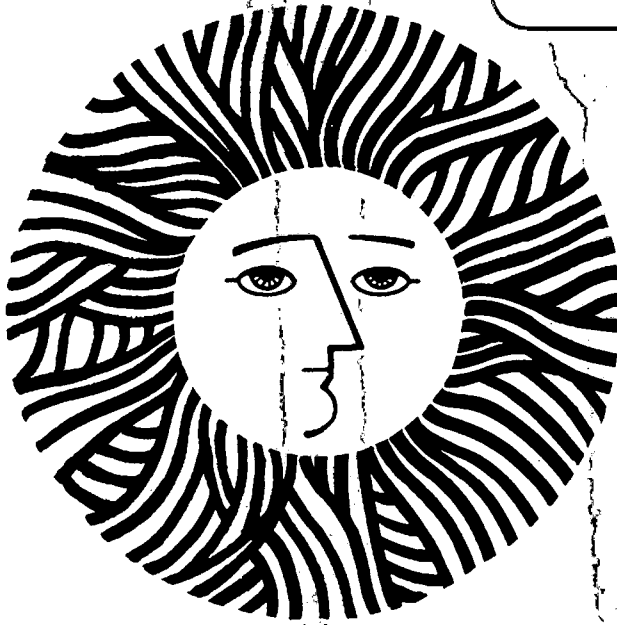
EXPERIMENTAL STUDY OF A CHEMICALLY REACTING
TURBULENT BOUNDARY LAYER

Tsun-Ming Terry Ng
(Ph.D. thesis)

September 1981

DISCLAIMER

EXPERIMENTAL STUDY OF A CHEMICALLY REACTING

TURBULENT BOUNDARY LAYER

Tsun-Ming Terry Ng

Ph.D. Thesis

September 1981

Energy and Environment Division
Lawrence Berkeley Laboratory
University of California
Berkeley, CA 94720

EXPERIMENTAL STUDY OF A CHEMICALLY REACTING
TURBULENT BOUNDARY LAYER

by

Tsun-Ming Terry Ng

ABSTRACT

Effects of a strong stepwise temperature rise and exothermic chemical reaction on the turbulent boundary layer over a flat plate were studied. The free stream velocity was fixed at 10.7 m/s and the wall temperature was set at about 1250°K. The Reynolds number based on the displacement thickness at the point of thermal discontinuity is about 900. For the reacting flow, ethylene-air mixture with equivalent ratio of 0.35 was used. High-speed Schlieren photography was used for visualization of the boundary layer thermal structures. Mean and rms density distributions were obtained from Rayleigh scattering intensity measurements. Mean and rms velocity distribution and some important fluctuation correlations were derived from single-component laser Doppler velocimetry measurements.

Strong wall-heating causes the expansion of the heat-affected region near the surface and pushes the rest of the boundary layer upwards. The boundary layer thickness, the displacement thickness, the momentum thickness, and the friction coefficient are increased by the wall-heating. The Reynolds stress is reduced due to the density decrease. The diffusion pattern of turbulent kinetic energy near the surface is altered, causing a partial failure of the boundary layer

assumption near the thermal leading edge. The rate of production of turbulent kinetic energy by Reynolds stress remains almost unchanged.

For the reacting boundary layer, the Schlieren pictures indicate that there is significant fluid heating and surface reaction before the formation of discrete flame structures. The boundary layer thickness, the displacement thickness, the momentum thickness, and the friction coefficient are increased. Differences in structures of the reaction zones near the leading edge and locations farther downstream cause different statistical behaviors to be observed. The turbulent kinetic energy diffusion pattern is altered significantly, causing the partial failure of the boundary layer assumption near the leading edge. The kinetic energy production by Reynolds stress is greatly reduced, indicating that the production mechanism is disrupted by the vigorous fluid expansion.

Chairperson, Thesis Committee

September 1981

ACKNOWLEDGEMENTS

TABLE OF CONTENTS

LIST OF FIGURES AND TABLES

NOMENCLATURE

C_f	Friction coefficient
C_p	Specific heat
D	Initial laser beam waist diameter
d	Beam waist diameter at the probe volume
d_f	Fringe spacing
d_x	Dimension of the minor axis of the LDV probe volume parallel to the intersecting plane
d_y	Dimension of the minor axis of the LDV probe volume normal to the intersecting plane
d_z	Dimension of the major axis of the LDV probe volume
f	Focal length
F_c	Flatness factor of the quantity c
h	Enthalpy
I	Intensity of the incident light
I_b	Background radiation
I_N	Noise signal
I_P	Uncorrected photomultiplier signal
I_R	Rayleigh scattering intensity
K	Thermal conductivity
k	Turbulent kinetic energy per unit mass
k_1	$u'^2 + v'^2$
ℓ_m	Mixing length
N	Total number of samples taken
n	Total number density
n_i	Number density of species i
P	Probability

q	Total heat transfer
Re	Reynolds number
R_{uv}	Correlation coefficient between u' and v'
S_c	Skewness factor of the quantity c
S_t	Stanton number
T	Temperature
t	Time
u	Streamwise velocity component
U_p	Particle velocity component normal to the LDV fringes
u_i	Velocity component in the i-direction
v	Velocity component in the y-direction
w	Mean molecular weight
x	Streamwise direction
y	Direction vertical to the surface
z	Horizontal cross-stream direction
Δt	Total sampling time
δ	Velocity boundary layer thickness
δ_1	Displacement thickness
δ_2	Momentum thickness
δ_T	Thermal boundary layer thickness
δ_{T_1}	Enthalpy thickness
δt	Sampling period
n_i	Refractive index of species i
θ	Angle
λ	Wavelength
μ	Viscosity

μ_i Mole fraction of species i

ν Frequency

ρ Gas density

σ_{Ri} Rayleigh scattering cross-section of species i

σ^+ Normalized Rayleigh scattering cross-section

τ Total stress

τ_t Non-dimensional Reynolds stress

ϕ Equivalence ratio

Subscripts

o   Reference condition

w   Wall condition

Superscripts

—   Average

'   Fluctuation

^   Root-mean-square

1. INTRODUCTION

The initiation and substantiation of a chemical reaction in a boundary layer is a fundamental problem in combustion. Some practical situations in which this problem is encountered are the auto-ignition of a combustible mixture by a hot surface, the preignition of fuel-air mixture by hot spots in an engine, and combustion on a catalytic surface. Works on this subject have shown cool flames as the first stage of a two-stage ignition process. One of the first studies of a reacting laminar boundary layer was by Toong (1956). Recent studies have been made by Schefer et al. (1980), Cairne et al. (1981), Chen and Faeth (1981), and Wang et al. (1981). Studies of reacting turbulent boundary layers are rare; one is by Cheng et al. (1980).

Statistical methods have been and still are the major means dealing with turbulent flow problems. One drawback of the statistical approach is the problem of closure of the governing equations because of statistical correlations which arise in time-averaging the conservation equations. To deal with this problem, many turbulence modelling methods have been proposed over the years. The subject is discussed in detail by Launder and Spalding (1972) and reviewed by Reynolds (1976). One of the first mathematical models is Prandtl's mixing-length hypothesis. The success of the hypothesis lies in its simplicity; however, its applicability is limited. More complex, although not necessarily better, computational schemes based on the governing partial differential equations have since been developed. Most of these schemes are in reality semi-empirical methods in the sense that experimental data are required in modelling various statistical correlations in the governing equations. Although various

degrees of success have been achieved in some specific flow problems, no universally applicable turbulence model has yet been developed, and the study of turbulent flows still has to rely very much on experimental approaches.

Most earlier experimental studies of the turbulent boundary layer are limited to measurements of statistical quantities, with emphasis on the distribution of the Reynolds stress and the transportation of turbulent kinetic energy. Statistical measurements tend to conceal the physics of the process involved; until recently, there was little knowledge about the physical structure of a turbulent boundary layer. One of the first observations on the turbulent boundary layer was that it can be divided into different regions by considering the relative importance of viscous and turbulent shears. This observation eventually led to the derivation of the highly successful "law of the wall". More detailed information about the turbulent boundary layer structure has been obtained in recent years due to advances in optical techniques. The visual study of the boundary layer over a flat plate by Kline et al. (1967) revealed the presence of well-organized, large-scale turbulent structures termed "bursts". The bursting phenomenon is a localized, three-dimensional, intermittently occurring event. Its origin and the detail of its internal pattern are not yet well understood. It is generally described as a horseshoe-shaped vortex with a complex internal velocity field. Carino and Brodkey (1969) and Kim et al. (1971) find that bursting is responsible for most of the turbulent kinetic energy production and a large portion of the Reynolds stress near the wall. The turbulent boundary layer is now thought to have large-scale, organized structures superimposed on relatively random background turbulence. A review on the subject of

turbulent boundary layer structures is given by Willmarth (1975).

Although considerable understanding of the turbulent boundary layer has been obtained, the effect of density change and large heat release on its structure is still largely unknown, due mainly to the lack of suitable experimental techniques. Hot-wire anemometry, which is invaluable in turbulent studies, is applicable only to low or moderate-temperature flows. Until very recently reliable data for high-temperature and combusting flows were virtually unavailable. Recent developments of several advanced optical techniques, like laser Doppler velocimetry (LDV) and Rayleigh scattering measurement, have greatly alleviated this problem. The non-intrusive nature of these techniques and their fast response time make them particularly suitable for turbulent combustion studies. To give a few examples, LDV had been used by Rask (1979) in an internal combustion engine, Gouebet et al. (1979) in a high temperature plasma, Cheng et al. (1980) in a reacting boundary layer, and Pitz (1981) in a reacting shear layer, while Rayleigh scattering measurements had been performed by Rambach et al. (1979) in turbulent diffusion flames and Bill et al. (1981) in a V-shaped flame.

The primary objectives of the present work are:

(1) to study the structure of an isothermal turbulent boundary layer flow over a flat plate;

(2) to study the effect of relatively regular and "organized" fluid expansion caused by a large stepwise temperature rise on the turbulent boundary layer; and

(3) to study the effect of vigorous and relatively random combustion heat release and the resulting fluid expansion on the flat-plate boundary layer.

To attain these objectives, the following were carried out:

(1) High-speed Schlieren photography was used to visualize the over-all structure of the heated and the reacting turbulent boundary layer.

(2) The mean and the root-mean-square (rms) fluid density distributions were deduced from Rayleigh scattering measurements. The probability density function and the spectral distribution were also obtained.

(3) A single-component LDV was used to measure the mean velocity, the rms velocity, the Reynolds stress, and several important velocity correlations. The probability density function and the spectral distribution of the streamwise velocity were obtained.

2. THE COMBUSTOR

The combustion flow was produced by a low-speed wind tunnel with square cross-section, a fuel-air supply and a mixing system as shown in Fig. 1. Primary air was supplied by a constant-speed blower and was filtered before it entered the wind tunnel. The air flow rate was regulated by a damper and metered by a calibrated square-edged orifice. In using laser Doppler velocimetry for velocity measurements, secondary air was needed for the particle seeder. The secondary air was supplied by a compressed-air line and was measured by a Matheson 605 rotameter. When using the Rayleigh scattering technique for density measurements, the secondary air bypassed the particle generator and was fed directly into the main flow. The fuel (C_2H_4) was supplied by two high-pressure fuel tanks and regulated by pressure regulators. Electric heating tapes were wrapped around the regulators to warm up the fuel in order to prevent water vapor condensation. The fuel flow rate was measured by a Fischer and Porter 10A3500 flow meter. A manifold was used to separate the fuel into four streams prior to entering the fuel-air mixing section. In the mixing section, shown in Fig. 2, each fuel stream was fed into a separate fuel distributor made up of a 3/4 in. diameter tube with six evenly spaced 1/8 in. diameter outlets directly counter to the main air flow. The resulting vigorous fluid motion ensured that the fuel and air were thoroughly mixed before they entered the wind tunnel.

Detailed dimensions of the wind tunnel are given in Fig. 3. The gas mixture from the flow system entered a 60 cm cubic stagnation chamber with a #50-mesh wire screen partition in the middle. The chamber was connected to a nozzle which reduced the cross-section elliptically to a 10 cm square

outlet over a distance of 100 cm. A 25 cm long sand-rough aluminum plate was placed at the exit to ensure the transition to turbulent of the boundary layer. The rough plate was then attached to a 25 cm long smooth aluminum plate with internal water cooling to prevent the gas from heating up before it reached the heating section that followed. The two aluminum plates were enclosed by metal walls to minimize ambient disturbance while the heating section was left unenclosed for easy accessibility by various instrumentations. The exhaust gases passed directly into an 8 in. square exhaust duct.

The heating section was made up of a 25.4 cm long ceramic block, shown in Fig. 4, and nine separate heating strips. The ceramic block had a 2° peak at the middle to enable Rayleigh scattering measurement close to the wall (the two aluminum plates upstream also had matching 2° peaks at the center). For Rayleigh scattering measurements close to the wall, background scattering from the heating section surface could have been a severe problem. The 2° peak down the middle of the heating section effectively shadowed the second half of the surface of the section from the laser beam, thus greatly reducing the background scattering in this region. Hence density measurements in this study were carried out by moving the Rayleigh scattering measurement slightly off center into this shadowed region. The surface of the ceramic block was separated into nine evenly spaced 25.4 cm sections by 2.54 mm wide, .25 mm high partitions. Details of the heating strips' design are shown in Fig. 5. The heating strips were made of 25.4 cm wide, .127 mm thick Kanthal A-1 alloy. All the strips were heated electrically and individually to give an approximately even wall temperature. Each strip was kept in tension by springs connected to its ends to ensure that it lay flat against the ceramic block

surface. The electric contact blocks and sections of the heating strip outside the main gas flow were air-cooled to prevent overheating.

Figure 6 depicts the coordinate system used. The center of the leading edge of the heating section was designated as the origin. Direction downstream was denoted as x, upward from the surface as y, and across the surface as z, following the right-hand rule.

The wind tunnel was placed on a three-dimensional traversing mechanism driven by a computer-controlled stepping motor system. The position in the x-direction was measured by a scale with resolution of 1 mm. Positions in the y and z directions were measured by dial gauges with resolution of 0.1 mm. Computer-controlled traversing enabled rapid scanning of the test section by various diagnostic techniques.

3. EXPERIMENTAL TECHNIQUES

Due to the hostile nature of the combustion environment and the required high-frequency response for turbulent measurements, applications of many conventional techniques, like hot-wire anemometry and thermo-coupling, are difficult if not impossible. Recent advances in some optical techniques have made many conventional techniques obsolete. Optical techniques in general can offer the advantages of high frequency response, non-intrusion, and small sensing volume.

In this study, several optical techniques were adopted. High-speed Schlieren photography was used for visualization of the boundary layer flow structures. Density distributions were measured using Rayleigh scattering. Velocity distributions and correlations were measured using laser Doppler velocimetry (LDV).

3.1 Schlieren System

The well-known Schlieren method is based on the phenomenon that light passing through a density gradient in a fluid is deflected as if it were passing through a prism. A detailed discussion of the basic principles are available in Shapiro (1953).

A schematic of the experimental setup is shown in Fig. 7. A Spectra Physics Model 164 4-watt argon-ion laser was used as the light source (λ = 488 nm). A neutral density filter was placed in front of the laser to reduce the light intensity to the desired level. An 18 mm and a 1.0 m focal length lens were used to collimate the laser light into a field of parallel beams over the test section. A second 1.0 m focal length lens was used to focus the image of the test section onto a

Fastax WF-17 16 mm high-speed camera capable of operating up to 8000 frames/sec. In this study, a speed of about 3000 frames/sec was used. A knife edge was placed at the focal point of the second 1.0 m focal length lens to block off part of the deflected light and to produce a Schlieren image. No attempt was made to obtain quantitative measurement from the picture; rather the technique was used for flow visualization and qualitative assessment of the turbulent structure.

3.2 Rayleigh Scattering System

Rayleigh scattering is the elastic scattering (wavelength of the light remains unchanged) of light by particles whose sizes are small compared with the wavelength of the incident light. This technique for density measurement has been applied by Pitz et al. (1976) in a premixed hydrogen-air flame, Rambach et al. (1979) in turbulent diffusion flames, Bill et al. (1981) in a V-shaped turbulent flame, and Cheng et al. (1980) in a turbulent boundary layer. The Rayleigh scattering technique offers the major advantages of nonintrusion, small probe volume, and high frequency response. Compared with the widely used Raman scattering technique, Rayleigh scattering has the advantage of a much higher scattering intensity since the Rayleigh scattering cross-section is about 100 times larger. A discussion of the signal-to-noise ratio of Rayleigh scattering and comparison with Raman scattering are given by Robben (1975).

3.2.1 *Basic Principle*

The Rayleigh scattering cross-section σ_{Ri} of species i is given by (Robben, 1975)

$$\sigma_{Ri} = \frac{4\pi^2}{\lambda^4} \left(\frac{n_i - 1}{n_i}\right)^2 \sin^2\theta \qquad (3.1)$$

where λ = wavelength of incident light

n_i = index of refraction of species i

n_i = no. density of species i

θ = direction of scattering as measured from the E vector of the incident radiation.

The total scattered signal is given by (Robben, 1975)

$$I_R = K I n \sum_i \mu_i \sigma_{Ri} \qquad (3.2)$$

where   K = constant for given optical arrangement

I = intensity of the incident light

n = total no. density

μ_i = mole fraction of species i

If the Rayleigh scattering of a certain reference condition, denoted by subscript o, is known, the ratio of the instantaneous scattering intensity to the reference intensity is given by

$$I_R/I_{Ro} = n \sum_i \mu_i \sigma_{Ri} / n_0 \left(\sum_i \mu_i \sigma_{Ri}\right)_0 \qquad (3.3)$$

By definition

$$n = \rho/w \qquad (3.4)$$

where ρ = gas density

w = mean molecular weight

Substituting Eq. 3.4 into 3.3, one gets

$$\frac{I_R}{I_{Ro}} = \frac{\rho}{\rho_o} \sigma^+ \qquad (3.5)$$

where

$$\sigma^+ = \frac{w_o}{w} \frac{\sum_i \mu_i \sigma_{Ri}}{(\sum_i \mu_i \sigma_{Ri})_o}$$

From the equation above, it is obvious that the Rayleigh scattering intensity ratio depends on both the gas density and composition. However, calculations by Namer et al. (1980) indicate that for many hydrocarbon fuel-air mixtures, the value of σ^+ is close to 1 regardless of the degree of reaction. Hence it is possible to make the following approximation:

$$\frac{I_R}{I_{Ro}} \simeq \frac{\rho}{\rho_o} \qquad (3.6)$$

The accuracy of this approximation is particularly good for low equivalent ratio fuel-air mixtures since major portions of the gas mixture are nitrogen and unreacted oxygen which do not participate directly in the chemical process.

3.2.2 Experimental Setup

A schematic of the Rayleigh scattering system is shown in Fig. 8. A Spectra Physics 164 4-watt argon-ion laser was used as the light source. The waist diameter, defined at $1/e^2$ times the peak intensity, of the beam ($\lambda = 488$ nm) coming out of the laser is 1.2 mm. A 18 mm focal length lens and a 120 mm focal length lens were combined to form a lens system to focus the laser beam to a waist diameter of about 100 μ.* A 55 mm

---

*The theoretical value of the waist diameter is about 30 μm. Aberrations in the lenses cause the higher actual value.

f1.2 lens was used to collect the scattering at 90° from the beam direction. Two slits, one 1 mm in width and oriented at 90° to the beam, and the other 100 μm wide and parallel to the beam, were placed on top of each other to form a rectangular window. The window was placed behind the collecting lens such that its rectangular image was focused on the waist region of the laser beam. This in effect confined the sensing volume to a 1 mm long section centered about the beam waist. The collected light was filtered by a Melles Griot 03FIL005 3 nm band pass 488 nm interference filter placed behind the slits. The filtered light then fell onto a Hamamatsu 931A photomultiplier. The collecting optical system was fastened to a three-dimensional translational stage to enable easy focusing and movement.

As indicated in Fig. 9, the signal from the photomultiplier was first amplified by a Dymec 2461A dc amplifier and then digitized by a LPS 11 12-bit A/D converter. Measurements were made by using a PDP 11/10 computer and stored on 7-track magnetic tapes for post-processing. The corner frequency of the overall data-collecting system was about 5 KHz.

3.2.3 *Background Radiation and Noise*

The measurement of Rayleigh scattering intensity is complicated by the presence of background radiation and photomultiplier noise. Sources of background radiation are radiation from heated surfaces, the flame, room light, and reflection of stray light from solid surfaces. The photomultiplier noise is due to the statistical variations in photon arrival rates and general instrumentation noises. In interpreting Rayleigh scattering measurements, corrections for both have to be made.

The uncorrected photomultiplier signal, I_p, represents the sum of

Rayleigh scattering signal, I_R, noise signal I_N, and background radiation sign, I_b; i.e.

$$I_p = I_R + I_N + I_b \qquad (3.7)$$

To correct for background radiation at a given location, intensity measurements at distances of $\pm$ .5 mm away from the center of the laser beam were taken (see Fig. 8). By assuming a linear distribution, an estimation of the average background, intensity, $\overline{I}_b$, was obtained. The average Rayleigh scattering signal was then obtained by

$$\overline{I}_R = \overline{I}_p - \overline{I}_b - \overline{I}_N \qquad (3.8)$$

Since the mean, $\overline{I}_N$, of the noise signal is zero, Eq. 3.8 can be reduced to

$$\overline{I}_R \doteq \overline{I}_p - \overline{I}_b \qquad (3.9)$$

Average density ratio is then obtained as

$$\overline{\rho}/\overline{\rho}_0 = \overline{I}_R/\overline{I}_{Ro} \qquad (3.10)$$

Using the definition $I = \overline{I} + I'$, where superscript ' represents fluctuation, Eq. 3.7 can be expanded to

$$\overline{I}_p + I_p' = \overline{I}_R + \overline{I}_b + I_R' + I_b' + I_N' \qquad (3.11)$$

Squaring Eq. 3.11 and taking the average, and assuming that all the fluctuations are uncorrelated with each other, one obtains

$$\overline{I_P}^2 + \overline{I_P'}^2 = (\overline{I_R} + \overline{I_b})^2 + \overline{I_R'}^2 + \overline{I_b'}^2 + \overline{I_N'}^2 \qquad (3.12)$$

From Eq. 3.9, $\overline{I_P}^2 = (\overline{I_R} + \overline{I_b})^2$, hence Eq. 3.12 is further reduced to

$$\overline{I'_R}^2 = \overline{I'_P}^2 - \overline{I'_N}^2 - \overline{I'_b}^2 \qquad (3.13)$$

The mean square fluctuation of the background radiation can be calculated from the background radiation measurements. In most cases its value is small compared with $\overline{I'_P}^2$ and $\overline{I'_N}^2$ and can be neglected.

As a result of the Poisson distribution of the photoelectrons, the mean square fluctuation of the noise is proportional to the multiplier signal. For the experiments carried out in the present study, the conditions outside the boundary layer were chosen as the reference. Since there was no density fluctuation outside the boundary layer, the variance of I_{Ro} was due mainly to the photomultiplier noise, i.e.,

$$\overline{I'_{Po}}^2 = \overline{I'_{No}}^2 \qquad (3.14)$$

An estimation of $\overline{I'_N}^2$ was then given by

$$\overline{I'_N}^2 = \overline{I'_{Po}}^2 \cdot \overline{I_P}/\overline{I_{Po}} \qquad (3.15)$$

Combining Eq. 3.13 and 3.5 and neglecting $\overline{I'_b}^2$, one obtains

$$\overline{\rho'}^2 \propto \overline{I'_R}^2 \simeq \overline{I'_P}^2 - \overline{I'_{Po}}^2 \, \overline{I_P}/\overline{I_0} \qquad (3.16)$$

Hence the mean square fluctuation and mean density profiles can be obtained readily by the Rayleigh scattering technique.

3.3 Laser Doppler Velocimetry

Even since its first application to fluid velocity measurement in a laminar pipe flow by Yeh and Cummins (1964), laser Doppler velocimetry (LDV) has been widely used in various fluid mechanics and combustion experiments. This technique offers the advantages of non-intrusion, rapid frequency response, small sensing volume, and direct measurement of velocity rather than its inference from pressure (pitot tube) or heat-transfer coefficient (hot-wire) (Doebelin, 1975). In addition, LDV has the distinct advantage of being able to operate in hostile environments where conventional methods fail, making it particularly suitable for combustion studies.

LDV measurements in combustion environments have been performed by Rambach et al. (1979) in turbulent diffusion flames, Bill et al. (1981) and Cheng and Ng (1981) in V-shaped premixed turbulent flames, Cheng et al. (1980) in a reacting turbulent boundary layer, and Pitz (1981) in a combusting free shear layer. Despite many experimental difficulties, the results were satisfactory.

3.3.1 Operating Principles

LDV is based on the phenomena of Doppler shifting and light interference. When light from a monochromatic source is scattered by a particle moving relative to a fixed detector, the frequency of the scattered light received by the detector is Doppler-shifted by an amount

proportional to the particle velocity. Under normal circumstances, the shift is extremely small compared with the original light frequency and is difficult to measure directly. However, the Doppler shift can be measured if the scattered light is mixed with a coherent light of slightly different frequency. The two waves interfere and a beam of frequency equal to the difference between the two light frequencies can be observed. Details of the basic principles of LDV are available in Mayo (1969), Drain (1980), Durst et al. (1976), Durrani (1977), and Stevenson (1977).

Basic LDV systems operate using one of the following configurations (Stevenson, 1977): (1) interference between scattered light from one laser beam with unscattered light from another beam (reference-beam LDV); (2) interference between scattered light from two laser beams (differential LDV); and (3) interference between scattered light from a single beam in two different directions (single-beam LDV). Drain (1972) has shown that for gas flow measurements, the differential LDV system tends to have a better signal-to-noise ratio (SNR) than the reference-beam system. Hence the dual-beam, real fringe, differential LDV system was chosen for this study.

In a typical dual-beam differential LDV (Fig. 10), a laser beam is split into two parallel beams by a beam splitter. The two beams are focused by a lens to intersect and form the LDV probe volume. Seeding the fluid with particles is usually required to provide sufficient scattered particles for satisfactory measurement. To provide a conceptual basis for both qualitative and quantitative analysis of LDV, Rudd (1969) proposed an interference fringe model (Fig. 11). When two coherent beams having plane wavefronts intersect at an angle θ, a pattern of planar fringes is formed by interference. The fringe spacing, d_f, is determined

by the wavelength, λ, and the intersecting angle, θ, as follows:

$$d_f = \lambda/2 \sin (\theta/2) \qquad (3.17)$$

As a particle moves through the fringes, the scattered light will also show a similar intensity fluctuation. By measuring the frequency, ν, of the fluctuation, the particle velocity component (U_p) normal to the fringes is given by

$$U_p = \nu \cdot d_f \qquad (3.18)$$

A more complete picture of the LDV system is obtained when the real fringe characterization is combined with the Gaussian radial intensity distribution of the interfering beams. The effective probe volume, defined at $1/e^2$ of the peak intensity, is found to be ellipsoidal in shape. The probe volume dimensions (Fig. 11) are given by Stevenson, (1977)

$$d_x = d/\sqrt{2} \cos (\theta/2)$$
$$d_y = d/\sqrt{2} \qquad (3.19)$$
$$d_z = d/\sqrt{2} \sin (\theta/2)$$

where d_z is the dimension of the major axis, d_x is the dimension of the minor axis in the intersection plane, and d_y is the dimension of the minor axis normal to the intersecting plane. The waist diameter, d, is given by

$$d = 4\lambda f/\pi D \qquad (3.20)$$

where D is the original laser beam waist diameter defined at $1/e^2$ of the peak intensity.

Although the fringe model does not give a complete explanation of the physical processes involved in LDV, it gives an easily visualized picture of the system.

3.3.2 *Experimental Setup*

A schematic of the LDV system is shown in Fig. 10. The argon-ion laser operating at λ = 514.5 nm was used as the light source. The beam passed through a polarization rotator and a beam splitter to form two parallel beams 51 mm apart. The polarization rotator was adjusted to ensure that the split beams were of equal intensity. The beam splitter was fastened to a rotary stage for changing the orientation of the beam-intersecting plane. A 600 mm focal length lens focused the two parallel beams to form the LDV probe volume. Some important parameters of the LDV system are given in Table 1.

A 55 mm focal length, f1.2 lens was used to collect the forward-scattered light. A 514 nm interference filter with a 10 nm band pass was used to filter the collected light. The light then fell on a Hamamatsu 931A photomultiplier.

A cyclone particle producer, similar to the one developed by Glass and Kennedy (1977), was used as a particle seeder. Aluminum oxide polishing powder of .30 μm nominal diameter was used for seed particles.

As indicated in Fig. 9, signals from the photomultiplier were first amplified by a HP8477 AC amplifier with range from .1 to 400 MHz. The amplified signals then passed through a TSI 1984 input conditioner and a TSI 1990 frequency counter. The analog output of the frequency counter,

which is inversely proportional to the frequency of the detected bursts, were digitized and recorded by the LPS 11 laboratory peripheral system and PDP 11/10 computer. The raw data were stored on 7-track magnetic tapes for post-processing.

3.3.3 *Velocity Biasing and Correction*

In most LDV measurements, the Doppler frequency of every validated particle crossing the fringe pattern is recorded. The mean, $\bar{u}$, and mean square fluctuation velocity, $\overline{u'^2}$, are computed by ensemble averaging, i.e.,

$$\bar{u} = \sum^N n/N$$

$$\overline{u'^2} = \sum^N (u-\bar{u})^2 / N \tag{3.21a}$$

where N is the total number of samples taken. In turbulent combustion experiments, these averages are subject to biasing. The biasing can come from two sources:

1. The higher probability that high velocity particles have of crossing the probe volume than lower velocity ones results in biasing.

2. When an originally uniformly seeded fuel-air mixture is ignited, "patches" of low and high density fluid will appear in the flow. The lower density patches will have fewer particles per unit volume than the higher density ones. The lower probability of getting a validated sample from a lower density patch results in biasing.

Dimotakis (1976) suggested that in high data rate regimes, the biasing error could be corrected by time averaging the data, i.e.,

$$\overline{u} = \int u(t)dt/\Delta t$$

$$\overline{u'^2} = \int (u-\overline{u})^2 dt/\Delta t \tag{3.21b}$$

where t = time and Δt = total sampling time. This requires the simul-taneous recording of frequency data and time lapsed between consecutive validated samples.

Another method of correcting the biasing error, which has been used by Bill (1981), Cheng (1980), and Cheng and Ng (1981), is to treat the LDV data as continuous signals. This is permissible if the data valida-tion rate is sufficiently high for the turbulence level of the flow. A discrete time series of the velocity is obtained by sampling the LDV signal at a fixed, high sampling rate. Since the sampling period, δt, is small, the discrete time series can be integrated numerically to give good approximations of various time-averaged values:

$$\overline{u}_i = \sum_{i}^{N} u_i(t)/N = \sum_{i}^{N} u_i(t)\ t/N\ t$$

$$\simeq \int u(t)dt/\Delta t \tag{3.22a}$$

$$\overline{u'_i^2} = \sum_{i}^{N} (u_i-\overline{u}_i)^2/N = \sum_{i}^{N} (u_i-\overline{u}_i)^2 \delta t/N\ \delta t$$

$$\simeq \int (u_i-\overline{u}_i)^2 dt/\Delta t \tag{3.22b}$$

$$\overline{u'_i^3} = \sum_{i}^{N} (u_i-\overline{u}_i)^3/N = \sum_{i}^{N} (u_i-\overline{u}_i)^3 \delta t/N\ \delta t$$

$$\simeq \int (u_i-\overline{u}_i)^3 dt/\Delta t \tag{3.22c}$$

$$\overline{u'_i}^4 = \Sigma \ (u_i - \overline{u}_i)^4 / N = \Sigma \ (u_i - \overline{u}_i)^4 \delta t / N \ \delta t$$

$$\simeq \int (u_i - \overline{u}_i)^4 \delta t / \Delta t \tag{3.22d}$$

To obtain high data validation rates, the flow has to be heavily seeded. This sampling method was adopted in this study.

3.3.4 *Errors*

In addition to velocity biasing, there are other errors in LDV measurements. The most commonly mentioned ones are:

1. Transit time broadening

2. Optical errors

3. Fringe gradient broadening

4. Velocity-gradient broadening due to the existence of velocity gradient in the probe volume

5. Movement of probe volume due to presence of a refractive index gradient in the flow.

More detailed discussions of LDV measurement errors are available in Pitz (1981) and Buchhane et al. (1978). Most LDV errors and their corrections are still subjects of research. In this study, the errors which could be estimated were usually small and could be neglected.

3.3.5 *Measurements of Velocity Fluctuation Correlations*

If both velocity components, u, in the x-direction and v, in the y-direction, are measured instantaneously, all the correlations involving the velocity fluctuations, u' and v', can be evaluated. It requires a

two-component optical system and two frequency measurement units to record two frequency readings simultaneously. The procedures and apparatus involved are more complicated than single-component measurements. However, by relatively simple methods, some important velocity fluctuation correlations can be derived from single-component LDV measurements.

a. Measurements of $\bar{u}$, $\bar{v}$, $\overline{u'^2}$, $\overline{v'^2}$, and $\overline{u'v'}$

The procedure to measure $\overline{u'v'}$ using a single component LDV system is described by Durrani and Greated (1977). This technique has been used by Durst et al. (1980), Moreau and Boutier (1976), and Cheng and Ng (1981).

The velocity component u and two other components, u_1 and u_2, at angles of $\pm \theta$ relative to the x-axis are measured separately (see Fig. 12). It can be shown easily that

$$u_1 = u \cos\theta + v \sin\theta \qquad (3.23)$$

$$u_2 = u \cos\theta - v \sin\theta \qquad (3.24)$$

Using the definition $u_i = \bar{u}_i + u_i'$, where superscript ' denotes fluctuation and $^-$ denotes the mean, the following equations can be derived:

$$\overline{u_1} = \bar{u} \cos\theta + \bar{v} \sin\theta \qquad (3.25)$$

$$\overline{u_2} = \bar{u} \cos\theta - \bar{v} \sin\theta \qquad (3.26)$$

$$u_1' = u' \cos\theta + v' \sin\theta \qquad (3.27)$$

$$u_2' = u' \cos\theta - v' \sin\theta \qquad (3.28)$$

By evaluating $\overline{(3.27)^2} - \overline{(3.28)^2}$, one gets

$$\overline{u_1'^2} - \overline{u_2'^2} = 4\,\overline{u'v'}\,\cos\theta\,\sin\theta$$

or

$$\overline{u'v'} = (\overline{u_1'^2} - \overline{u_2'^2})/4\cos\theta\,\sin\theta \qquad (3.29)$$

Subtracting Eq. 3.26 from 3.25, one obtains

$$\overline{u_1} - \overline{u_2} = 2\,\overline{v}\,\sin\theta$$

or

$$\overline{v} = (\overline{u_1} - \overline{u_2})/2\sin\theta \qquad (3.30)$$

By evaluating $\overline{(3.27)^2} + \overline{(3.28)^2}$, the following is obtained

$$\overline{u_1'^2} + \overline{u_2'^2} = 2(\overline{u'^2}\cos^2\theta + \overline{v'^2}\sin^2\theta)$$

or

$$\overline{v'^2} = [(\overline{u_1'^2} + \overline{u_2'^2})/2 - \overline{u'^2}\cos^2\theta]/\sin^2\theta \qquad (3.31)$$

The values of $\overline{u}$ and $\overline{u'^2}$, $\overline{u_1}$ and $\overline{u_1'^2}$, and $\overline{u_2}$ and $\overline{u_2'^2}$ can be calculated from the corresponding LDV measurements (Eqs. 3.22a and 3.22b). With Eqs. 3.29, 3.30, and 3.31, $\overline{u}$, $\overline{v}$, $\overline{u'^2}$, $\overline{v'^2}$ and $\overline{u'v'}$ can be obtained readily.

b. Measurements of $\overline{u'v'^2}$ and $\overline{v'k_1}$

For convenience of discussion, define

$$k_1 = u'^2 + v'^2 \qquad (3.32)$$

By evaluating $\overline{(3.27)^3}$ and $\overline{(3.28)^3}$, these equations are obtained:

$$\overline{u_1'^3} = \overline{u'^3}\cos\theta + 3\overline{u'v'^2}\cos\theta\,\sin^2\theta + 3\overline{u'^2v'}\cos^2\theta\,\sin\theta$$
$$+ \overline{v'^3}\sin^3\theta \qquad (3.33)$$

$$\overline{u_2'^3} = \overline{u'^3}\cos^3\theta + 3\overline{u'v'^2}\cos\theta\,\sin^2\theta - 3\overline{u'^2v'}\cos^2\theta\,\sin\theta$$
$$- \overline{v'^3}\sin^3\theta \qquad (3.34)$$

Adding Eq. (3.33) and (3.34),

$$\overline{u_1'^3} + \overline{u_2'^3} = 2\overline{u'^3}\cos^3\theta + 6\overline{u'v'^2}\cos\theta\,\sin^2\theta$$

or $$\overline{u'v'^2} = (\overline{u_1'^3} + \overline{u_2'^3} - 2\overline{u'^3}\cos^3\theta)/6\cos\theta\,\sin^2\theta \qquad (3.35)$$

Subtracting Eq. (3.34) from (3.33),

$$\overline{u_1'^3} - \overline{u_2'^3} = 2\overline{v'^3}\sin^3\theta + 6\overline{v'u'^2}\cos^2\theta\,\sin\theta$$

If θ is chosen to be 60°, it can be shown that

$$\overline{v'k'} = (\overline{u_1'^3} - \overline{u_2'^3})/(3\sqrt{3}/4) \qquad (\theta=60°) \qquad (3.36)$$

Since $\overline{u'^3}$, $\overline{u_1'^3}$, and $\overline{u_2'^3}$ can be evaluated directly from LDV measurements (Eq. 3.22c), $\overline{u'v'^2}$ and $\overline{v'k'}$ can be calculated easily from Eqs. 3.35 and 3.36 respectively.

c. <u>Measurements of $\overline{u'v'(k_1)}$ and $\overline{v'^2 k_1}$</u>

By evaluating $\overline{(3.27)^4}$ and $\overline{(3.28)^4}$, the following are obtained:

$$\overline{u_1'^4} = \overline{u'^4} \cos^4\theta + 4 \overline{u'v'^3} \cos\theta \sin^3\theta + 6 \overline{u'^2v'^2} \cos^2\theta \sin^2\theta$$

$$+ 4 \overline{u'^3v'} \cos^3\theta \sin\theta + \overline{v'^4} \sin^4\theta \qquad (3.37)$$

$$\overline{u_2'^4} = \overline{u'^4} \cos^4\theta - 4 \overline{u'v'^3} \cos\theta \sin^3\theta + 6 \overline{u'^2v'^2} \cos^2\theta \sin^2\theta$$

$$- 4 \overline{u'^3v'} \cos^3\theta \sin\theta + \overline{v'^4} \sin^4\theta \qquad (3.38)$$

Subtracting Eq. 3.38 from 3.37, one gets

$$\overline{u_1'^4} - \overline{u_2'^4} = 8(\overline{u'v'^3} \cos\theta \sin^3\theta + \overline{u'^3v'} \cos^3\theta \sin\theta)$$

If θ is chosen to be 45°, i.e., $\cos\theta = \sin\theta = \sqrt{2}/2$, it can be shown that

$$\overline{u'v'k_1} = (\overline{u_1'^4} - \overline{u_2'^4})/2 \qquad (3.39)$$

Adding Eqs. 3.37 and 3.38, one obtains

$$\overline{u_1'^4} + \overline{u_2'^4} = 2 \overline{u'^4} \cos^4\theta \; 12 \overline{u'^2v'^2} \cos^2\theta \sin^2\theta + 2 \overline{v'^4} \sin^4\theta \quad (3.40$$

If θ is chosen to be 67.79°, i.e., $\tan^2\theta = 6$, then

$$\overline{v'^2k_1} = (\overline{u_1'^4} + \overline{u_2'^4} - 2 \overline{u'^4}/49)/(72/49) \qquad (3.41)$$

Values of $\overline{u'^4}$, $\overline{u_1'^4}$ and $\overline{u_2'^4}$ can be calculated directly from LDV measurements. Hence both $\overline{u'v'k_1}$ and $\overline{v'^2k_1}$ can be obtained readily from Eqs. 3.40 and 3.41.

4. RESULTS AND DISCUSSIONS

Density and velocity measurements were performed for three different cases: 1) boundary layer flow with no wall-heating; 2) boundary layer flow with severe wall-heating; and 3) reacting boundary layer flow. High-speed Schlieren motion pictures were taken for the latter two cases. The free stream velocity for all three cases was fixed at about 10.7 m/s. For cases 2 and 3, the wall temperature, T_w, was set at about 1250°K. For case 3, the equivalence ratio, ϕ, was 0.35. Reaction was initiated and sustained by continuous heating of the surface.

Data were taken at predetermined positions above the surface at several streamwise locations. In scanning the test section, the position of the measuring instrument (LDV or Rayleigh scattering system) was fixed while the combustor was moved by the computer-controlled three-dimensional traversing mechanism. The Rayleigh scattering instrument noise was about 10%. The background radiation level ranged from 2 to 7% for case 2 and from 10 to 20% for case 3. The sampling rate was 2500 samples/sec and 8192 samples were taken at each location.

4.1 The Structure of the Turbulent Boundary Layer

Turbulent flows have long been regarded as chaotic and disorganized. Recent studies, however, have demonstrated the existence of large-scale, organized structures, superimposed on background turbulence, in turbulent shear flows. In free shear flow and the wake flow behind a cylinder, the large structures are essentially two-dimensional and relatively easy to identify (Roshko, 1976). In turbulent boundary layer flow, the large-scale structures are three-dimensional and more difficult to identify.

Flow-visualization experiments by Kline et al. (1967), Corino and Brodkey (1969), and Kim et al. (1971) have developed a rather complex description of an intermittent phenomenon in turbulent boundary layers. Termed "bursting", this phenomenon has been shown by Willmarth and Lu (1972) to be an important contributor to the production of turbulent kinetic energy and Reynolds stress. However, to develop a clear picture of three-dimensional structures from either direct measurements or flow-visualization techniques is very difficult, and understanding of the large-scale structure in a turbulent boundary layer is still limited.

In this study, Schlieren pictures were used only to reveal some of the overall features of the turbulent structure in the boundary layer. No attempt was made to extract quantitative data from these pictures.

4.1.1 The Heated-Wall Boundary Layer

Schlieren pictures of the heated-wall boundary layer are shown in Figs. 13a and 14a. Existence of identifiable large-scale structures, indicated by dark arrows on the picture, are not apparent until the thermal boundary layer attains sufficient thickness at about 25 mm downstream from the heating section leading edge. A sequence of events can be observed to take place: i) low speed, low density fluid moves upward from the surface; ii) high speed, high density fluid mixes with the upward-moving hot fluid, indicated by the slow disappearance of density gradients near the boundary of the structure; iii) the large-scale structure is carried downstream by the main flow. The overall shape of the turbulent structure is similar to that commonly observed in a turbulent boundary layer. Since the structure is three-dimensional, it is impossible to obtain information about its internal details from two-dimensional Schlieren pictures.

4.1.2 *The Reacting Boundary Layer*

Schlieren pictures of the reacting boundary layer are shown in Figs. 13b and 14b. Pictures of the leading edge in Fig. 13b indicate that considerable surface heating and surface reaction take place before any detached-flame structure starts to form. No well-defined continuous flame sheet is observed. Rather, individual flame structures are initiated at the heated surface and are swept downstream by the main flow. The flame structure, though larger in scale, has an overall structure quite similar to that of the turbulent structure in the heated boundary layer. Again no detail about the internal structure can be obtained.

4.2 Statistical Quantities

Although some understanding of turbulent structures in turbulent shear flows has been obtained in recent years due to advances in optical techniques and modern instrumentations, time-averaged properties of turbulence are still used in most theoretical and experimental turbulence studies. In utilizing the statistical approach through the basic conservation equations, a fundamental problem arises. In time-averaging, statistical correlations involving velocity, density, pressure, and temperature fluctuation appear in the governing equations. This results in more unknowns than equations; the problem of closure. One way to deal with this is by turbulent modelling, in which effects of the correlations are approximated in terms of other quantities in the governing equations. Proper ways of modelling these correlations are not obvious in most cases and better understanding of their basic properties and physical meanings is essential.

4.2.1 *Conservation Equations*

Governing equations for variable-density turbulent boundary layer flows are given in Nicholl (1970) and White (1974). The basic mean equations for conservation of mass, momentum, and enthalpy for a flat plate boundary layer are, respectively,

$$\frac{\partial}{\partial x} (\bar{\rho}\bar{u}) + \frac{\partial}{\partial y} (\bar{\rho}\bar{v} + \overline{\rho'v'}) = 0 \tag{4.1}$$

$$\bar{\rho}\bar{u} \frac{\partial \bar{u}}{\partial x} + (\bar{\rho}\bar{v} + \overline{\rho'v'}) \frac{\partial \bar{u}}{\partial y} = \frac{\partial}{\partial y} (\bar{\rho} \frac{\partial \bar{u}}{\partial y} - \overline{\rho u'v'}) \tag{4.2}$$

$$\bar{\rho}\bar{u} \frac{\partial \bar{h}}{\partial x} + (\bar{\rho}\bar{v}' + \overline{\rho'v'}) \frac{\partial \bar{h}}{\partial y} = \frac{\partial q}{\partial x} + \tau \frac{\partial \bar{u}}{\partial y} \tag{4.3}$$

where

$$\tau = \bar{\mu} \frac{\partial \bar{u}}{\partial y} - \overline{\rho u'v'}$$

$$q = k \frac{\partial \bar{T}}{\partial y} - \overline{\rho v'h'}$$

$$\bar{h} = \bar{h}_0 + \overline{C_p(T-T_0)}$$

and

μ = viscosity

k = thermal conductivity

h = enthalpy

h_0 = reference enthalpy of formation

T = temperature

T_0 = reference temperature

C_p = specific heat

Another important relation which governs the transportation of turbulent kinetic energy, k, is given by Nicholl (1970):

$$\frac{1}{2}\frac{\partial}{\partial x}(\overline{\rho u}k + \bar{\rho}\,\overline{u'k} + \bar{u}\,\overline{\rho'k}) + \frac{1}{2}\frac{\partial}{\partial y}(\overline{\rho v}k + \bar{\rho}\,\overline{v'k} + \bar{v}\,\overline{\rho'k})$$

$$+ (\bar{\rho}\,\overline{u'^2} + \bar{u}\,\overline{\rho'u'} + \overline{\rho'u'^2})\frac{\partial \bar{u}}{\partial x} + (\bar{\rho}\,\overline{u'v'} + \overline{\rho'v'}\,\bar{v} + \overline{\rho'u'v'})\frac{\partial \bar{u}}{\partial y}$$

$$+ (\bar{\rho}\,\overline{u'v'} + \bar{u}\,\overline{\rho'v'} + \overline{\rho'u'v'})\frac{\partial \bar{v}}{\partial x} + (\bar{\rho}\,\overline{v'^2} + \bar{v}\,\overline{\rho'v'} + \overline{\rho'v'^2})\frac{\partial \bar{v}}{\partial y}$$

$$+ \overline{\rho'v'}\,g + \overline{u_i\frac{\partial p'}{\partial x_i}} - \mu\,\overline{u_i\nabla^2 u_i} = 0 \tag{4.4}$$

where $k = u'^2 + v'^2 + w'^2$. This relation is simplified by Sommer (1979) for flat-plate boundary-layer flow to:

$$\underbrace{(\overline{\rho}\bar{u} + \overline{\rho'u'})\frac{\partial k}{\partial x} + (\bar{\rho}\bar{v} + \overline{\rho'v'})\frac{\partial \bar{k}}{\partial y}}_{(1)} = \underbrace{-\frac{\partial}{\partial y}(\overline{v'p'} + \bar{\rho}\,\overline{v'k})}_{(2)}$$

$$\underbrace{- \bar{\rho}\,\overline{u'v'}\frac{\partial \bar{u}}{\partial y}}_{(3)} \underbrace{- \bar{\mu}\,\Sigma\,\overline{(\frac{\partial u_i'}{\partial x_j})^2} - 2\mu\,\{\frac{\partial \bar{k}^{1/2}}{\partial y}\}^2}_{(4)}$$

Convection flux (1) = diffusion (2) + production (3)

$$\text{- dissipation (4)} \tag{4.5}$$

The validity of some of the simplifications in the above equation is questionable and one has to be careful in applying it to turbulent flow problems.

Inspection of the conservation equations reveals the existence of several unknown fluctuation correlations which have to be dealt with in

some way. It is theoretically possible to derive differential equations for all these correlations; however, each new equation would contain additional unknown correlations. Hence eventually some sort of approximation or modelling would have to be used to "close" the system of equations. Guides as to how to model these correlations can be provided by experimental measurements. Furthermore, physical interpretations of these measurements can give additional insights into the structure of a turbulent boundary layer.

4.2.2 Mean Velocity and Density

Two-dimensionality of the flow in the test section, indicated in Fig. 15 by the uniformity of the velocity profile in the z-direction, is reasonably good.

The development of the mean velocity profiles for the isothermal boundary layer are shown in Figs. 16a and 17a. The scattering in $\bar{v}$ is considerably larger than in $\bar{u}$. This is because $\bar{v}$ was determined from $\bar{u}_1$ and $\bar{u}_2$ (Eq. 3.30) whose values are an order of magnitude larger. Thus small errors in $\bar{u}_1$ and $\bar{u}_2$ will result in large errors in $\bar{v}$. The boundary layer thickness, δ, the displacement thickness, δ_1, and the momentum thickness, δ_2, are plotted in Figs. 18, 19 and 20 respectively, as functions of x. The boundary layer thickness is defined at 99.5% of the free-stream velocity, $\bar{u}_0$. δ_1 and δ_2 are defined by (White, 1974)

$$\delta_1 = \int_0^\infty (1 - \frac{\bar{\rho}\,\bar{u}}{\rho_0\bar{u}_0})\ dy \qquad\qquad (4.6)$$

$$\delta_2 = \int_0^\infty \frac{\bar{\rho}\,\bar{u}}{\rho_0\bar{u}_0}\ (1 - \frac{\bar{u}}{\bar{u}_0})\ dy \qquad\qquad (4.7)$$

where ρ_o is the free-stream fluid density. The displacement thickness ranges from 1.28 mm at x = 14 mm to 1.77 mm at x = 150 mm. The corresponding Reynolds number, Re_{δ_1}, ranges from 901 to 1247. The momentum thickness ranges from .653 to 1.023 mm, and Re_{δ_2} from 460 to 721. The friction coefficient, C_f, is determined by

$$C_f = 2 \frac{d \delta_2}{dx} = \frac{2\tau_w}{\rho_o \bar{u}_o^2} \qquad (4.8)$$

and is plotted in Fig. 21. When scaled by the local value of δ, the mean velocity profile is found to be self-similar (Fig. 22) and dependent on $y^{1/7}$, as it is for the typical flat plate boundary layer.

The mean velocity profiles, $\bar{u}$ and $\bar{v}$, for the heated-wall boundary layer are shown in Figs. 16b and 17b, and the mean density profile, $\bar{\rho}$, in Fig. 23a. The thermal boundary layer thickness (defined at 99.5% of $(\rho_o - \rho_w)$, difference between densities at the free stream and the surface), δ_T, is plotted in Fig. 24. δ_T is found to increase as $x^{.45}$. This growth rate of δ_T is smaller than that reported by Johnson and Whippany (1957) and Antonia et al. (1977) for the turbulent boundary layer with a small stepwise discontinuity in the wall temperature. This is probably a result of the significant density change near the wall. The enthalpy thickness, δ_{T_1}, defined by

$$\delta_{T_1} = \int^\infty \frac{\rho \bar{u}}{\rho_o \bar{u}_o} \frac{(T - T_o)}{(T_w - T_o)} \, dy \simeq \int^\infty \frac{\bar{\rho} \bar{u} (\rho_o/\bar{\rho} - 1)}{\rho_o \bar{u}_o (\rho_o/\rho_w - 1)} \qquad (4.9)$$

is plotted in Fig. 25. The Stanton number, St, is evaluated from

$$St = \frac{d \delta_{T_1}}{dx} = \frac{q_w}{\rho_o \bar{u}_o \bar{C}_p (T_o - T_w)} \qquad (4.10)$$

and is shown in Fig. 26. The Stanton number starts with a value of about 3.75×10^{-3} and decreases rapidly to an almost constant value of about 2.9×10^{-3}. The behavior and magnitude of St are quite similar to those reported by Antonia et al. (1977), although their experimental conditions were significantly different from the ones in this study. The velocity boundary layer thickness, plotted in Fig. 18, is increased by severe wall-heatings. The mean velocity and density profiles, as indicated in Figs. 27 and 28, show no overall similarity, although the velocity boundary layer looks approximately self-similar. However, they relax towards a self-similar stage about 100 mm downstream from the leading edge. There is no similarity between the velocity and the density profiles. The velocity profile of the cold- and heated-wall boundary layers are plotted in Fig. 29, with the origin of the latter being shifted in the y-direction by an amount equal to the difference in the corresponding boundary layer thicknesses. It can be seen that parts of the profiles so plotted are identical at a certain distance from the wall. This suggests that the effect of wall-heating is limited to the region near the wall. The heat-affected region expands and "pushes" the rest of the boundary layer upwards without alteration to its structure. The study by Nicholl (1970) indicates the existence of a local wall-jet when a turbulent boundary layer is subjected to a severe stepwise temperature rise. This is probably because Nicholl's experiment was carried out in a developing channel flow. The additional upper-wall restriction and the local fluid expansion cause the fluid to accelerate in the streamwise direction rather than expand in the y-direction. The displacement and momentum thicknesses are plotted in Figs. 19 and 20. Severe wall-heating has increased δ_1 significantly and increased δ_2 to a small degree. The value of the friction coefficient,

indicated in Fig. 22, is also increased by wall-heating, contrary to the results of Rotta (1974). This contradiction can be explained by considering the effect of severe heating on the viscosity, μ, and the velocity gradient, $\frac{d\bar{u}}{dy}\Big|_w$, near the wall. The viscosity of the fluid near the wall increased with temperature. The velocity gradient, on the other hand, is decreased by the expansion of the heat-affected region. In the case of moderate temperature rise, as in Rotta (1974) where maximum $T_w/T_o = 1.78$, the latter effect dominates and the value of C_f decreases. In the case of large temperature rise, as in the present study where $T_w/T_o = 4.2$, the increase in μ dominates and results in a higher value of C_f.

The development of the mean velocity and density profiles in the reacting boundary layer is shown in Figs. 16c, 17c and 23b. The mean density profile indicates the existence of a local minimum fluid density away from the wall. The density gradient, or temperature gradient, near the wall is small, thus heat transfer from the wall can be neglected in comparison with the heat generation from chemical reaction. The value of $\bar{v}$ in the free-stream increases significantly, indicating a large streamline deflection away from the surface. The thermal boundary layer thickness (defined at .955 $(\rho_o - \bar{\rho}_b)$, where $\bar{\rho}_b$ is the minimum density), δ_T, is plotted in Fig. 24 and is found to be approximately proportional to $x^{.6}$. The velocity boundary layer thickness, the displacement thickness, and the momentum thickness all increase due to fluid expansion. The friction coefficient, shown in Fig. 21, also increases. No overall similarity is observed for either the density or the velocity profiles (Figs. 30 and 31). However, the stage of self-similarity seems to be reached about 100 mm downstream from the leading edge, much as in the stepwise heating boundary layer. The velocity profiles of the isothermal

and the reacting boundary layer are plotted together in Fig. 32 in the same way as in Fig. 29. Sections of the profiles away from the surface are observed to be similar to the heated-wall case.

4.2.3 Density and Velocity Fluctuations

Turbulent flows are characterized by rapid fluctuations in their velocity components and passive scalar quantities. The root-mean-square (rms), $\hat{u}$ and $\hat{v}$, of the velocity fluctuations for the three different experimental cases are plotted in Figs. 33 and 34, and the rms density fluctuations are shown in Fig. 36. The free-stream turbulence is about 1%. The magnitudes of the free stream $\hat{u}$ and $\hat{v}$ are about the same, an indication that the turbulence is isotropic.

Rms velocity fluctuations of the isothermal boundary layer show slightly higher values in the wall region near the heating-section leading edge. This indicates that the flow may be tripped as it crosses from the smooth aluminum surface to the heating-section. A similar trend is observed for other fluctuation correlations measured. The rms profiles are compared with those of Corrsin and Kistler (from Hinze, 1975) for a rough surface in Fig. 35. It can be seen that the agreement between the profiles is fairly good; the deviation is due mainly to the difference in the free-stream turbulence.

Severe wall-heating does not seem to have a significant effect on the velocity fluctuation. The value of $\hat{u}$ near the surface is raised by about 2%, while $\hat{v}$ remains essentially unchanged. The density fluctuation reaches a peak of about 19% at $y/\delta \simeq .2$ and then drops off near the surface. This is quite different from the results of Johnson (1959) and Sreenivasan and Antonia (1977) for a small stepwise temperature rise.

In Johnson's result, the temperature fluctuation reaches a peak value at $y/\delta \simeq .05$. Sreenivasan and Antonia's result does not show any drop-off in rms temperature down to $y/\delta \simeq .1$. The density and velocity fluctuation profiles are plotted against y/δ_T and y/δ in Figs. 37 and 38. As is expected, no overall similarity is observed for either profile. However, both do seem to relax towards a self-similar stage starting at $x \simeq 100$ mm.

The presence of combustion in the boundary layer induces local peaks in both the $\hat{u}$ and $\hat{v}$ profiles. Near the leading edge, the peaks are more distinct and less "spread-out" than farther downstream. As can be seen in the Schlieren pictures in Section 4.1.2, combustion near the leading edge is confined to a smaller region than farther downstream, hence the combustion-induced peaks in $\hat{u}$ and $\hat{v}$ are also narrower and more distinct. Near the wall, the value of $\hat{v}$ decreases while $\hat{u}$ remains almost unchanged from the isothermal case. The density fluctuation also shows a distinct peak at a location approximately corresponding to the rms velocity peaks. The peak value of $\hat{\rho}$ reaches 46% near the leading edge and about 37% further downstream. The difference in peak values of $\hat{\rho}$ can also be explained the same way as the difference in combustion-induced peak rms velocity. Since no distinct continuous flame sheet exists in the flow (Section 4.1.2), the location of the rms peaks should be interpreted as the locations where reaction is most probable to occur rather than as the mean flame positions. As indicated in Figs. 39 and 40, approximate self-similarity for $\hat{\rho}$ and $\hat{u}$ is reached at about 100 mm downstream.

4.2.4 *Reynolds Stress*

In the process of averaging the momentum equation, a triple corre-
lation, $\overline{\rho\, u'v'}$, arises. This quantity is interpreted physically as the

contribution to the stress by the turbulent fluid motion and is termed the Reynolds stress. Considerable effort has been directed towards understanding of the behavior of the Reynolds stress under different flow situations. Recent studies have indicated that large-scale turbulent structure is one of the main contributors to the Reynolds stress near the wall region of a turbulent boundary layer.

The Reynolds stress can be decomposed into two parts:

$$\overline{\rho\, u'v'} = \bar{\rho}\,\overline{u'v'} + \overline{\rho'u'v'} \tag{4.11}$$

The second term on the right-hand side is small in low Mach-number compressible flow and is usually neglected. A number of investigators have extended this result to general variable-density flows. However, the validity of this extension is not clear for cases like combustion where the density variation arises from local heat release. Measurement of the triple correlation is difficult and no conclusions has yet been reached about its relative importance.

The non-dimensionalized Reynolds stress, τ_t $(= -\,2\,\bar{\rho}\,\overline{u'v'}/\bar{u}_0^{\,2})$, is plotted in Fig. 41a. The value of τ_t increases from zero at the free-stream to about .004 near the wall. The maximum value of τ_t is larger than the typical value of about .003 reported in most studies over smooth surfaces. This is probably because the test section in this study is actually a surface with uniform roughness elements.

In the case of severe wall-heating, the value of τ_t near the wall is reduced. This is due to the reduction in fluid density without the proportional increase in the value of $\overline{u'v'}$. The correlation coefficient between u' and v', defined by

$$R_{uv} = \overline{u'v'}/\hat{u}\ \hat{v} \ , \qquad\qquad (4.12)$$

is plotted in Figs. 42 and 43. The value of R_{uv} is essentially unaffected by the severe wall-heating, although the scatter may be too large to allow a definite conclusion to be drawn. This suggests that the turbulent structures responsible for the correlation between u' and v' are not altered significantly by the relatively regular fluid expansion resulting from wall-heating.

The value of τ_t is greatly reduced by the presence of combustion in the boundary layer. This reduction is due both to the decrease in density and $\overline{u'v'}$. The value of R_{uv} is also reduced by combustion (Figs. 42 and 43). This indicates that the turbulent structure responsible for the correlation between u' and v' is altered by the vigorous and relatively random fluid expansion resulting from combustion.

A length scale for the flows can be obtained by Prandtl's mixing length theory. The theory states that

$$- \bar{\rho}\ \overline{u'v'} = \bar{\rho}\ \ell_m^2 \left|\frac{\partial u}{\partial y}\right| \frac{\partial u}{\partial y}$$

or

$$\ell_m = \left[\frac{-\ \overline{u'v'}}{|\partial u/\partial y|\frac{\partial u}{\partial y}}\right]^{1/2} \qquad\qquad (4.13)$$

where ℓ_m is the mixing length. Some typical results of ℓ_m are shown in Fig. 44. The results for the isothermal and the heated-wall boundary layers compare reasonably well with the Escudier formula (Launder and Spalding, 1972). The agreement is not as good in the case of the reacting boundary layer, although the Escudier formula is claimed to be valid for

uniform-density flow as well as variable-density ones. It may be because the presence of combustion has altered the basic turbulent structure responsible for the Reynolds stress in a boundary layer.

4.2.5 Turbulent Kinetic Energy Transportation

Many studies of turbulent flows have been concerned with the transportation of the turbulent kinetic energy, k. Although averaging tends to conceal the physics of the transport process, physical interpretation of various averaged kinetic energy transport correlations do provide some valuable insights into the behavior of turbulent flows.

The average turbulent kinetic energy transport equation (Eq 4.4) is rather complex. Basically, it can be divided into four parts: (1) convection, (2) diffusion, (3) production, and (4) dissipation, as in the simplified form (Eq. 4.5).

The velocity component, w, in the z-direction was not measured in this study due to experimental difficulties. The quantity k_1 (Eq. 3.32) was used in place of k. Most previous studies have indicated that contributions of w' to k and its transport quantities are similar to and of the same order of magnitude as those of u' and v'. Hence it is reasonable to assume turbulent transportation of k_1 will be similar to that of k.

4.2.5.1 Turbulent Kinetic Energy Distribution

The non-dimensionalized turbulent kinetic energy distribution are plotted in Fig. 45. The profile of the isothermal flow is typical of a flat-plate boundary layer.

Wall-heating does not seem to have significant effect on the kinetic energy distribution. The value of $\bar{k}_1$ increases slightly near the wall due to the increase in u'.

The kinetic energy profiles for the reacting boundary layer indicate the existence of a local peak value away from the surface. The presence of combustion thus would seem to produce additional turbulence in part of the boundary layer.

4.2.5.2 Streamwise Turbulent Kinetic Energy Diffusion

The developments of $\overline{u'k_1}$ profiles are shown in Fig. 46. $\overline{u'k_1}$ is interpreted as the transport, or diffusion, in the streamwise different of k_1 by turbulent actions. This term is usually neglected in studying boundary layer flows. However, the situation is less clear when a stepwise discontinuity, like the stepwise temperature rise or combustion in this study, is present in the flow. It is quite conceivable that, at least near the leading edge of the discontinuity, the boundary layer assumption may no longer be valid if the discontinuity has any significant effect on the turbulent structure of the flow.

The value of $\overline{u'k_1}$ in the isothermal boundary layer is negative, indicating that the fluid associated with negative u' is more energetic. The slow change in the $\overline{u'k_1}$ profile supports the boundary layer assumptions that streamwise diffusion of k_1 is not important.

Severe wall-heating reduces the value of $\overline{u'k_1}$ near the wall significantly. The change in the $\overline{u'k_1}$ profile is rather rapid near the leading edge and is a lot more gradual further downstream. This indicates that the stepwise temperature rise induces significant net streamwise turbulent

kinetic energy diffusion near the leading edge of the heating section. In other words, the sudden fluid expansion causes the failure of the boundary layer assumption in the wall region near the temperature discontinuity.

In the reacting boundary layer, the value of $\overline{u'k_1}$ is positive near the surface. A second negative peak is induced in the reaction zone near the wall. Expansion of the reaction zone eventually "swallows" the original negative peak, causing the profile to look more like that of a turbulent boundary layer. The locations of the negative peaks are shifted upwards in accordance with the divergency of the steamlines. The magnitude of the combustion-induced negative peak increases as the flow progresses, indicating positive turbulent energy transport along the streamlines by streamwise turbulence.

4.2.5.3 Cross-stream Turbulent Kinetic Energy Diffusion

The results of $\overline{v'k_1}$ are shown in Fig. 47. $\overline{v'k_1}$ can be interpreted physically as the diffusion of k_1 by the fluctuation in the v-component. The slope, $\partial\overline{v'k_1}/\partial y$, indicates the loss (positive slope) or gain (negative slope) of kinetic energy at a given location due to cross-stream diffusion.

The result of the isothermal flow is typical of a turbulent boundary layer. The values of $\overline{v'k_1}$ are all positive, meaning that the fluid associated with positive v' is more energetic. The profile has a peak near the middle of the boundary layer. The location of the peak, where the slope is zero, is the switch-over point from the kinetic energy loss to the kinetic energy gain region.

In the case of severe wall-heating, a second $\overline{v'k_1}$ peak appears near

the wall region. The slope of $\overline{v'k_1}$ now changes sign over three locations instead of one; and an additional kinetic energy gain and kinetic energy loss region are induced in the boundary layer.

In the reacting boundary layer, $\overline{v'k_1}$ is reduced to below zero with a negative peak near the wall by combustion. The negative value of $\overline{v'k_1}$ implies the fluid associated with negative v' is more energetic. A kinetic energy gain, or negative $\partial\overline{v'k_1}/\partial y$, region now exists near the surface.

4.2.5.4 Production of Turbulent Kinetic Energy

The production of turbulent kinetic energy by turbulent stress, $-\bar{\rho}\,\overline{u'v'}\,\partial\bar{u}/\partial y$, is plotted in non-dimensional form in Fig. 48. The profile for the isothermal flow is typical of a turbulent boundary layer. Severe wall-heating only causes a modest reduction in the production rate near the surface. This indicates that the production mechanism is not significantly affected. The situation, however, is quite different for the reacting boundary layer. The kinetic energy production rate is greatly reduced by the presence of combustion. This suggests that the turbulent structure or mechanism responsible for the turbulent stress and its subsequent kinetic energy production is altered by the vigorous fluid expansion resulting from chemical reaction. The fact that the kinetic energy per unit mass does not decrease, but actually increases in some regions either means that contributions from other production terms in the kinetic energy equation are significant, or the dissipation has to decrease, or both. Hence it may be hypothesized that combustion can disrupt the turbulent kinetic energy production mechanism in a turbulent

flow and cause the reduction of kinetic energy; it also can produce turbulence by mechanisms like density fluctuation-velocity fluctuation interactions. Depending on which is dominant, the result can either be a decrease or an increase in turbulent kinetic energy. The disruption of large-scale turbulent structures by combustion was also observed by Pitz (1981) in a reacting shear layer where the eddy coalescence process is reduced.

4.2.6 Distribution of $\overline{u'v'k_1}$

The distribution of $\overline{u'v'k_1}$ (Fig. 49) indicates a correlation between velocity fluctuations and kinetic energy. The physical meaning of this correlation is not clear. It increases from zero outside the boundary layer to a maximum value near the wall. Its distribution is not affected by severe wall-heating. The presence of combustion, on the other hand, significantly reduces the value of the correlation. This suggests that the turbulent structure is less organized in the reacting boundary layer than in the isothermal and heated layers.

4.3 Probability Density Functions (PDF's)

Some results of the density and velocity probability density functions are presented in this section, along with the skewness and flatness factor. The skewness factor, S_c, for quantity c is defined by

$$S_c = \overline{c'^3}/(\overline{c'^2})^{3/2} \tag{4.14}$$

and the flatness factor, F_c, by

$$F_c = \overline{c'^4}/(\overline{c'^2})^2 \qquad (4.15)$$

where c is either the density or the velocity. The skewness factor indicates distributions in the wings. A Gaussian distribution has a skewness factor of zero and a flatness factor of 3. The probability, P, of the observed value of a quantity c lies in between c_1 and c_2 is given by integrating the PDF over the range (c_1, c_2):

$$P(c_1 < c < c_2) = \int_{c_1}^{c_2} PDF(c) dc \qquad (4.16)$$

From a given set of experimental data, the number (N_i) of samples falling within discrete (c_1, c_2) ranges were counted. The PDF's were then obtained by

$$PDF(c_1 < c < c_2) = \frac{N_i}{(c_2 - c_1) \cdot \Sigma N_i} \qquad (4.17)$$

4.3.1 PDF of Density

The skewness factor and flatness factor of the density measurements are given in Figs. 50 and 51 respectively; and some typical pdf's are shown in Figs. 52, 53 and 54. The free-stream fluctuations, which are due to the presence of noise in the signal, are almost Gaussian as indicated by S_ρ and F_ρ .

In the stepwise wall-heating boundary layer, the distribution of S_ρ and F_ρ at large distance downstream are similar to those measured by Subramanian and Antonia (1978) for the temperature in a slightly heated boundary layer. Near the heating section leading edge, the situation is somewhat different. S_ρ decreases to a negative peak before it reaches a positive maximum near the wall while F_ρ shows two peak values. This is probably because the velocity and the thermal boundary layer are not developed simultaneously, resulting in only part of the boundary layer being affected by the wall-heating. Hence, near the leading edge, the thermal boundary layer is governed primarily by fluid mechanical structures near the surface rather than the over all structures in the boundary layer. Both S_ρ and F_ρ relax towards distributions more typical of a turbulent boundary layer as the flow progresses and the thermal and velocity boundary layers begin to merge.

S_ρ for the reacting boundary layer shows a positive peak near the wall and a negative one further away, while F_ρ shows two distinct positive peaks. The profiles do not change significantly as the flow progresses, indicating that the temperature field is governed by similar fluid structures quite early. The distribution is almost Gaussian near the wall. Since the fluctation near the surface is small, the PDF represents primarily the distribution of the noise. The PDF's in figs. 53 and 54 show that the distribution is bimodal near the center of the reaction zone. This bimodal distribution is considerably less distinct than that observed by Bill et al. (1981) in a V-shaped flame. Bill attribute the distribution to the movement of the flame sheet about the

probe volume, with the two peaks representing the burnt and unburnt
fluid. As indicated in Section 4.1, combustion in the boundary layer
occurs as a collection of flame structures rather than as a continuous
flame sheet; thus there is more mixing action between the burnt and the
unburnt fluid, resulting in a significant amount of fluid being in the
intermediate states. The point at which the bimodal distribution is
symmetrical ($S_\rho = 0$) represents the location where the presence of burnt
and unburnt fluid is equally probable. Above this point, the peak of the
PDF centers about the unburnt fluid density. The occasional passage
of flame structures contributes to the distribution in the low density
wing, resulting in a negative S_ρ. Below the bimodal point, the PDF peak
centers about the burnt fluid density, indicating that the majority of
the fluid in this region is burnt. The "tail" in the high density wing
shows the existence of unburnt reactant which causes the skewness factor
to become positive.

4.3.2 PDF of Velocity

Skewness and flatness factors of the streamwise velocity fluctuation,
u', are plotted in Figs. 55 and 56 respectively. Typical PDF's are
given in Figs. 57 to 61. The skewness factor, S_u, of the isothermal
flow is negative with a minimum near the middle of the boundary layer.
The negative value of S_u indicates the turbulence associated with negative
u' is more intense. The value of the flatness factor, F_u, is larger
than 3 and has a positive peak at the location coinciding with the negative
peak in S_u. The distribution of S_u and F_u are in close agreement with
those of Retchert and Azad (1979). The free-stream turbulence and the

turbulence near the surface are almost Gaussian as indicated by their respective S_u and F_u.

Severe wall-heating induces a small local negative peak in S_u and a small positive peak in F_u near the surface. The distribution is therefore deviated further from Gaussian by wall-heating. The deviation, however, is small and does not represent a significant change in the basic flow structure.

In the reacting boundary layer, S_u and F_u deviate from the isothermal flow in ways similar to the heated-wall case, except that the changes are more profound. The negative peak in S_u and the positive peak in F_u near the surface are much more distinct, suggesting a significant change in the basic flow structures. The value of S_u very close to the surface is positive, indicating the velocity fluctuation associated with positive u' is now more intense. The PDF's do not show any distinct bimodal distribution as in the V-shaped flame studied by Bill (1981). This again is due to the occurrence of combustion as discrete flame structures extended over the entire boundary layer instead of as a continuous flame sheet confined to a small region, thus resulting in more gradual changes in the velocity.

4.4 Spectral Analysis

A detailed description of the physical interpretation of spectra is given in Tennekes and Lumley (1972). Spectra are decompositions of the measured function into waves of different frequencies or wavelengths. The spectrum enables one to get a picture of how the fluctuation "energy"

is transferred between eddies of different sizes.

4.4.1 *Streamwise Velocity Spectrum*

Velocity spectra represent the distribution of mean turbulent kinetic energy in frequency space. The large-scale (low frequency) or "energy-containing" eddies are the ones primarily responsible for obtaining kinetic energy from the mean flow. The energy is then cascaded from large to small eddies through the process of vortex stretching, and is eventually dissipated near the Kolmagorov microscale through viscous effects. The range of frequencies at which no energy is added by the mean flow and no energy is dissipated by viscous action is termed the inertial subrange. The energy flux across each frequency in this range is constant. Dimensional analysis reveals that the spectral energy, E( ), in the inertial subrange is proportional to $^{-5/3}$.

Typical one-dimensional spectra of the streamwise velocity are shown in Figs. 62, 63 and 74. The inertia subrange is indicated on the graph by the - 5/3 slope. Values of the spectrum at all frequencies increase as the turbulent level increases with decreasing y. It is evident that the sampling rate is too slow for obtaining dissipation spectra at high frequencies.

Severe wall-heating seems to expand the energy-containing frequency range and cause the inertia subrange to start at a higher frequency. Combustion, on the other hands, causes the energy-containing frequency range to contract and the inertia subrange to start at a lower frequency. These changes are less evident near the leading edge where the reaction is confined mainly to regions very close to the wall. Spectral energy

levels at low frequencies are now higher, thus the value of $\hat{u}$ near the wall remains almost unchanged.

4.4.2 *Density Spectrum*

Typical spectra of the density measurement are given in Figs. 65 and 66. It is a common belief and observation (Hinze, 1975, and Tennekes and Lumley, 1972) that the cascade in the spectrum of a passive scalar quantity is similar to that in the velocity spectrum. However, no - 5/3 slope is observed in any range of the density spectrum. A range with slope of -1 is found to exist instead. The spectrum of the free-stream signal, which is dominated by the instrument noise, is uniform over the entire frequency range. In the reacting boundary layer, the spectrum near the surface is also fairly uniform due to the dominance of the noise. Both the density and the velocity spectra indicate that the fluctuation energy is concentrated at frequencies less than 1000 Hz.

5. SUMMARY AND CONCLUSIONS

The laser-Doppler-velocimetry and the Rayleigh-scattering systems have been proven to be effective in studying high temperature and combusting flows. The feasibility of using the single-component LDV to measure second and higher order velocity correlations has also been demonstrated. Some conclusions and a summary of the results of this investigation are presented in this section.

Isothermal Boundary Layer

Results of the isothermal boundary layer compare well with those typical of a turbulent boundary layer. The boundary layer is found to be slightly tripped as the flow enters the heating section.

Effects of Stepwise Heating

Effects of the severe stepwise temperature rise on the boundary layer are summarized below:

1) As revealed by the Schlieren pictures, the overall turbulent structure in the heated boundary layer is similar to that in an isothermal boundary layer.

2) Wall-heating causes the expansion of the heat-affected region near the surface and pushes the rest of boundary layer upwards. Significant structural changes of the boundary layer are found to occur only in the heat-affected region.

3) The boundary layer thickness, the displacement thickness, and the momentum thickness are increased by the wall-heating. The thermal

boundary layer thickness increases as $x^{.45}$ rather than the often reported value of $x^{.8}$.

4) The friction coefficient increases because of the increase in viscosity near the surface.

5) The level of $\hat{u}$ near the wall increases slightly by the fluid expansion while $\hat{v}$ remains essentially unchanged. The maximum fluctuation in the density occurs at $y/\delta \simeq .2$. This is much further from the surface than the location of maximum temperature fluctuation observed in most slightly heated boundary layers.

6) The Reynolds stress near the wall is reduced due to the density drop while the correlation coefficient between u'v' remains essentially unchanged.

7) The value of $\overline{u'k_1}$ near the surface is reduced quite rapidly near the leading edge. This means that the streamwise turbulent diffusion of kinetic energy is significant, thus the boundary layer assumption is no longer valid. A local peak is induced in the $\overline{v'k_1}$ profile near the wall region, indicating a change in the cross-stream diffusion pattern.

8) The production rate of turbulent kinetic energy by Reynolds stress remains almost unchanged. This suggests that the turbulent structure responsible for the kinetic energy production is not altered by severe heating.

9) Density PDF's near the leading edge behave differently from those further downstream. This is because the temperature field near the leading edge is controlled mainly by fluid structures near the surface instead of the overall structures in the entire boundary layer. The effect of density change on the velocity PDF is relatively small.

10) Both the density and velocity spectra indicate that the turbulent energy is concentrated at frequencies less than 1000 Hz.

Effects of Combustion

Effects of combustion on the boundary layer are summarized here:

1) The Schlieren pictures indicate that there is significant fluid heating and surface reaction near the leading edge. At locations further downstream, discrete flame structures are initiated at the hot surface and are swept downstream by the main flow.

2) The boundary layer thickness, the displacement thickness, and the momentum thickness are increased by combustion. The value of C_f is increased due to increase in the viscosity of the fluid.

3) Local peaks in the $\hat{u}$ and $\hat{v}$ profiles are induced by combustion. The value of maximum $\hat{\rho}$ is higher near the leading edge than further downstream because the reaction zone is narrower and more confined near the leading edge.

4) The Reynolds stress and the correlation coefficient between u' and v' are reduced. This suggests that the turbulent structure responsible for the correlation between the velocity fluctuations is affected by the vigorous fluid expansion.

5) Significant changes in both the $\overline{u'k_1}$ and the $\overline{v'k_1}$ profiles are observed. This indicates that the kinetic energy diffusion pattern is altered by the presence of combustion. The large streamwise gradient of $\overline{u'k_1}$ near the leading edge also implies the failure of the boundary layer assumption.

6) The kinetic energy production by Reynolds stress is greatly reduced,

indicating that the production mechanism is disrupted by the vigorous fluid expansion. The fact that there is no reduction in the kinetic energy suggests that contributions from other production mechanisms must be important.

7) The value of $\overline{u'v'k_1}$ is greatly reduced, implying that the turbulent structure is less organized.

8) Bimodal density PDF's are observed in the middle of the reaction zone. The passage of flame structures causes non-Gaussian behavior in the density PDF's.

9) Significant changes in velocity PDF's are observed. Unlike the case of a sheet flame, no bimodal velocity PDF is found. This is because the combustion zone is spread over the entire boundary layer, resulting in more gradual and continuous velocity changes.

10) The density and velocity spectra indicate that fluctuation energy is concentrated in eddies with frequencies less than 1000 Hz.

REFERENCES

Antonia, R. A., Danh, H. Q. and Prabhu, A. (1977), "Response of a Turbulent Boundary Layer to a Step Change in Surface Heat Flux," J. Fluid Mech., Vol. 80, part 1, pp. 153-177.

Bill, R. G., Jr., Namer, I., Talbot, L., Cheng, R. K. and Robben, F. (1981), "Flame Propagation in Grid-Induced Turbulences," to be published in Combustion and Flame.

Buchhave, P. and George, W. K., Jr. (1978), "Bias Corrections in Turbulence Measurements by the Laser Doppler Anemometer," Laser Velocimetry and Particle Sizing, Edited by Thompson, H. D. and Stevenson, W. H., Hemisphere Publishing Corp., Washington.

Cairnie, L. R., Harrison, A. J. and Summers, R. (1981), "Acetaldehyde Autoignition and Cool Flames in a Free Convection Boundary Layer," First Specialists Meeting (Int'l) of the Combustion Institute, The French Section of the Combustion Institute, Vol. 2, p. 366.

Chen, L. D. and Faeth, G. M. (1981), "Ignition of Gases During Flow Near a Heated Surface," First Specialists Meeting (Int'l) of The Combustion Institute, The French Section of the Combustion Institute, Vol. 2, p. 395.

Cheng, R. K., Bill, R. G., Jr. and Robben, F. (1980), "Experimental Study of Combustion in a Turbulent Boundary Layer," Eighteenth Symposium (Int'l) on Combustion, The Combustion Institute, p. 1021.

Cheng, R. K. and Ng, T. T. (1981), "Experimental Study of the Flowfield of a V-shaped Premixed Turbulent Flame," Specialists Meeting (Int'l) of the Combustion Institute, The French Section of the Combustion Institute, Vol. I, p. 13.

Corino, E. R. and Brodkey, R. S. (1969), "A Visual Investigation of the Wall Region in Turbulent Flow," J. Fluid Mech., Vol. 37, part 1, pp. 1-30.

Dimotakis, P. E. (1976), "Single Scattering Particle Laser Doppler Measurements of Turbulence," AGARD No. 193.

Doebelin, E. O. (1975), Measurement Systems, McGraw-Hill Book Company, New York.

Drain, L. E. (1972), "Coherent and Noncoherent Methods in Doppler Optical Beat Velocity Measurement," J. Phys. D: Appl. Phys., 5, 481.

Drain, L. E. (1980), The Laser Doppler Technique, John Wiley & Sons, Ltd. New York.

Durrani, T. S. and Greated, C. A. (1977), Laser System in Flow Measurement, Plenum Press, New York.

Durst, F., Melling A. and Whitelaw, J. H. (1976), Principles and Practice of Laser-Doppler Anemometry, Academic Press, London.

Durst, F., Popp, M. and Tropea, C. D. (1980), "Turbulence Measurements over a Backward-Facing Step," SFB Report.

Glass, M. and Kennedy, I. M. (1977), "An Improved Seeding Method for High Temperature Laser Doppler Velocimetry," Combustion and Flame, 29 p. 333.

Gouesbet, G., Valentine, P. and Grehan, G. (1979), "Laser Velocimetry in RF Plasmas," Laser Velocimetry and Particle Sizing, Edited by H.D. Thomson and W.H. Stevenson, Hemisphere Publishing Corp., Washington, p. 335.

Hinze, J. O. (1975), Turbulence, McGraw Hill, New York.

Johnson, D. S. and Whippany, N. J. (1957), "Velocity, Temperature, and Heat-Transfer Measurements in a Turbulent Boundary Layer Downstream of a Stepwise Discontinuity in Wall Temperature," J. Applied Mechanics, March, pp. 2-8.

Johnson, D. S. (1959), "Velocity and Temperature Fluctuation Measurements in a Turbulent Boundary Layer Downstream of a Stepwise Discontinuity in Wall Temperature," J. Appl. Mech., September, p. 325.

Kim, H. T., Kline, S. J. and Reynolds, W. C. (1971), "The Production of Turbulence Near a Smooth Wall in a Turbulent Boundary Layer," J. Fluid Mech., Vol. 50, part 1, pp. 133-160.

Kline, S. J., Reynolds, W. C., Schraub, F. A. and Runstadler, P. W. (1967), "The Structure of Turbulent Boundary Layer," J. Fluid Mech., Vol. 30, part 4, pp. 741-773.

Launder, B. E. and Spalding, D. B. (1972), Mathematical Models of Turbulence, Academic Press, London.

Mayo, W. T. (1969), "Laser Doppler Flowmeters - a Spectral Analysis," Ph.D. Thesis, Georgia Institute of Technology.

Moreau, P. and Boutier, A. (1976), "Laser Velocimeter Measurements in a Turbulent Flame," Sixteenth Symposium (Int'l) on Combustion, The Combustion Institute, p. 1747.

Namer, I., Schefer, R. W. and Chan, M. (1980), "Interpretation of Rayleigh Scattering in a Flame," Lawrence Berkeley Laboratory Report, LBL-10655.

Nicholl, C.I.H. (1970), "Some Dynamical Effects of Heat on a Turbulent Boundary Layer," J. Fluid Mech., Vol. 40, part 2, pp. 361-384.

Pitz, R. W., Cattolica, R., Robben, F. and Talbot, L. (1976), "Temperature and Density in a Hydrogen-Air Flame From Rayleigh Scattering," Combustion and Flame, Vol. 27, pp. 313-320.

Pitz, R. W. (1981), "An Experimental Study of Combustion: The Turbulent Structure of a Reacting Shear Layer Formed at a Rearward-Facing Step," Ph.D. Dissertation, U. of California, Berkeley, California.

Rambach, G. D., Dibble, R. W. and Hollenbach, R. E. (1979), "Velocity and Temperature Measurements in Turbulent Diffusion Flames," presented at the Western States Combustion Meeting at Lawrence Berkeley Laboratory, Berkeley, California, October 15-16.

Rask, R. B. (1979), "Velocity Measurements Inside the Cylinder of a Motored Internal Combustion Engine," Laser Velocimetry and Particle Sizing, Edited by H. D. Thompson and W. H. Stevenson, Hemisphere Publishing Corp., Washington, p. 251.

Retchert, J. K. and Azad, R. S. (1979), "Features of a Developing Turbulent Boundary Layer Measured in a Bounded Flow," Can. J. Phys., Vol. 57, p. 477.

Reynolds, W. C. (1976), "Computation of Turbulent Flows, Ann. Review of Fluid Mech., Vol. 8, p. 183.

Robben, F. (1975), "Comparison of Density and Temperature Measurement Using Raman Scattering and Rayleigh Scattering," Lawrence Berkeley Laboratory Report, LBL-3294.

Roshko, A. (1976), "Structures of Turbulent Shear Flows: A New Look," presented at AIAA 14th Aerospace Science Meeting, Washington, D.C., January 26-28.

Rotta, J. C. (1974), "The Turbulent Boundary Layer on a Flat Plate with Severe Surface Heating at Subsonic Flow," Wärme- und Stoffübertragung, Vol. 7, 133-144.

Rudd, M. J. (1969), "A New Theoretical Model for the Laser Dopplermeter," J. Phys. E.: Sci. Instrum., Vol. 2, 55.

Schefer, R. W., Robben, F. and Cheng, R. K. (1980), "Catalyzed Combustion of H_2/Air Mixtures in a Flat-Plate Boundary Layer: I. Experimental Results," Combustion and Flame, Vol. 38, pp. 51-63.

Shapiro, A. H. (1953), The Dynamics and Thermodynamics of Compressible Fluid Flow, Art. 3.7, The Ronald Press Company, New York.

Parameter	Magnitude
λ	514.5 nm
D	1.2 mm
θ	4.84°
d_f	6.1 μm
d	327 μm
d_x	232 μm
d_y	231 μm
d_z	5.47 mm

Table 1   Important Parameters of the
LDV Setup
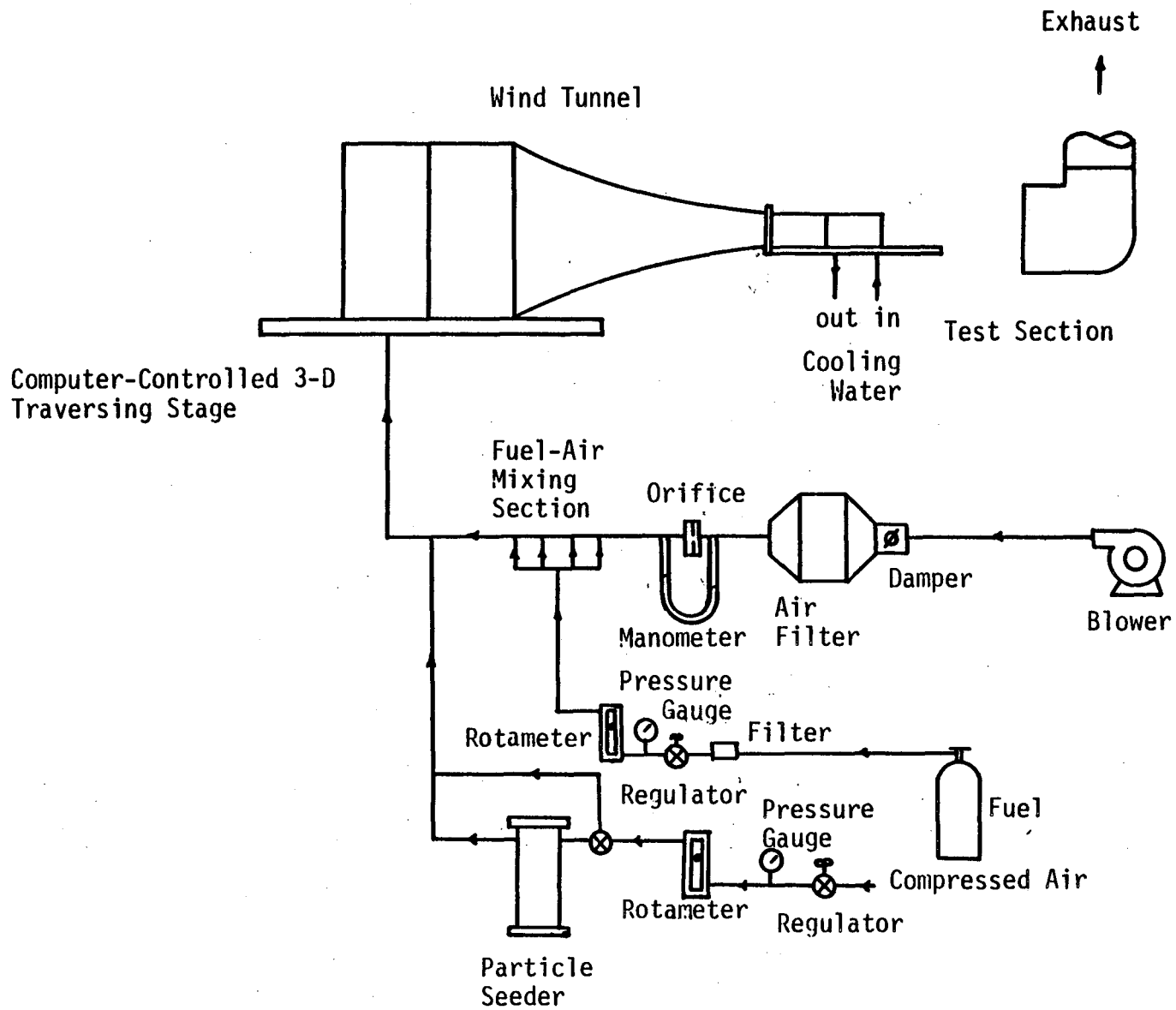
Fig. 1   Schematic Diagram of the Flow System
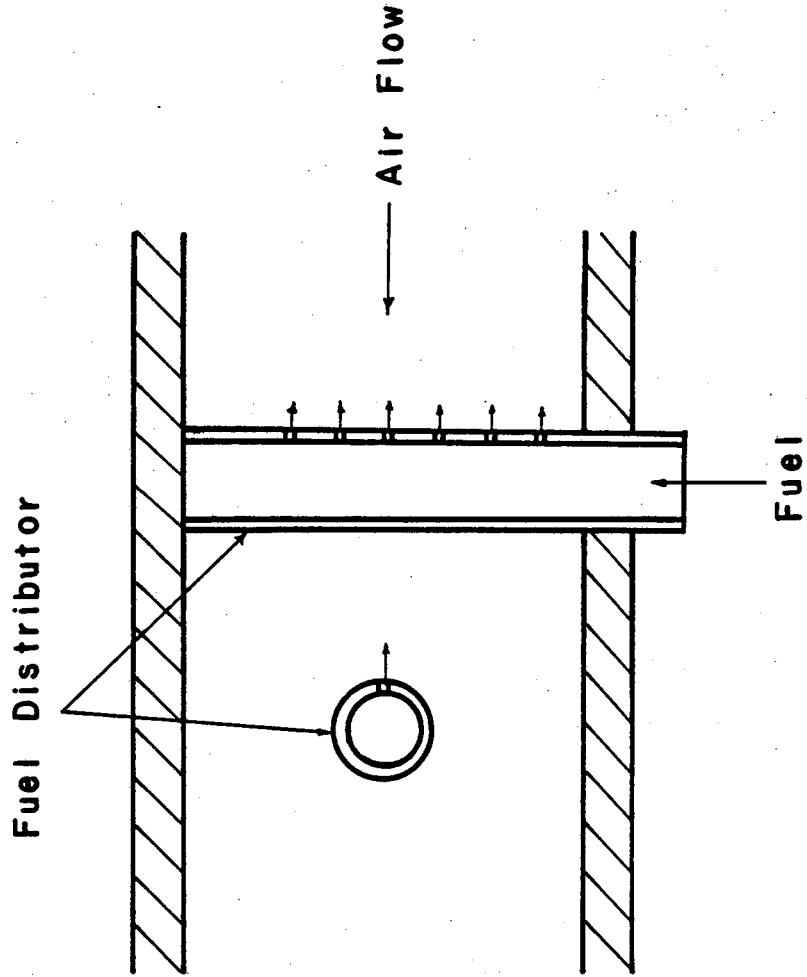
Fig. 2   Fuel Distributor
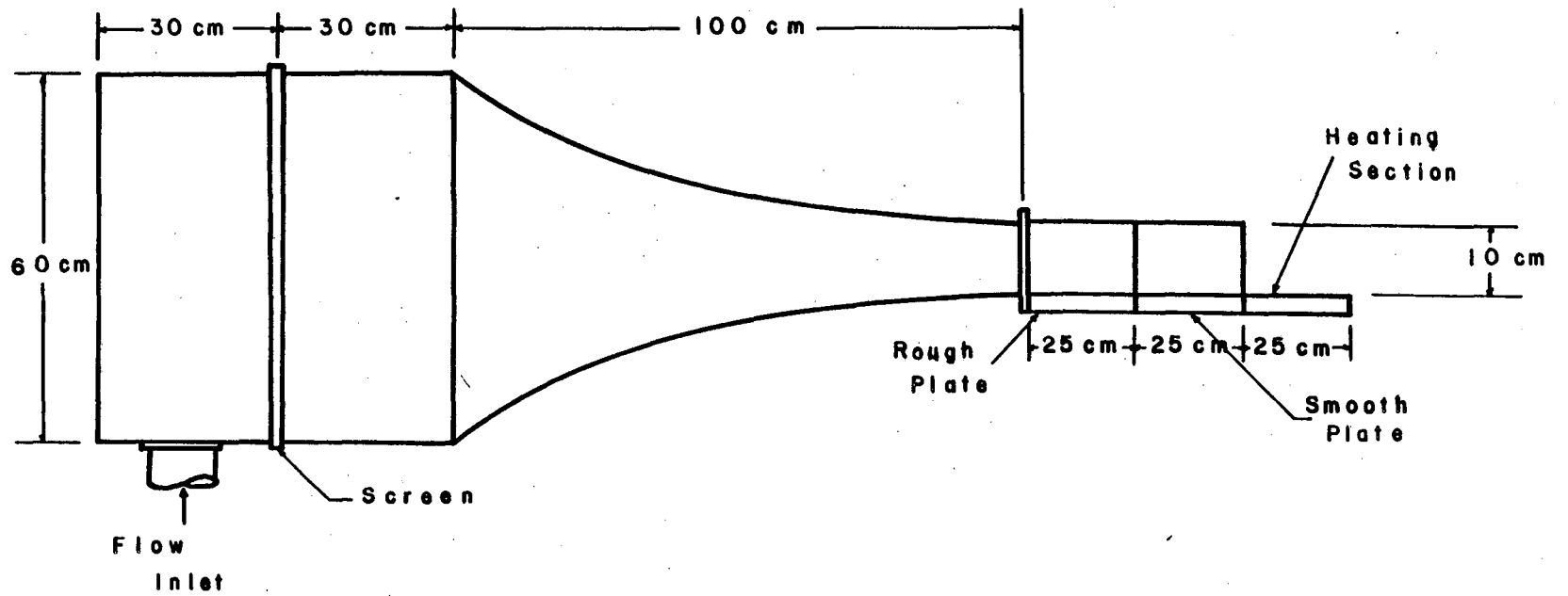
Fig. 3   The Wind Tunnel

Fig. 4   The Ceramic Block

to Transformer

Insulating Ceramic Ring

Heating Strip

Ceramic Block

Electric Contact Block

to Transformer

Tension Spring
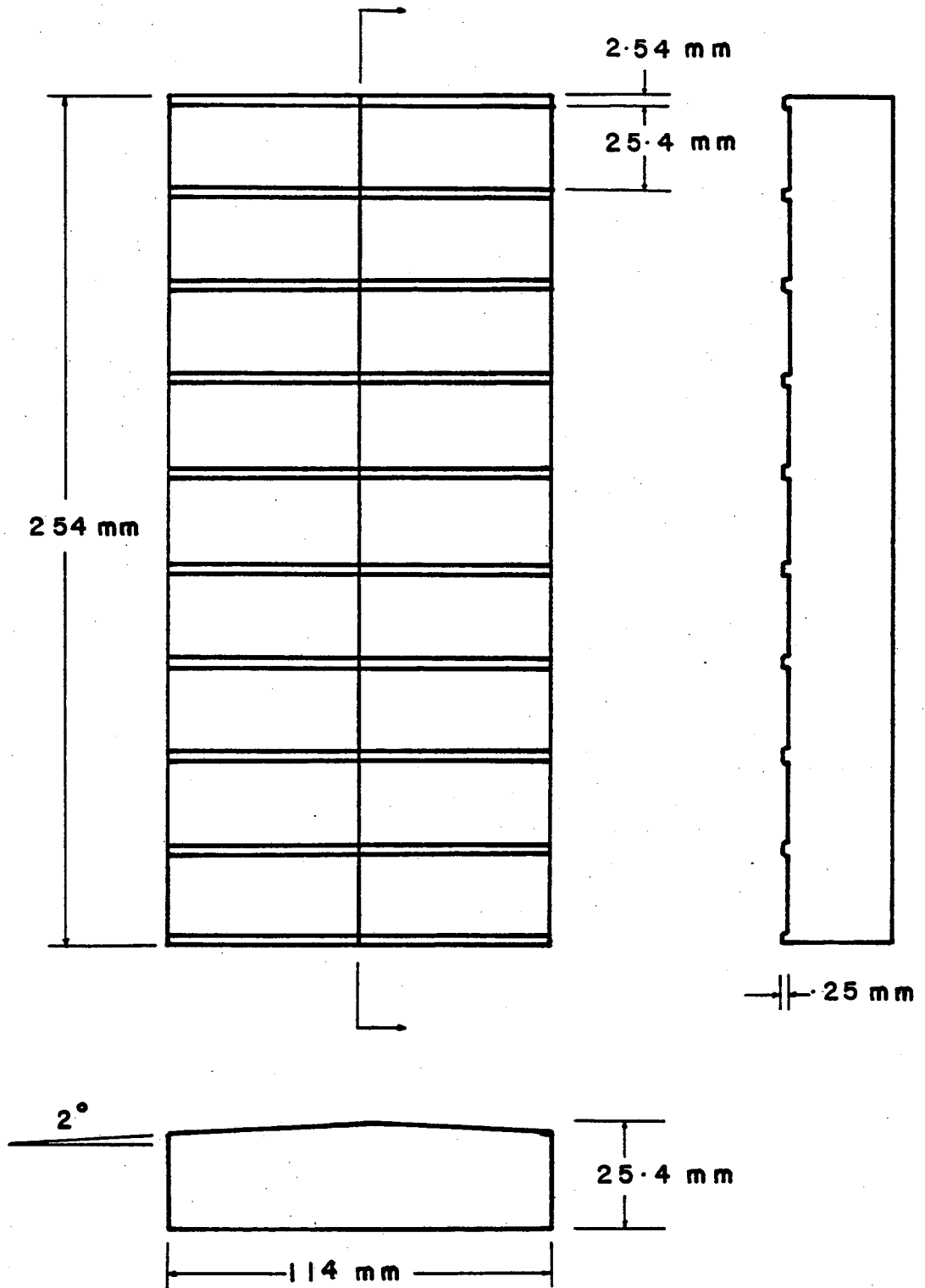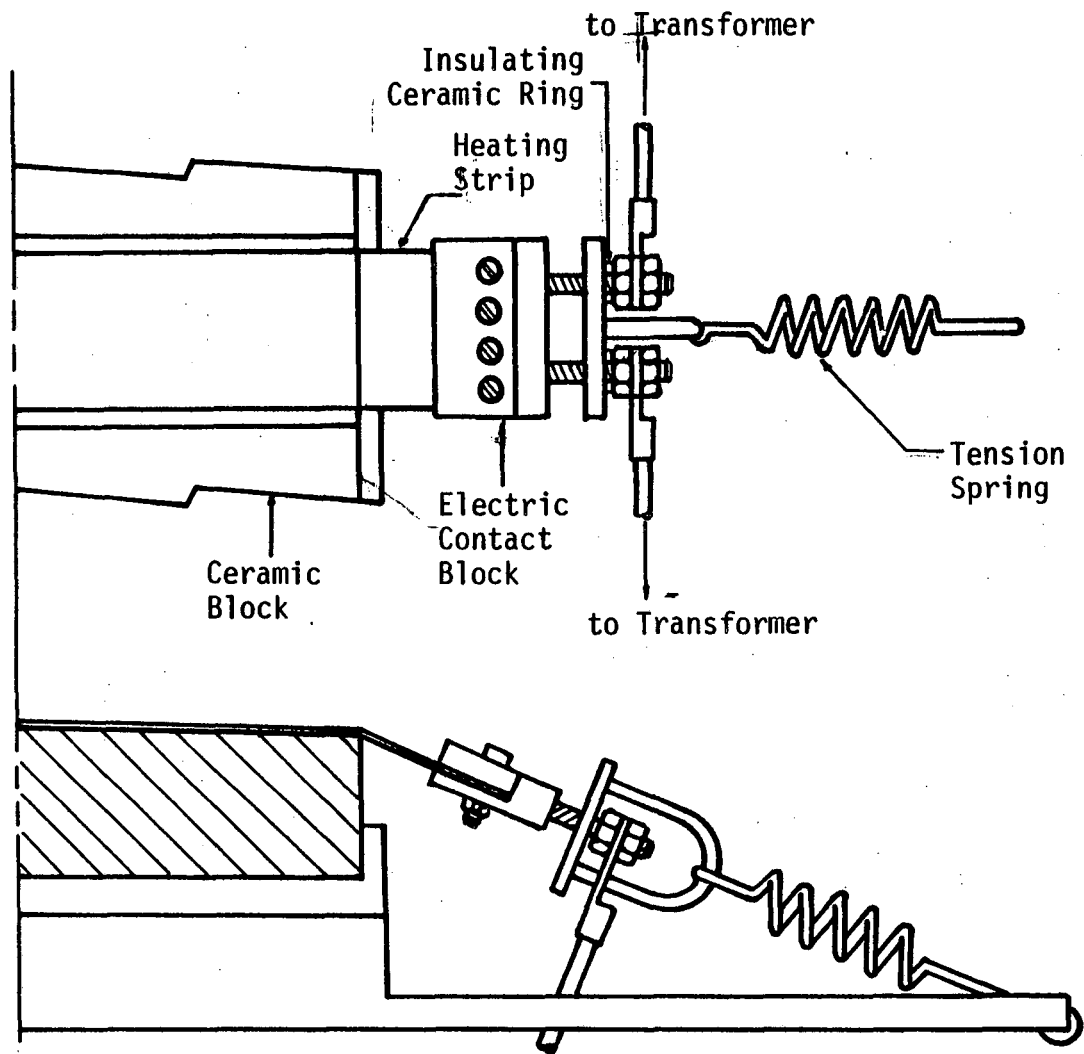
Fig. 5   The Heating Strip
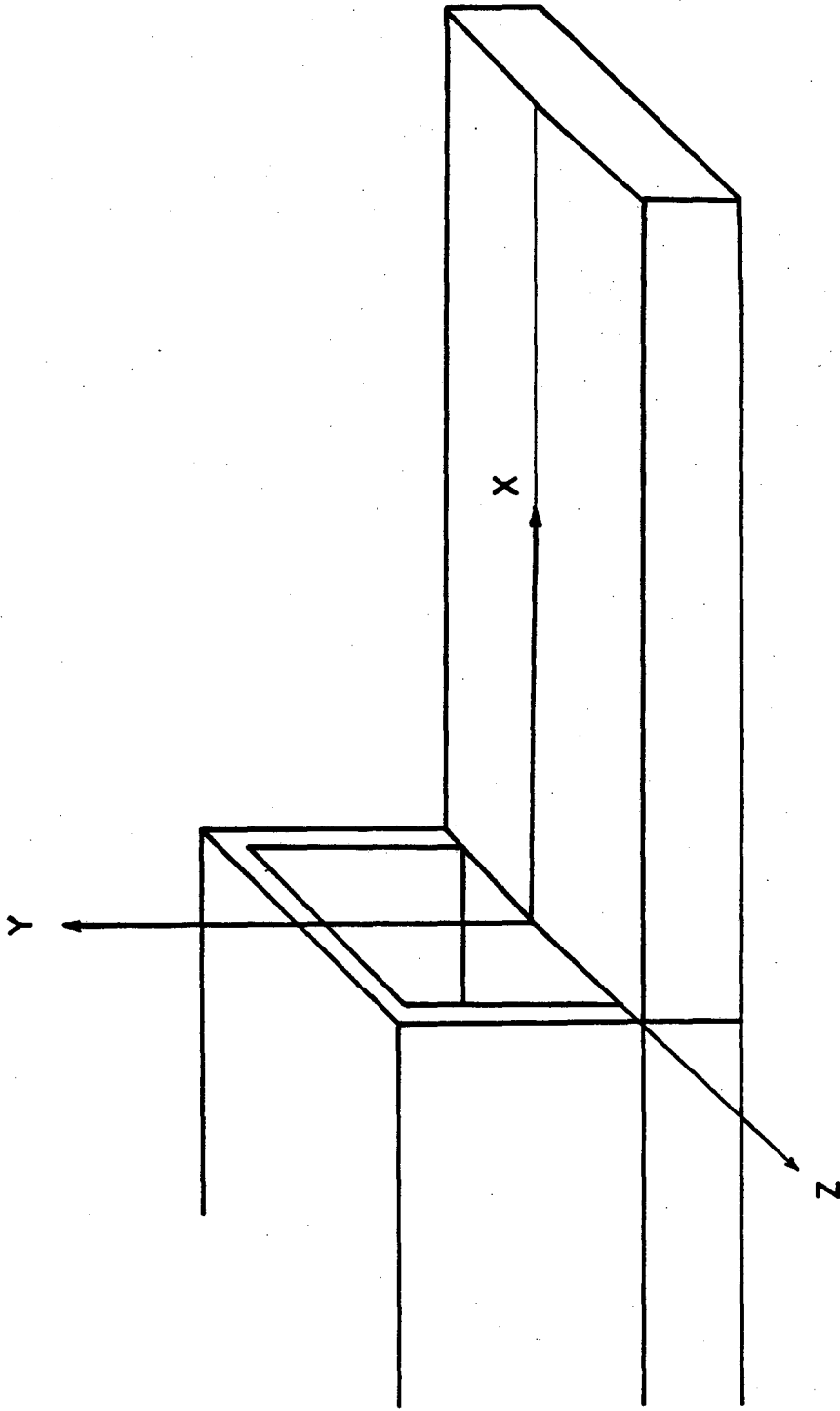
Fig. 6   The Coordinate System
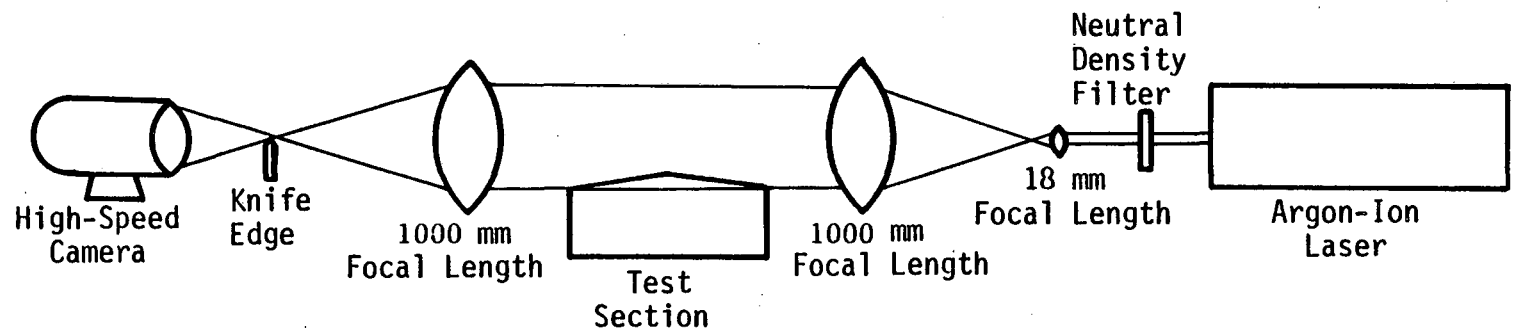
Fig. 7   The Schlieren System

Movement to Either Side of the Beam
for Background Radiation Measurement

Collecting lens

PMT

Filter

Slits

55 mm Focal Length
f 1.2

0.5
mm

0.5
mm

Laser
Beam Waist

Light
Trap

113 mm

120 mm
Focal Length

18 mm
Focal Length

Iris

4 Watt Argon-Ion
Laser

Test Section

576 mm

170 mm
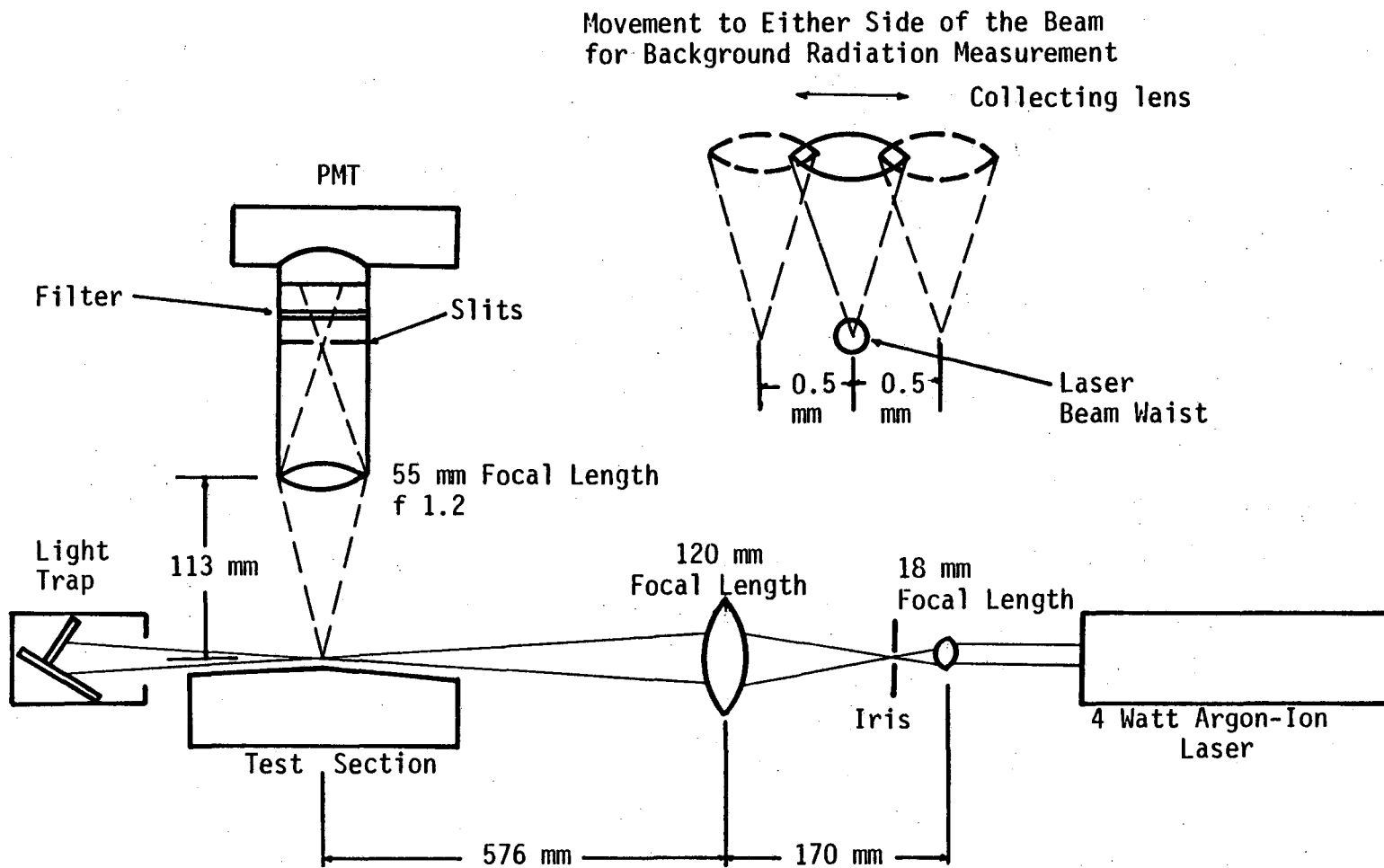
Fig. 8   The Rayleigh Scattering System
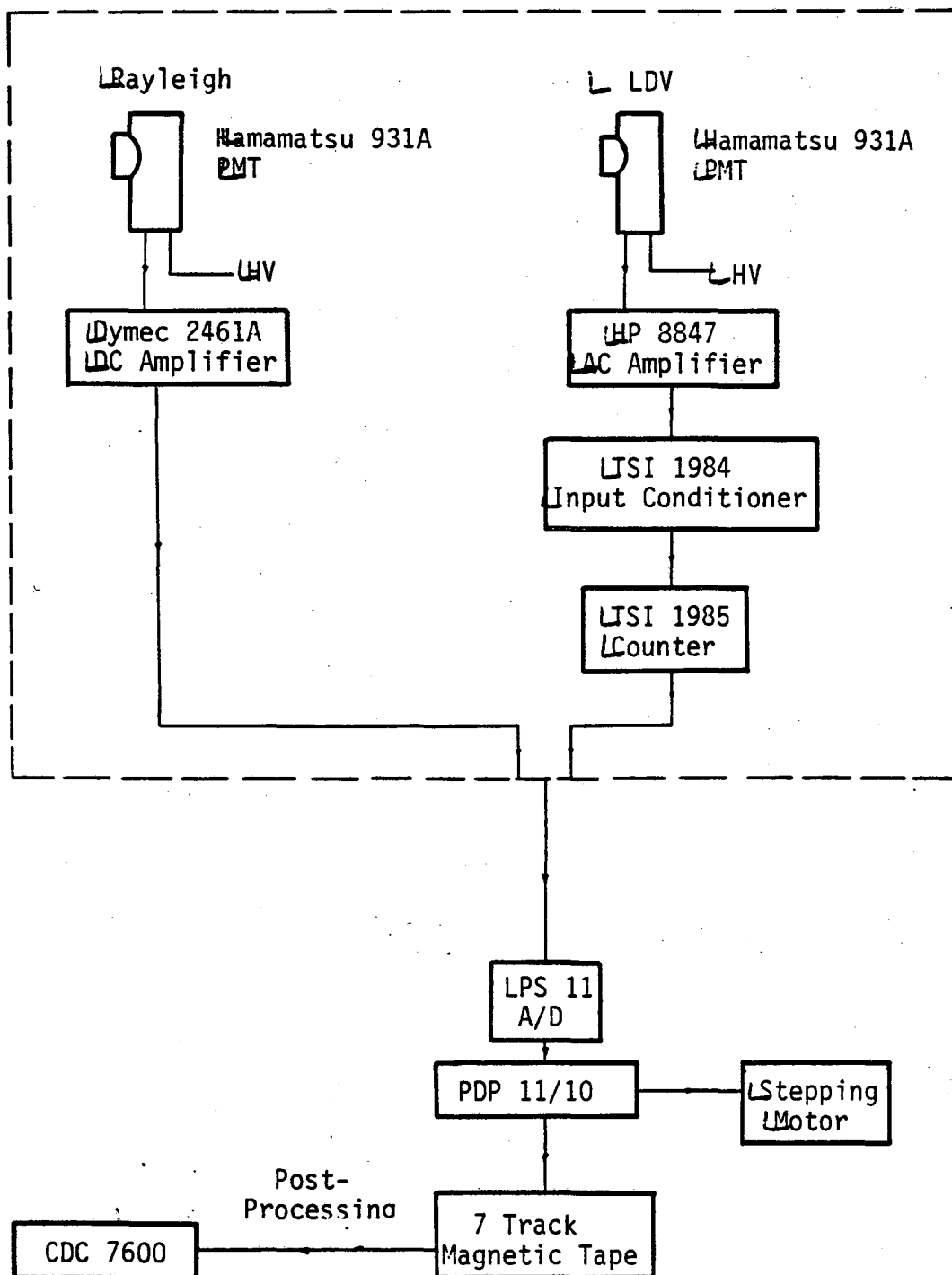
Fig. 9   The Data Aquisition System
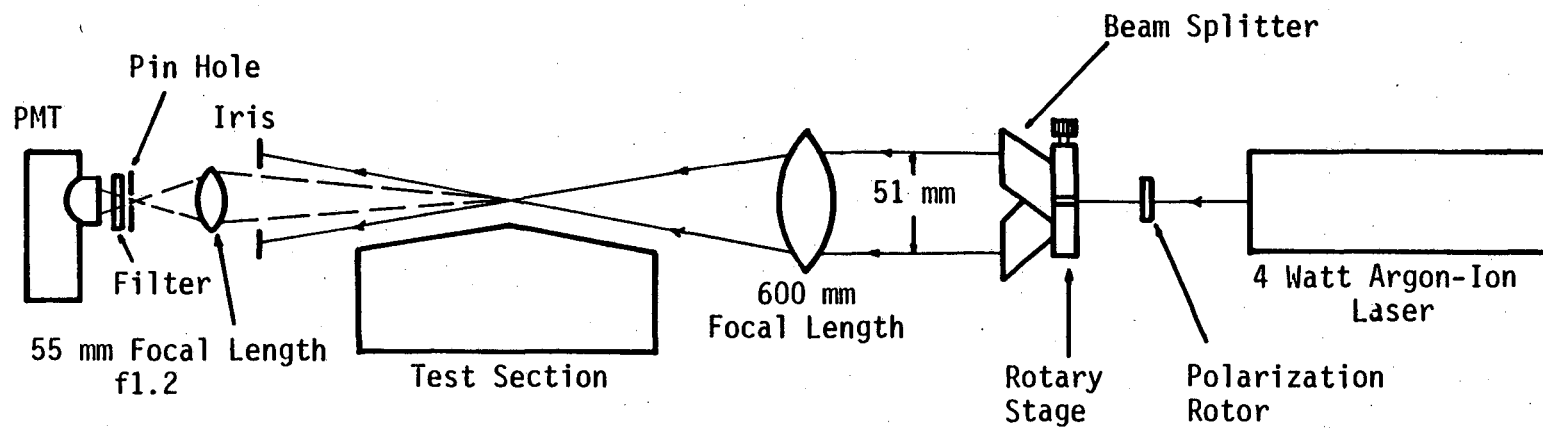
Fig. 10   The LDV System
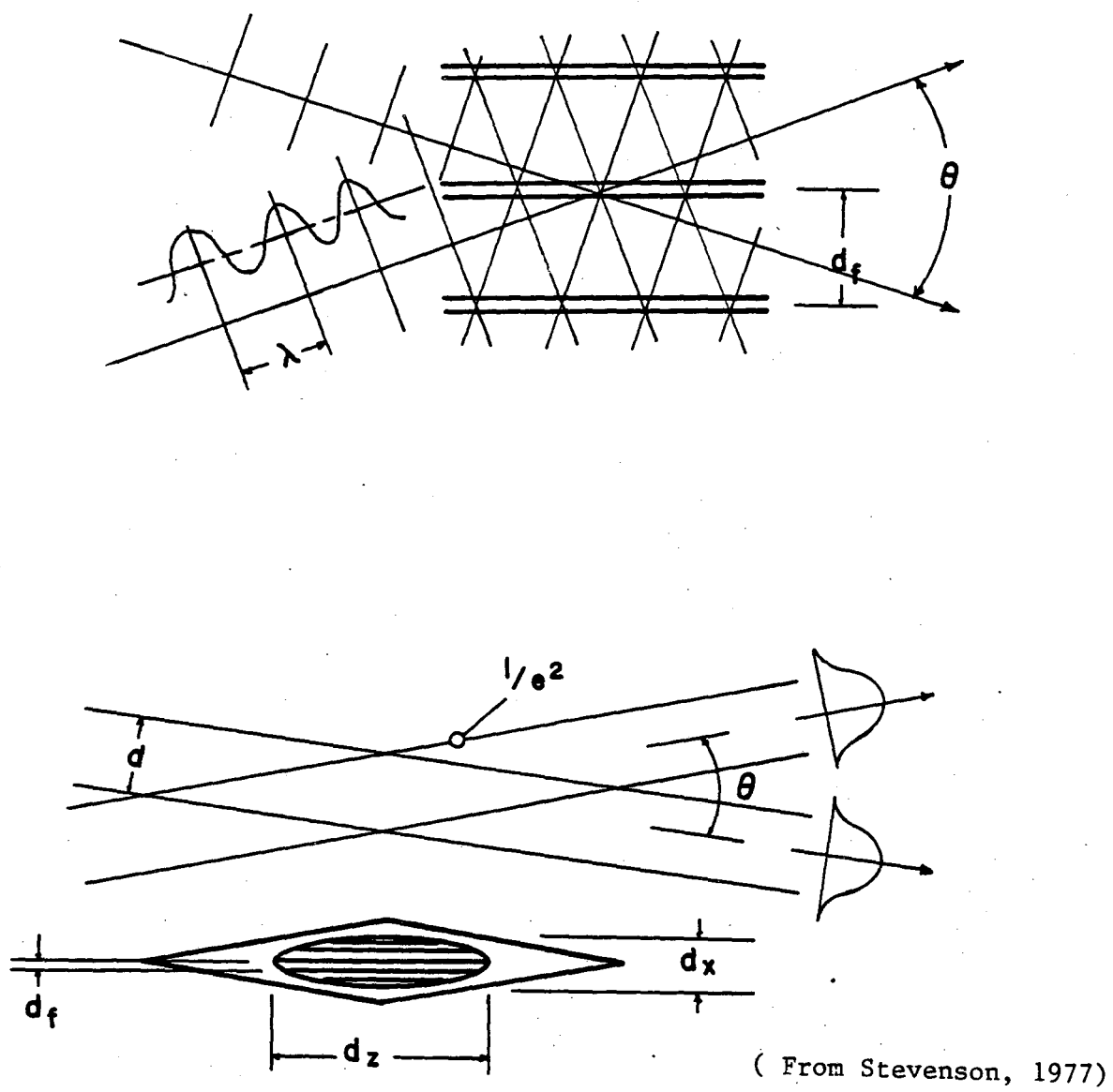
Fig. 11   The Interference Fringe Model

(From Stevenson, 1977)
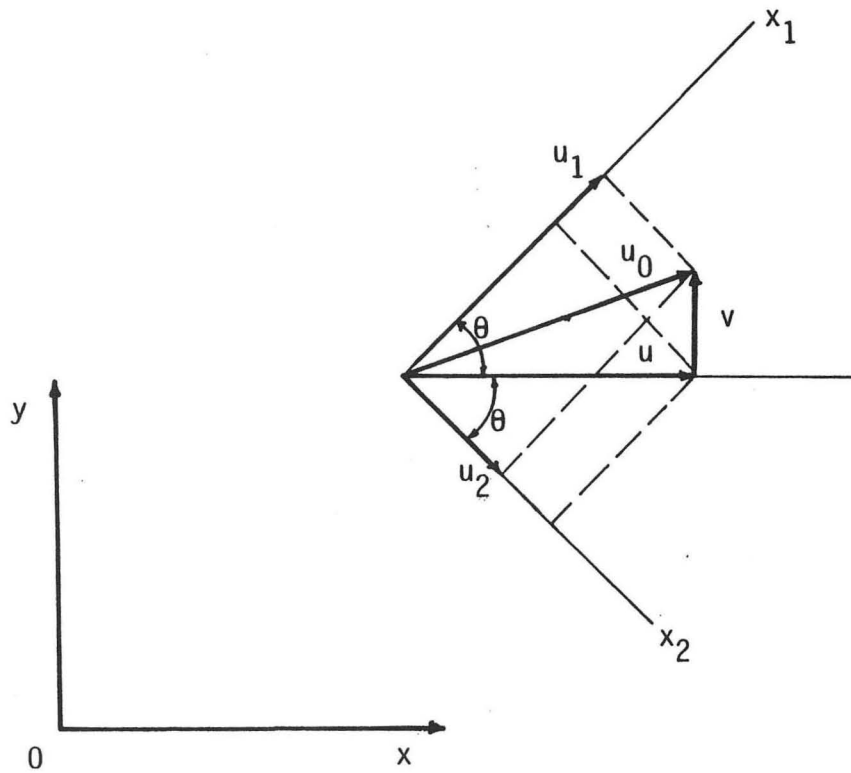
u_0 = Instantaneous velocity

u_1 = Velocity component in x_1 direction

u_2 = Velocity component in x_2 direction

Fig. 12   The Velocity Components
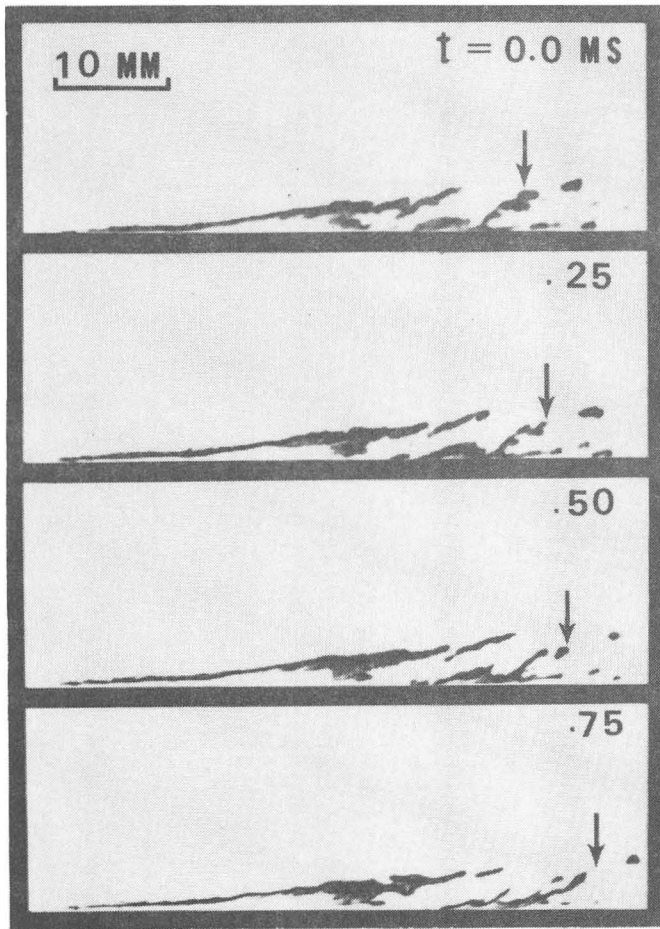
Fig. 13a Schlieren Pictures of the
          Heated Boundary Near the
          Leading Edge
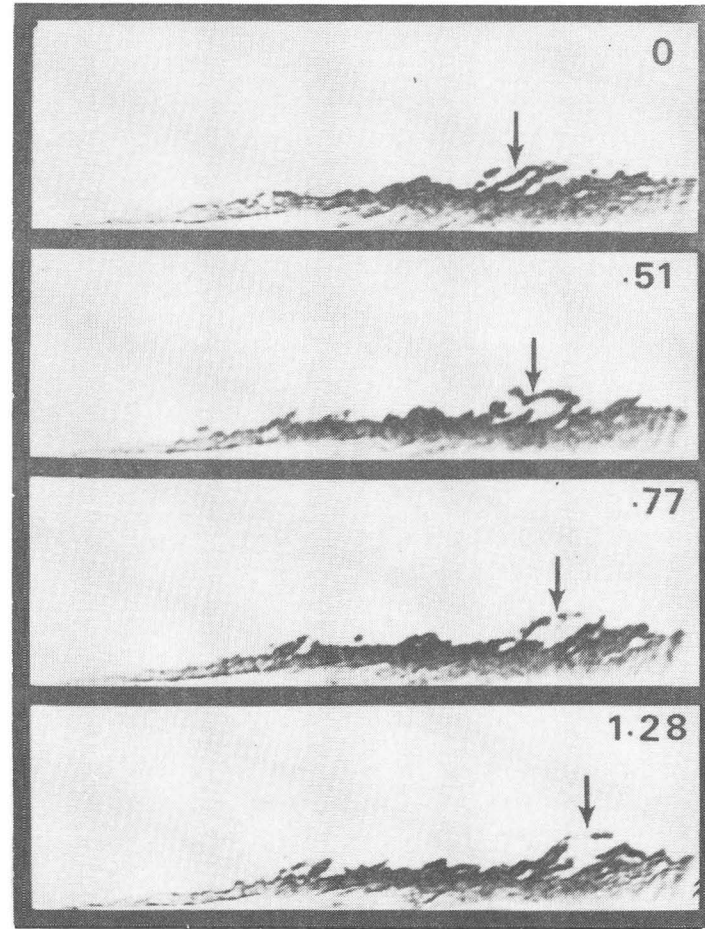
Fig. 13b Schlieren Pictures of the
          Reacting Boundary Layer
          Near the Leading Edge

XBB 817-6448

70
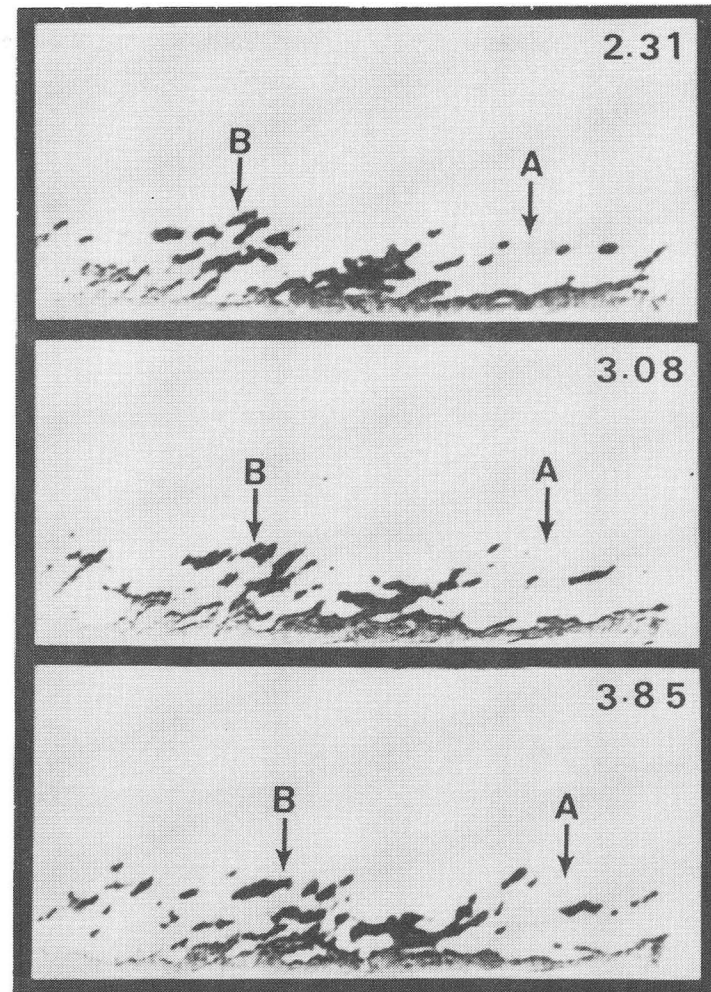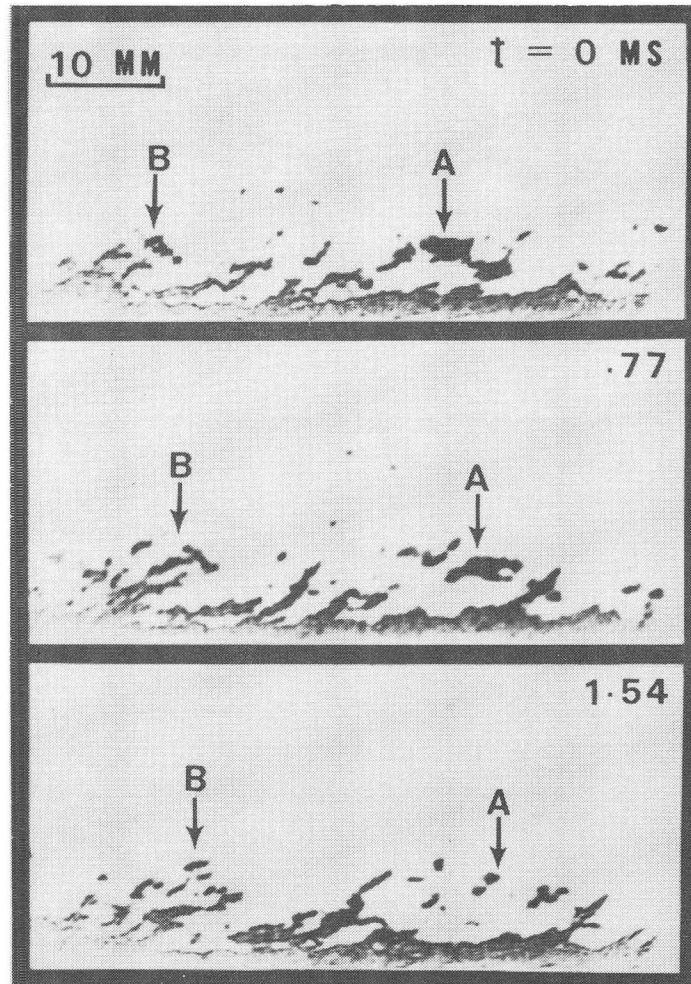
Fig. 14a Schlieren Pictures of the Heated Boundary
Layer Farther Downstream

XBB 817-6449
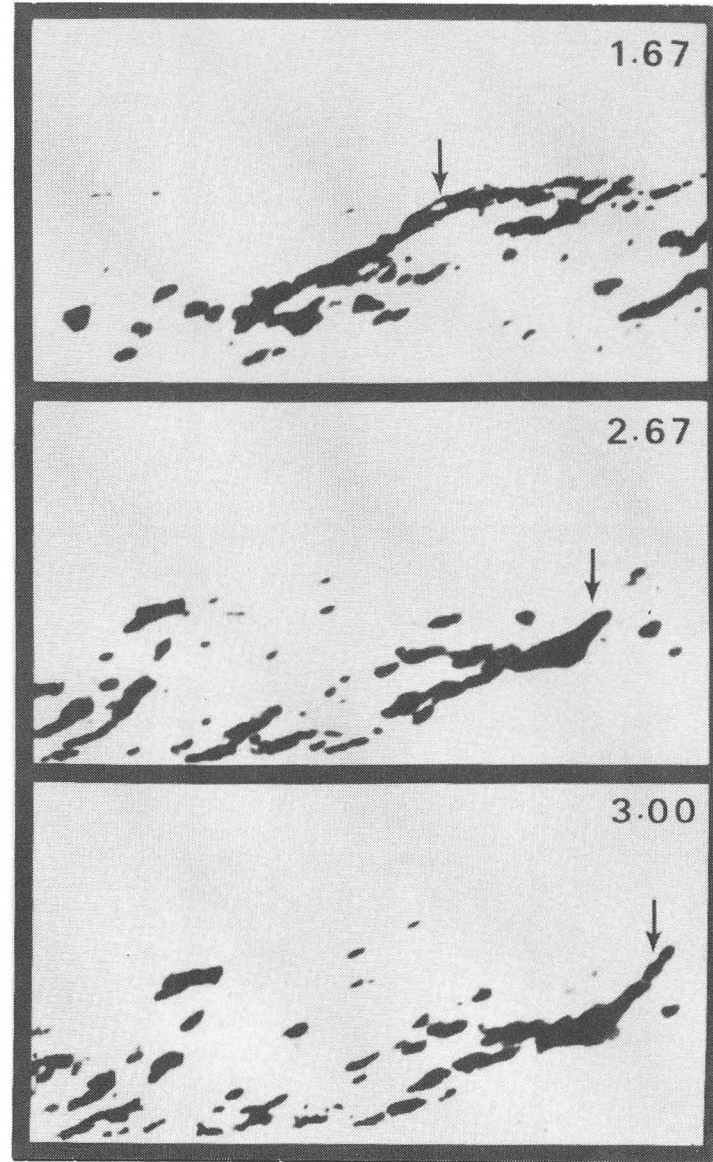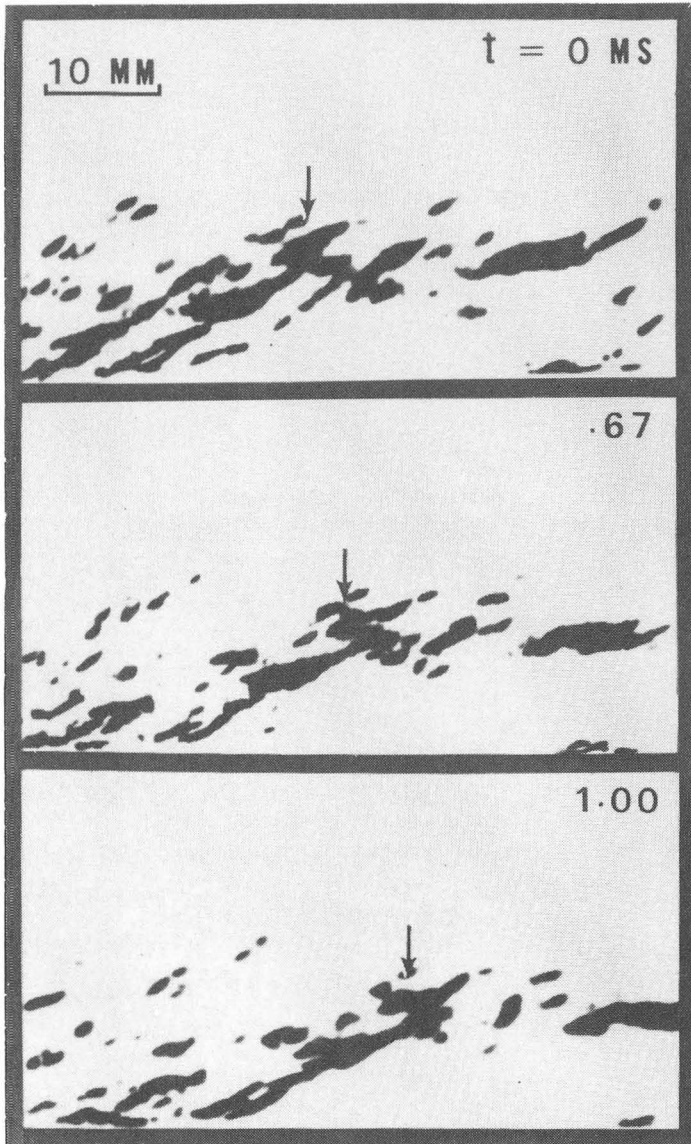
Fig. 14b Schlieren Pictures of the Reacting Boundary
Layer Farther Downstream

XBB 817-6450

72
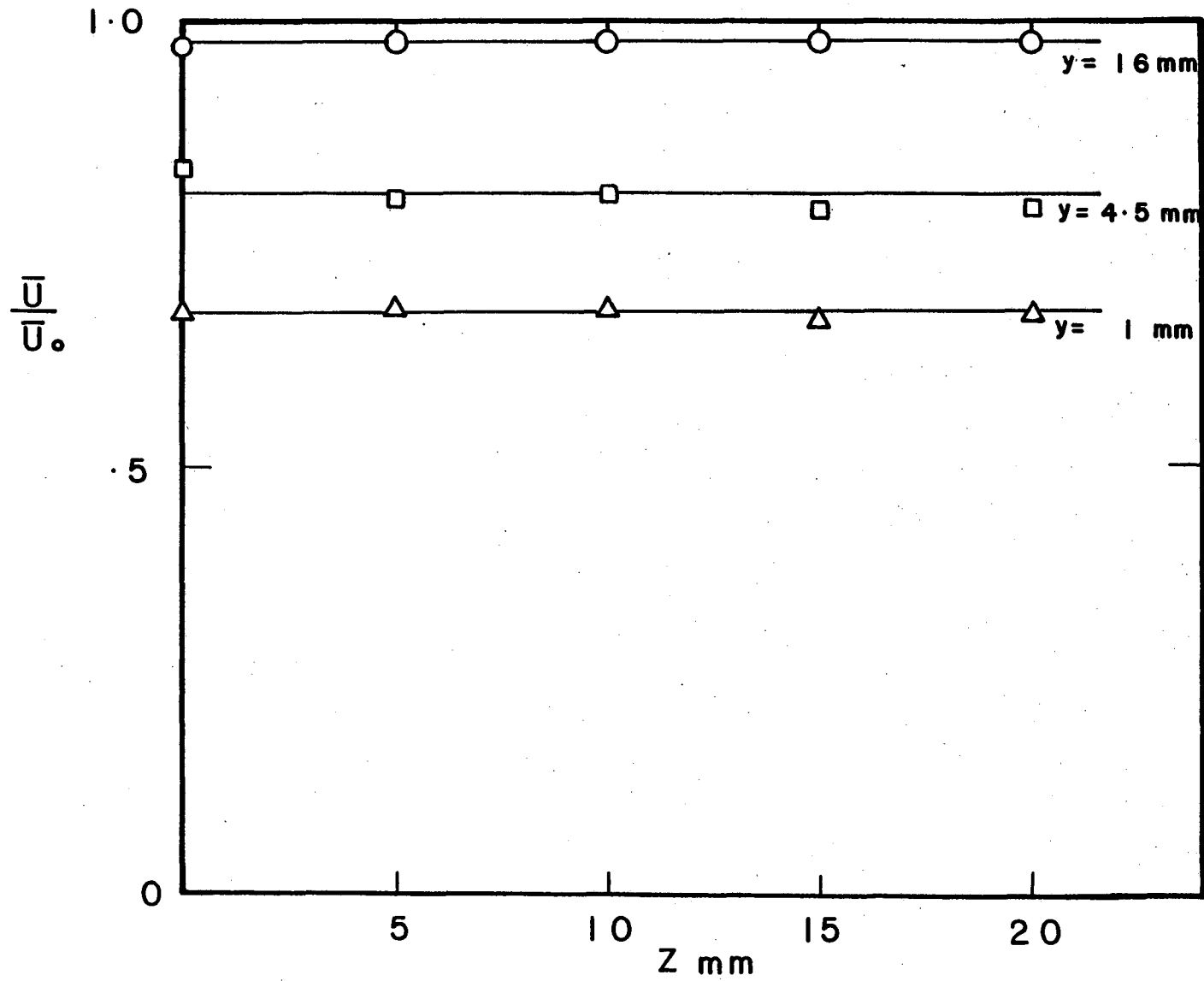
Fig. 15   Mean Velocity Profiles in the Z-Direction at x = 150 mm
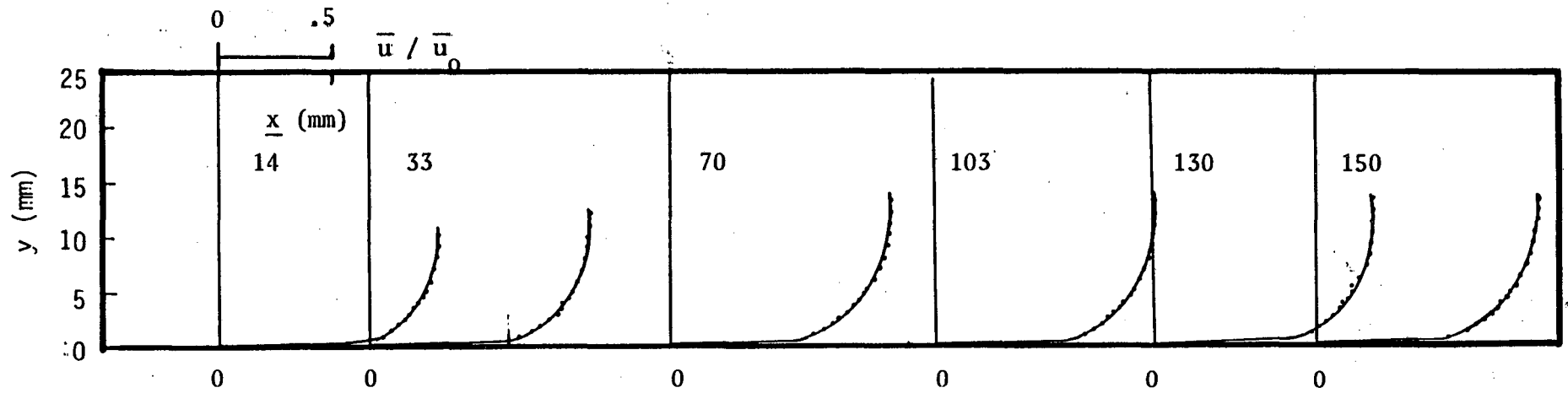
a. Isothermal
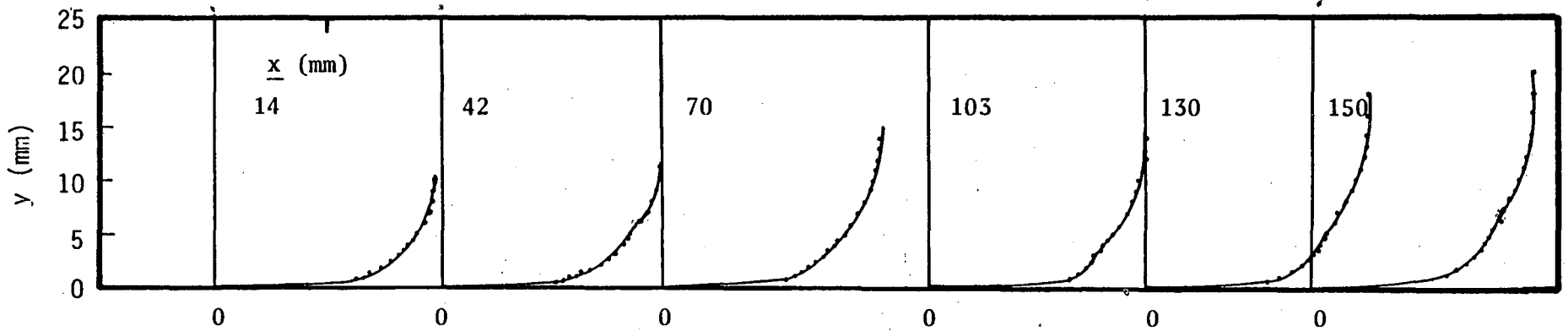
b. Heated

Fig. 16   Mean Streamwise Velocity Profiles
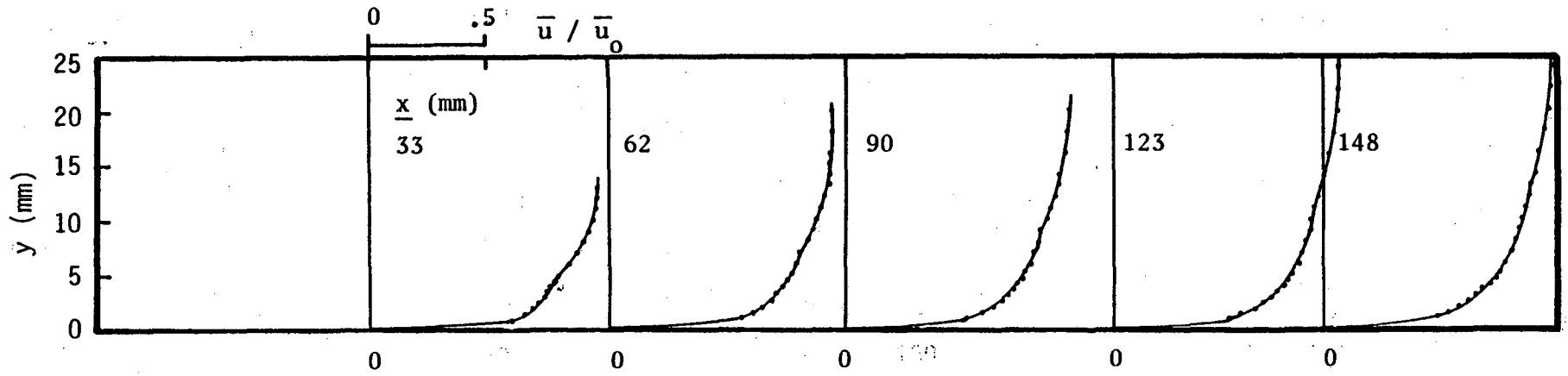
c. Reacting

Fig. 16   Mean Streamwise Velocity Profiles
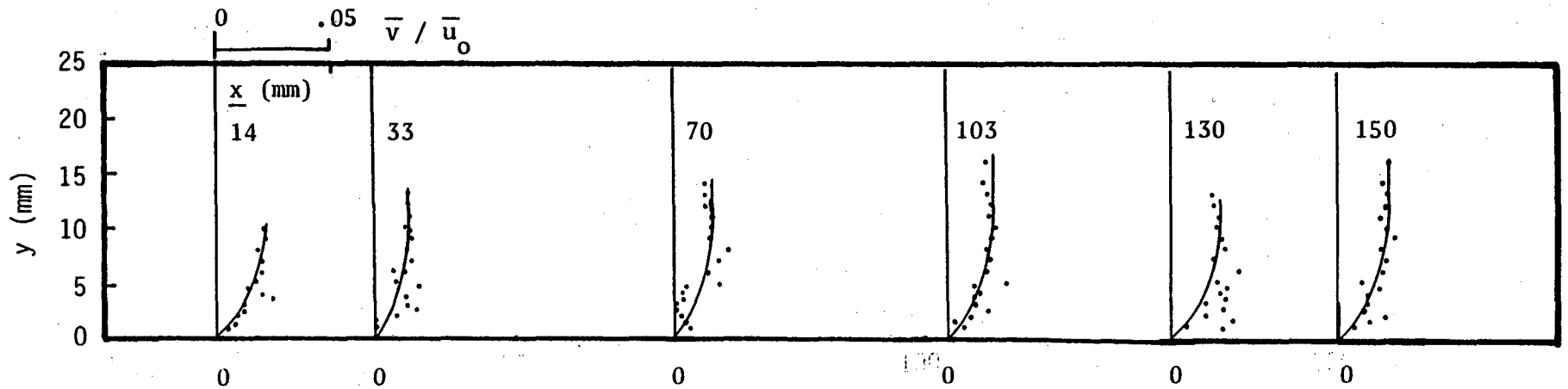
a. Isothermal

Fig. 17   Mean Cross-Stream Velocity Profiles
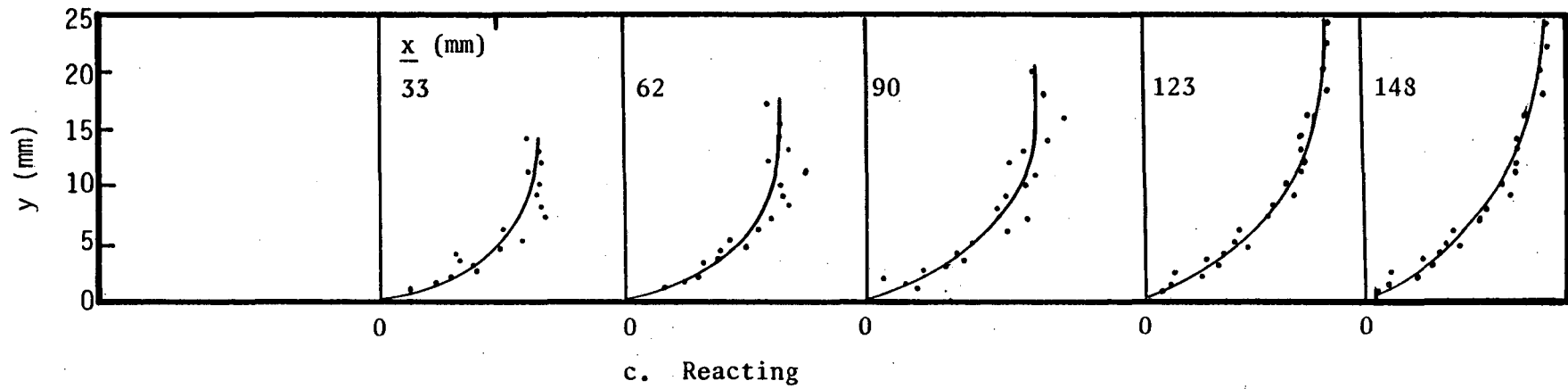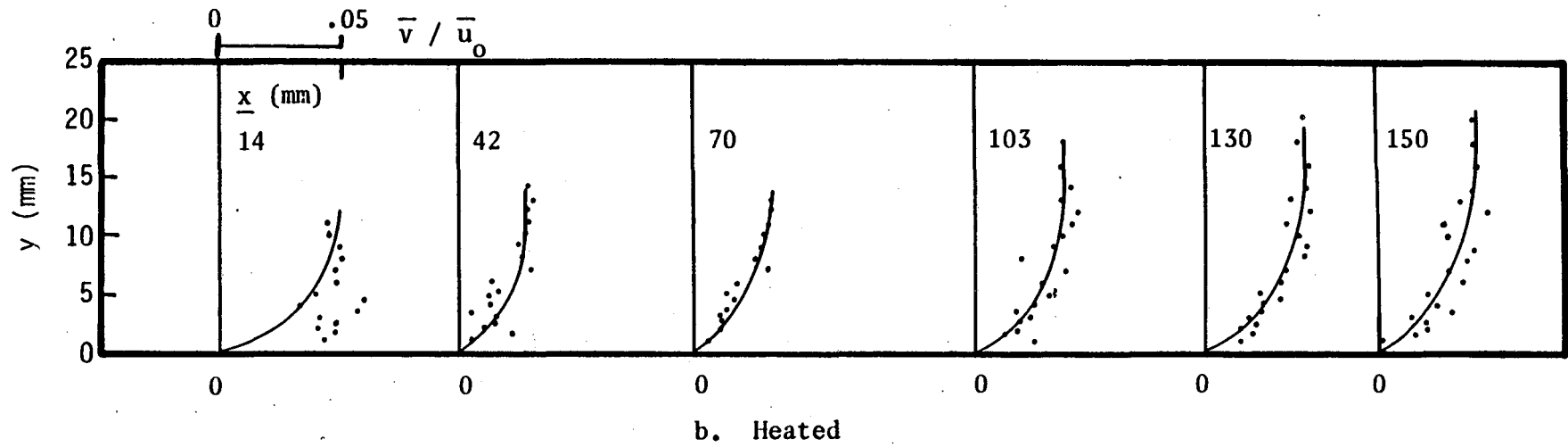
Fig. 17   Mean Cross-Stream Velocity Profiles
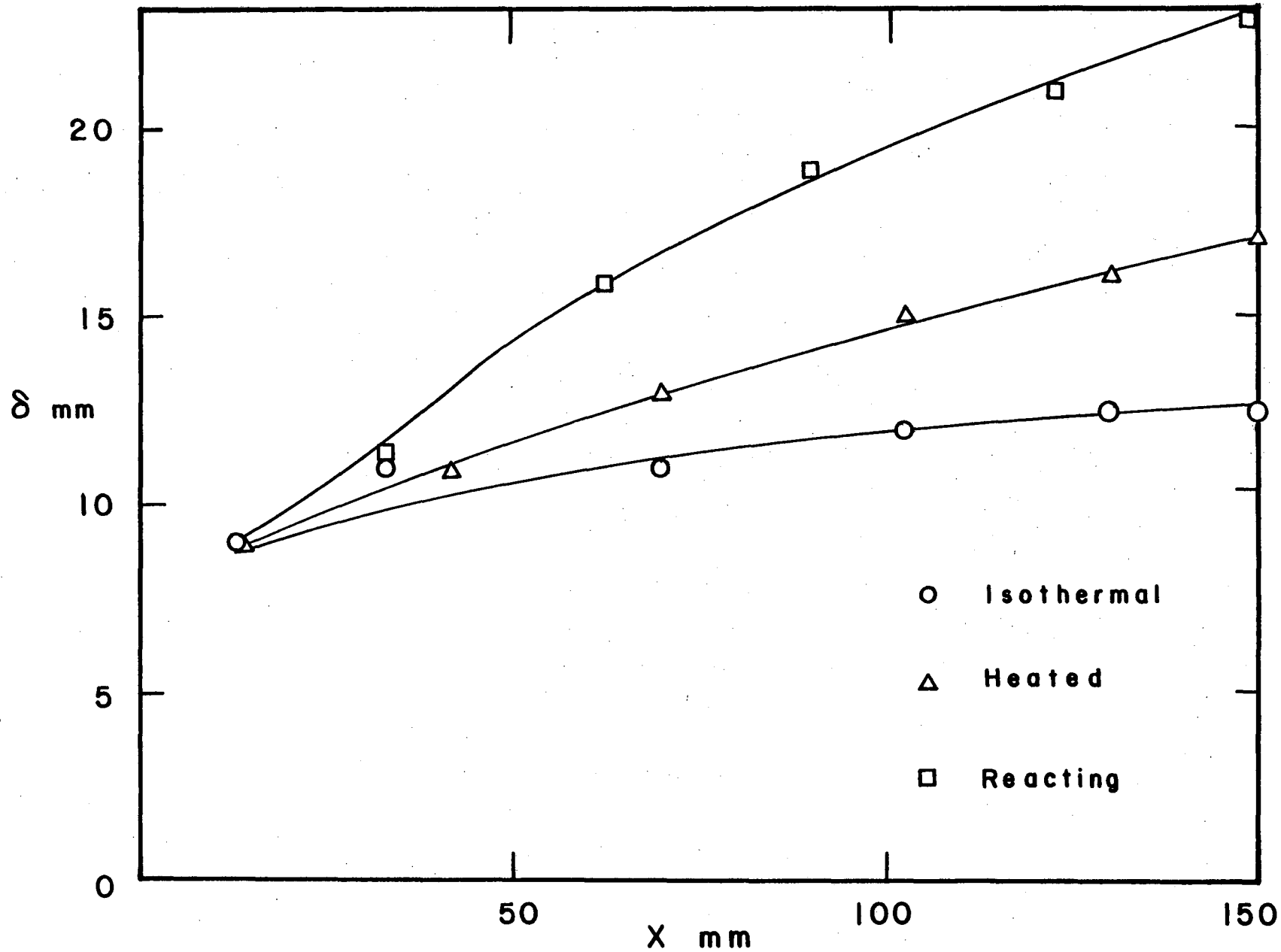
Fig. 18   The Boundary Layer Thickness
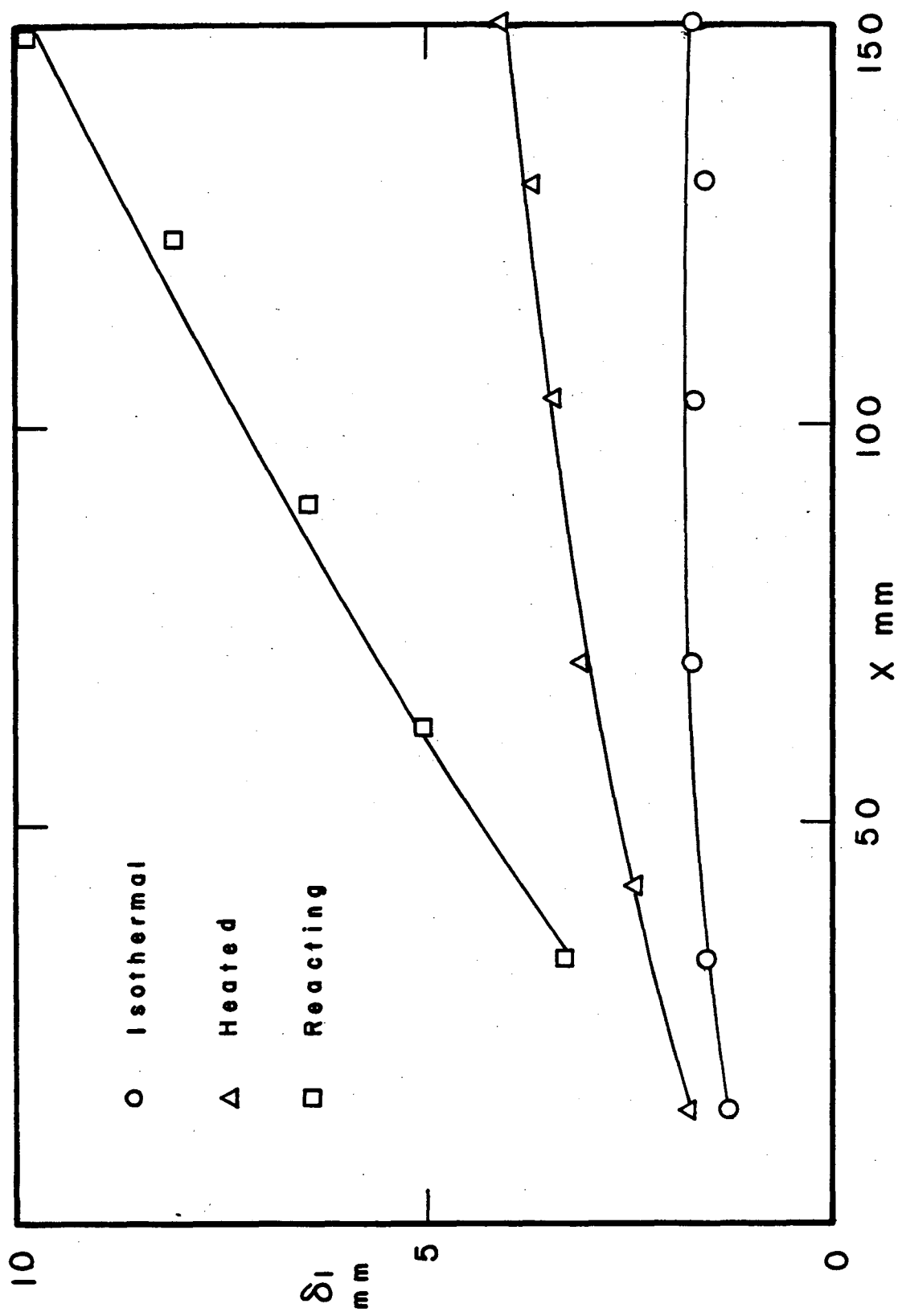
Fig. 19   The Displacement Thickness
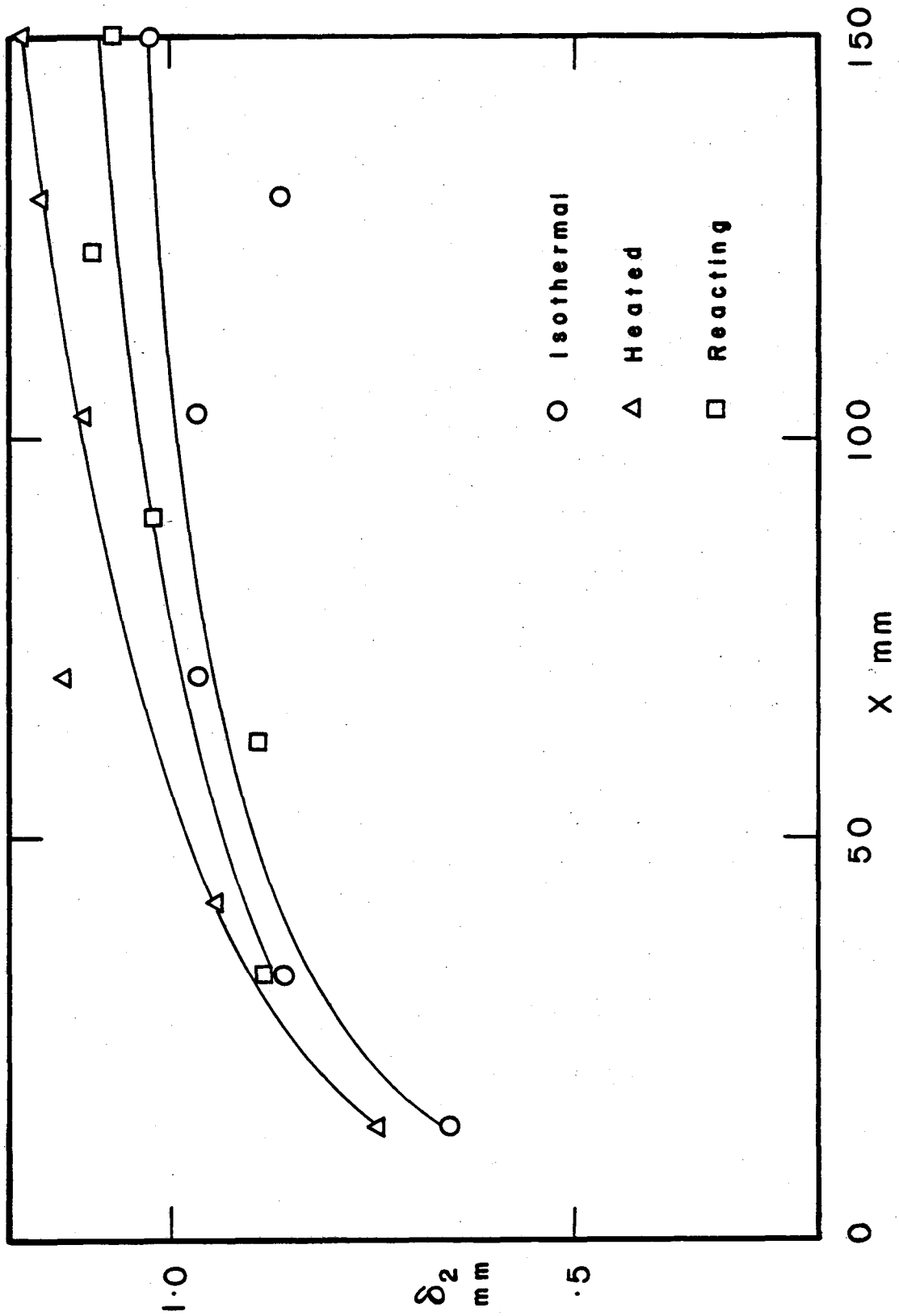
Fig. 20   The Momentum Thickness
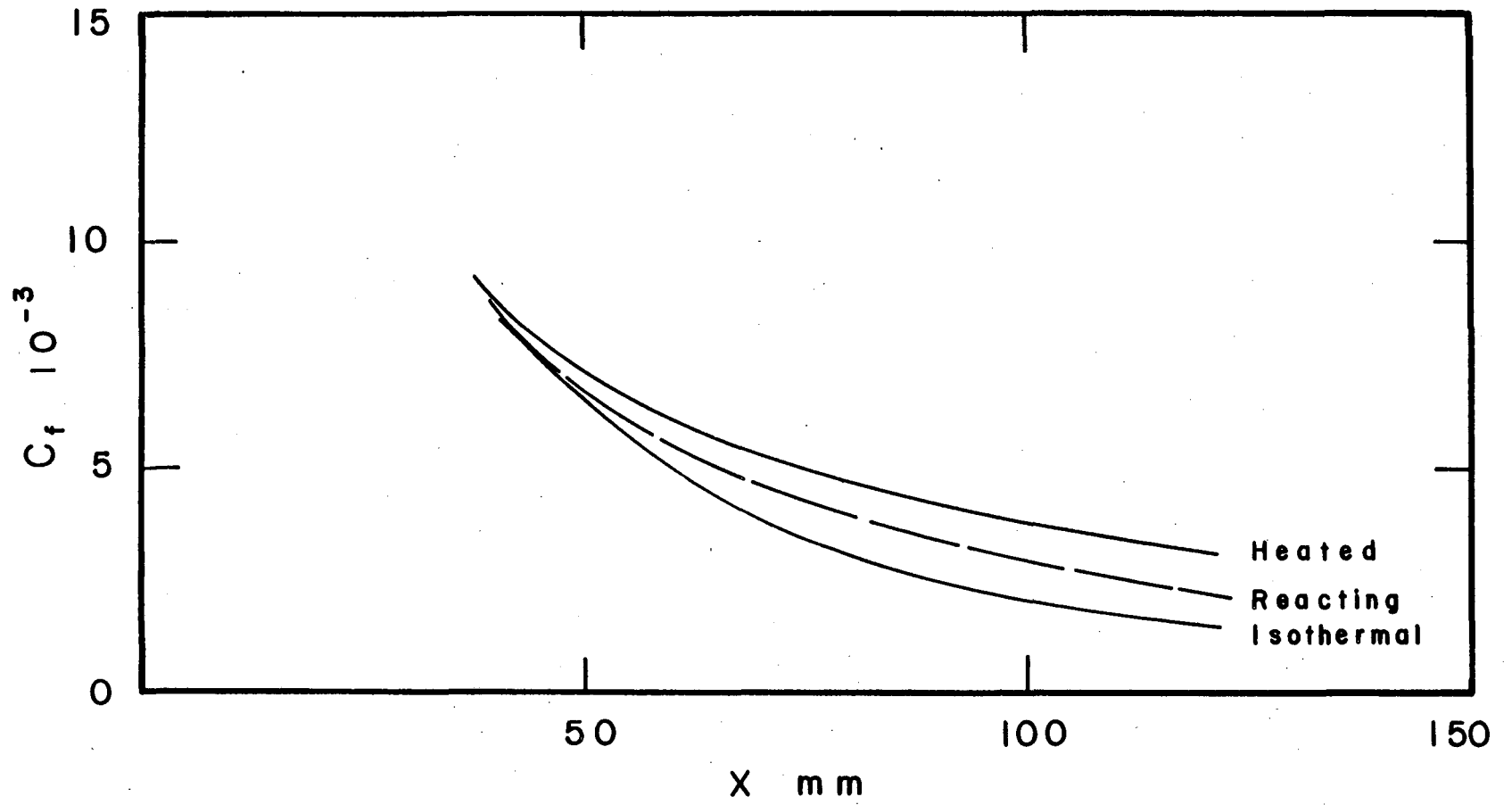
Fig. 21   The Friction Coefficient
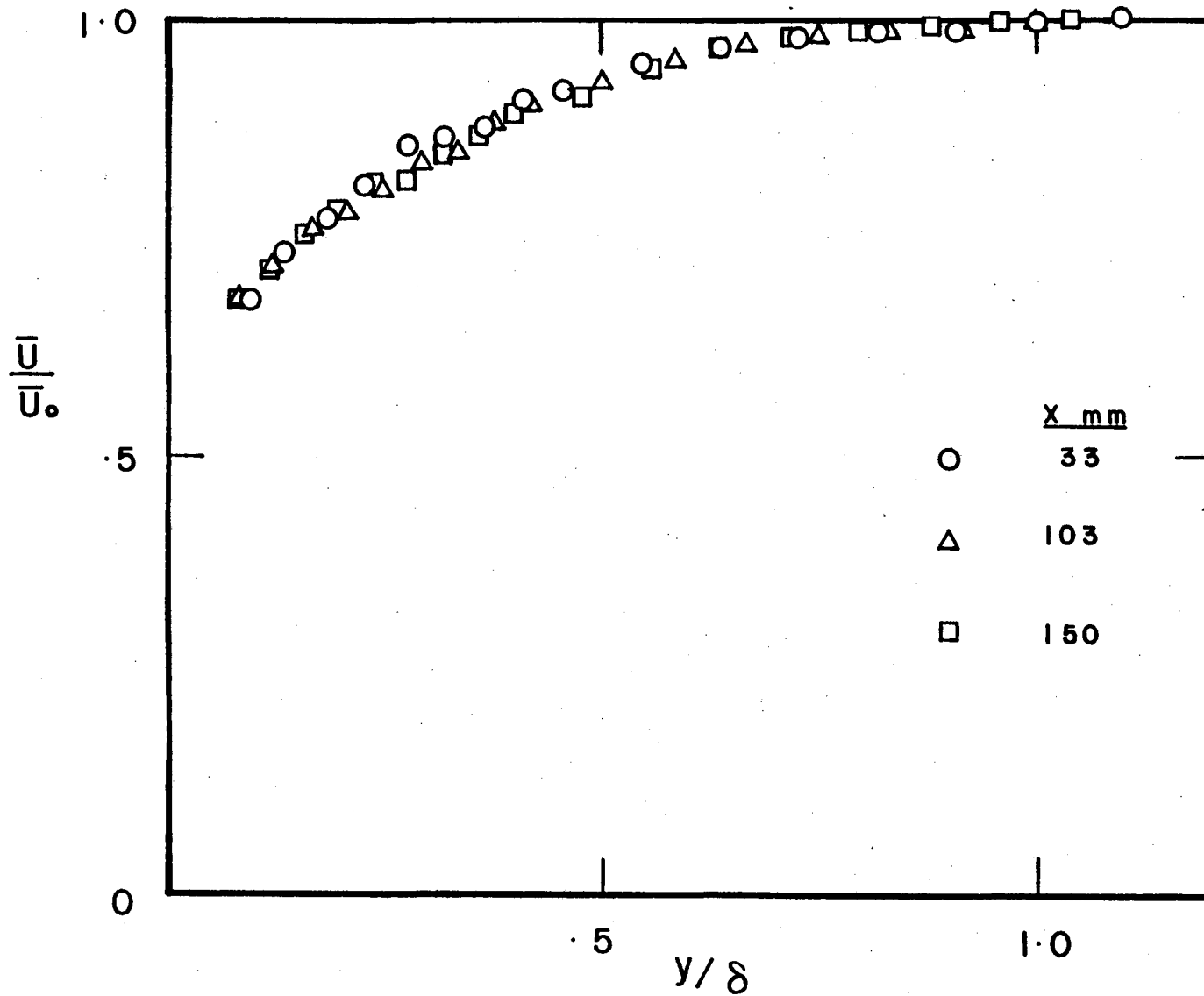
Fig. 22   Mean Streamwise Velocity as a Function of y/δ for the
Isothermal Boundary Layer

$$(\bar{\rho} - \rho_w) / (\rho_o - \rho_w)$$

a. Heated

b. Reacting
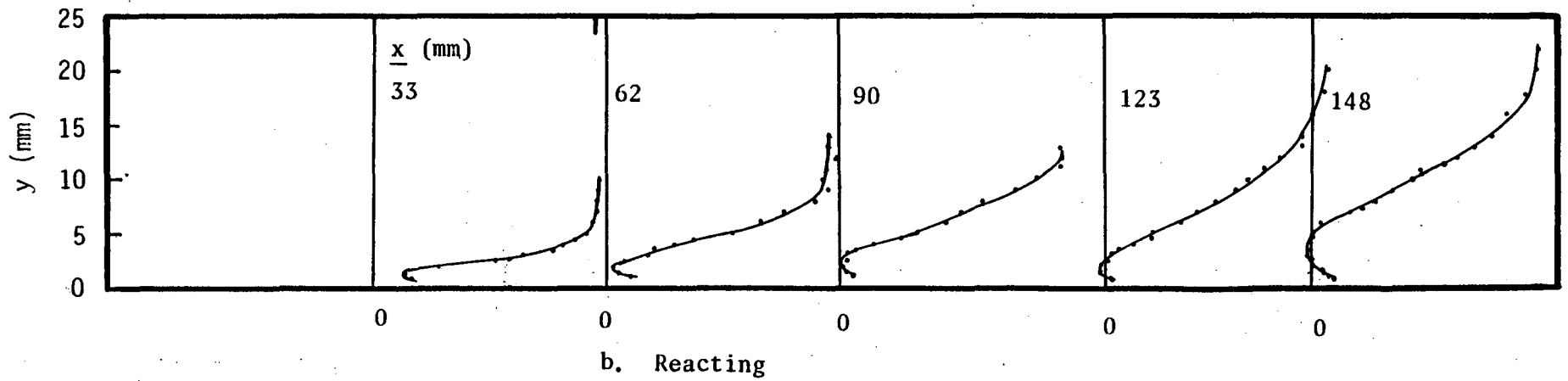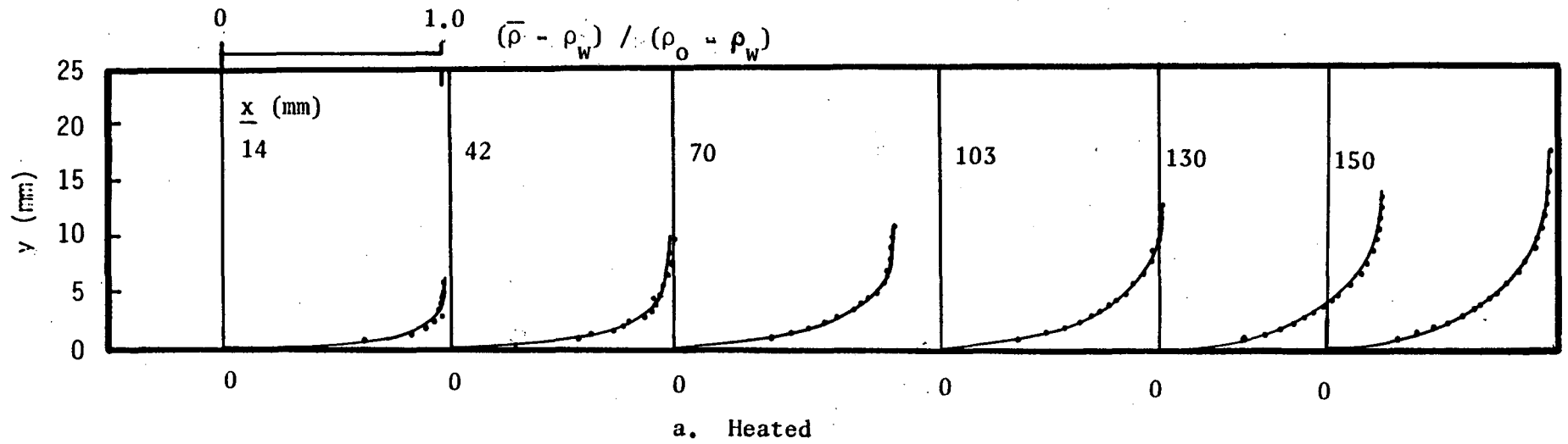
Fig. 23   Mean Density Profiles
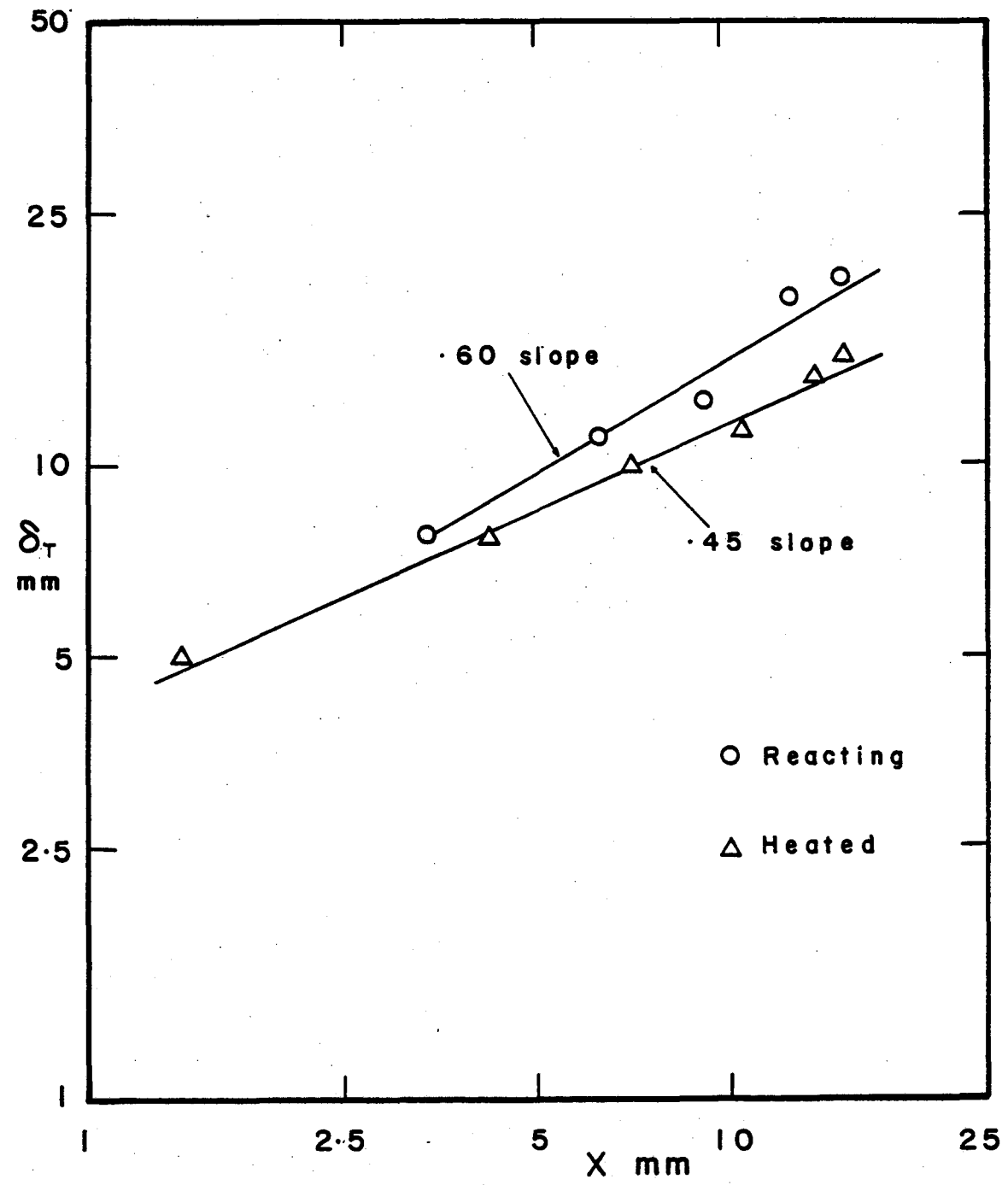
Fig. 24   The Thermal Boundary Layer Thickness
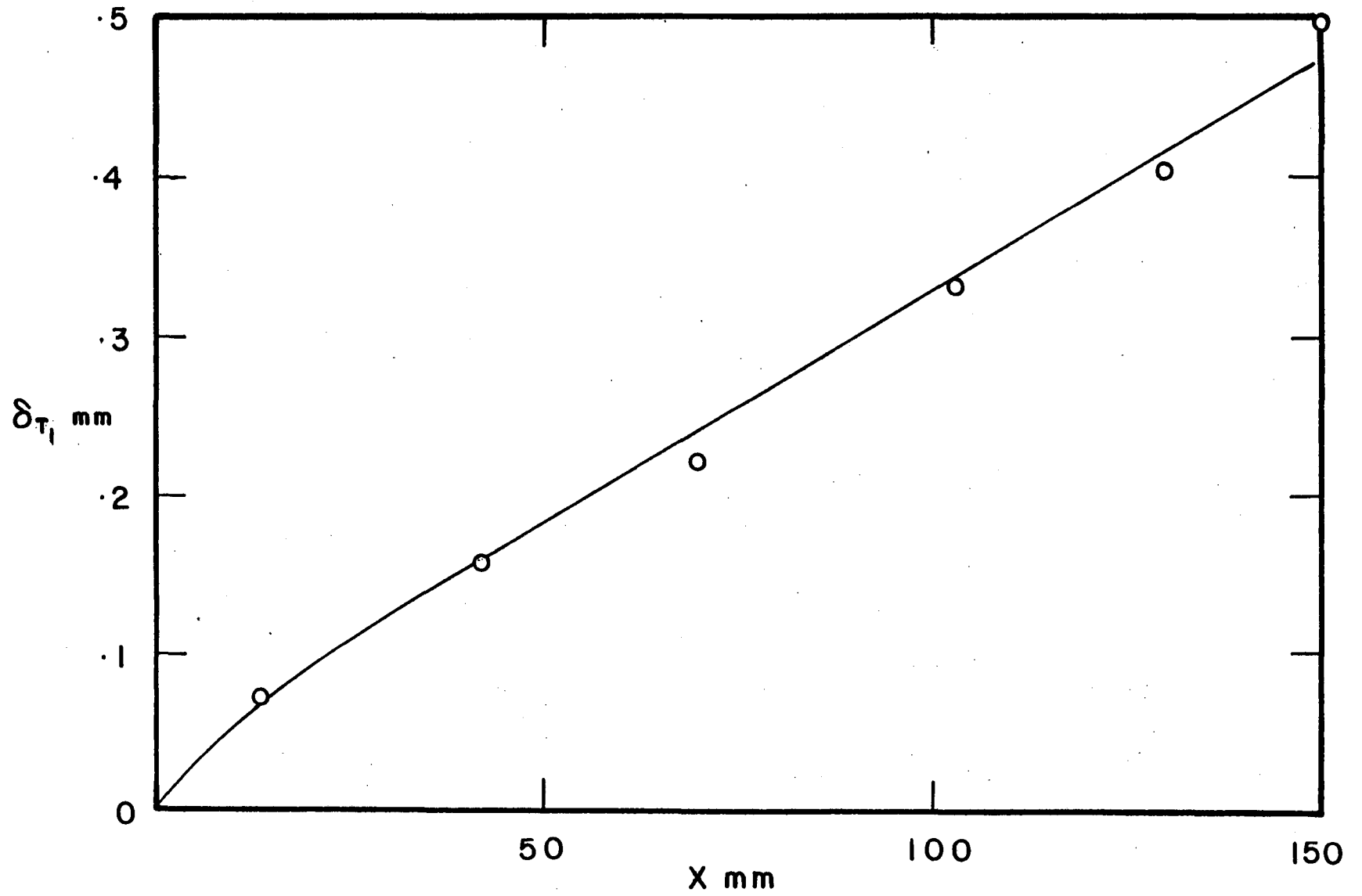
Fig. 25   The Enthalpy Thickness of the Stepwise Heating Boundary Layer
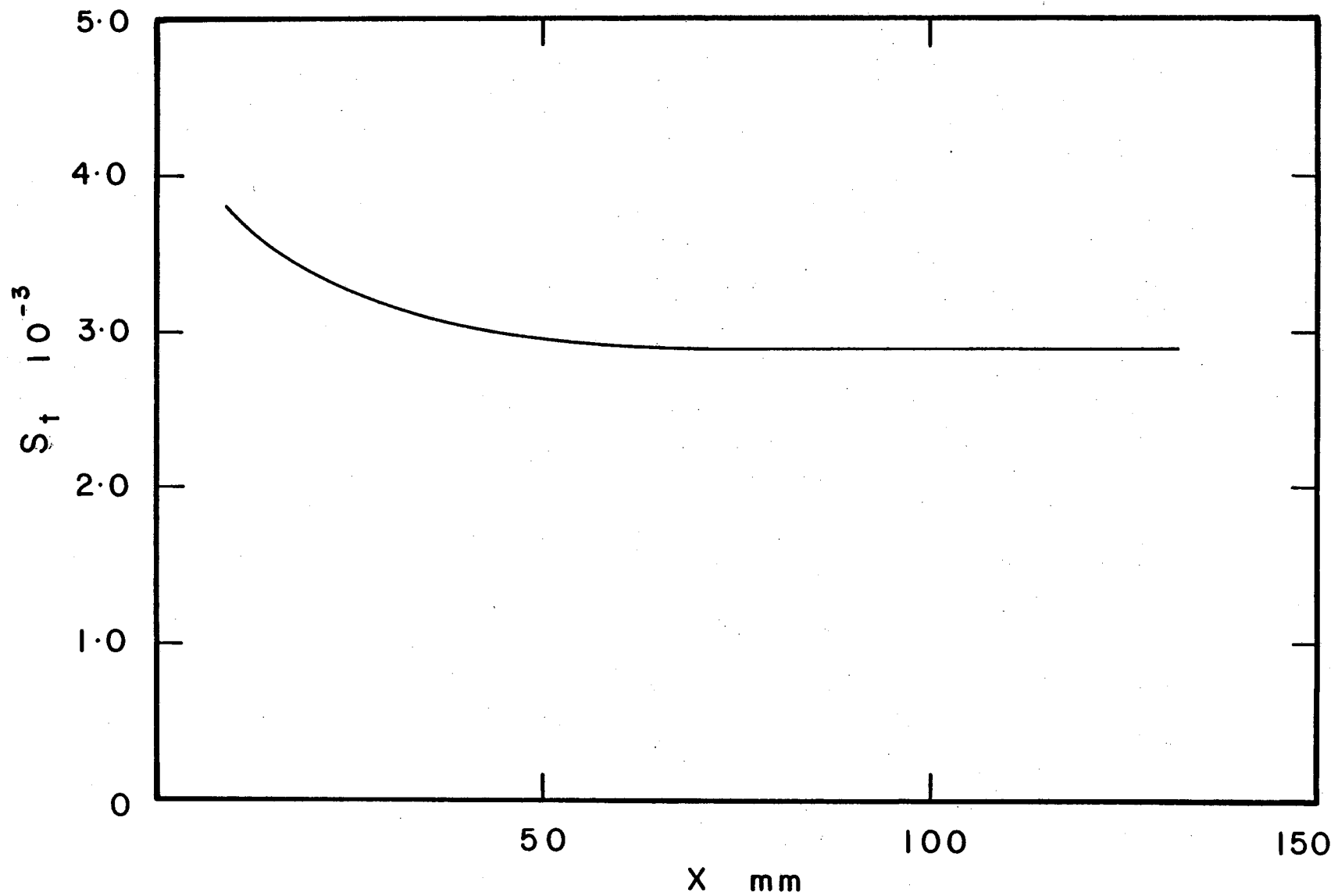
Fig. 26   The Stanton Number of the Stepwise Heating Boundary Layer
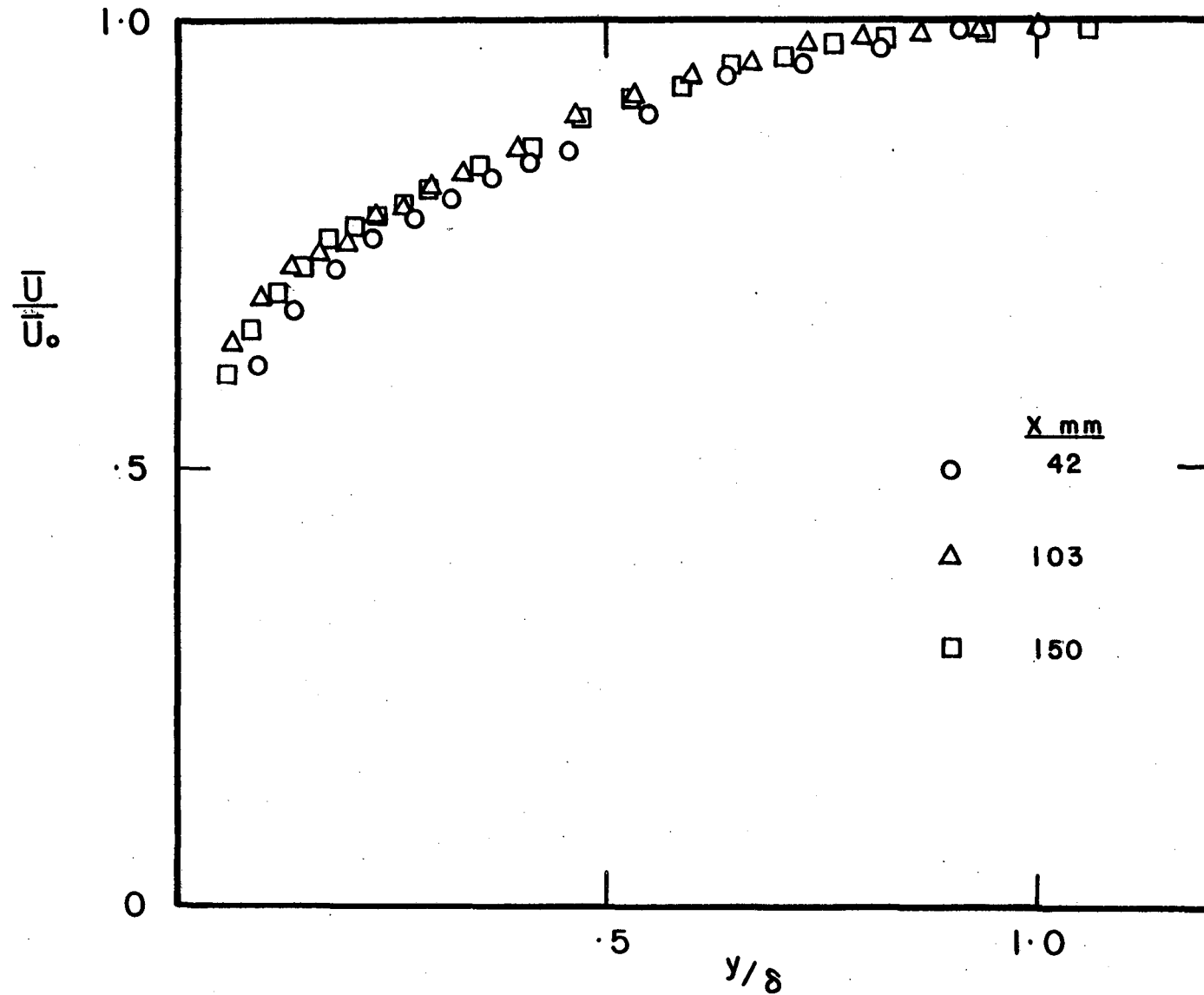
Fig. 27   The Mean Velocity as a Function of y/δ for the Stepwise
           Heating Boundary Layer
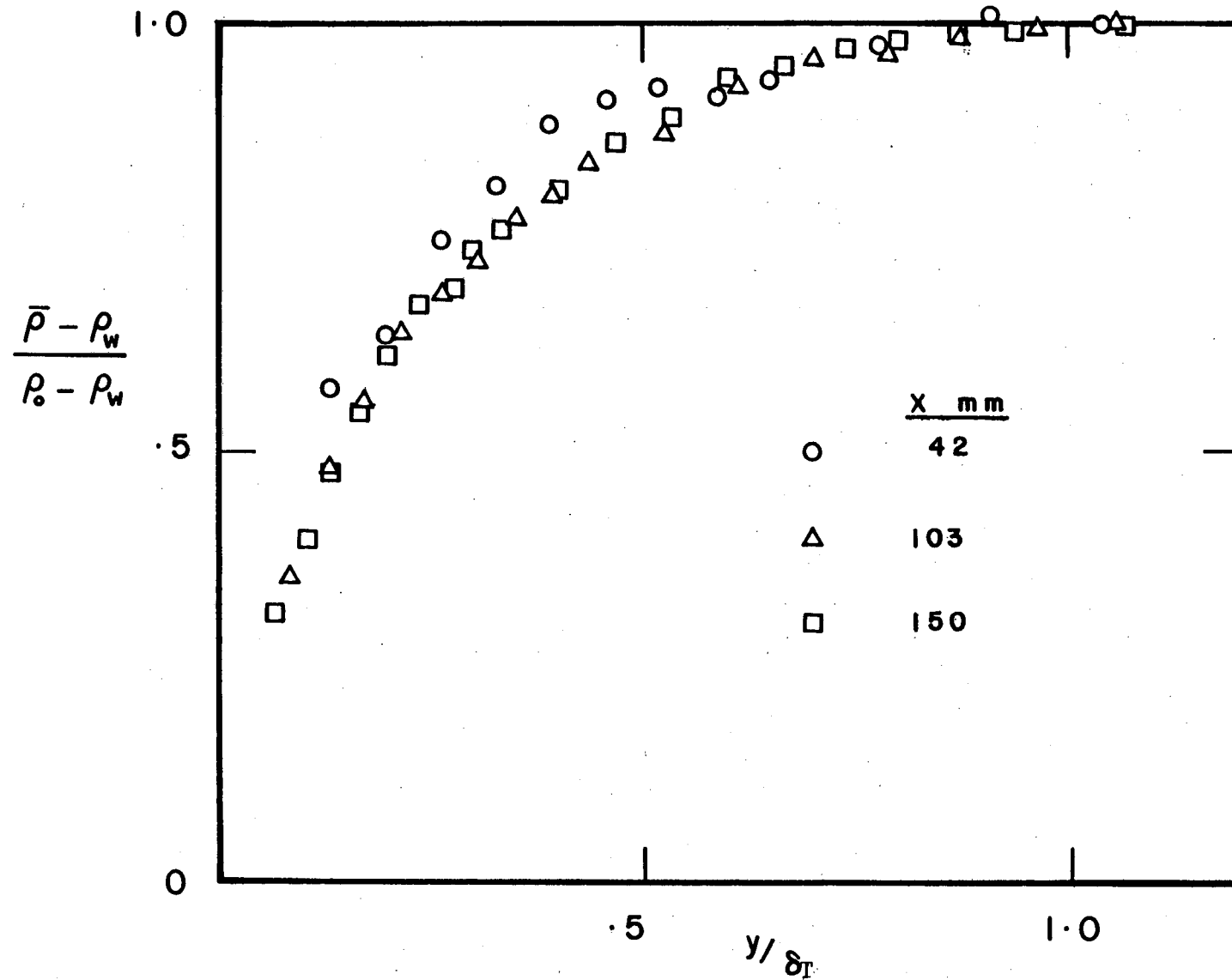
Fig. 28   The Mean Density Profiles of the Heated Boundary Layer as a
Function of y/δ_T
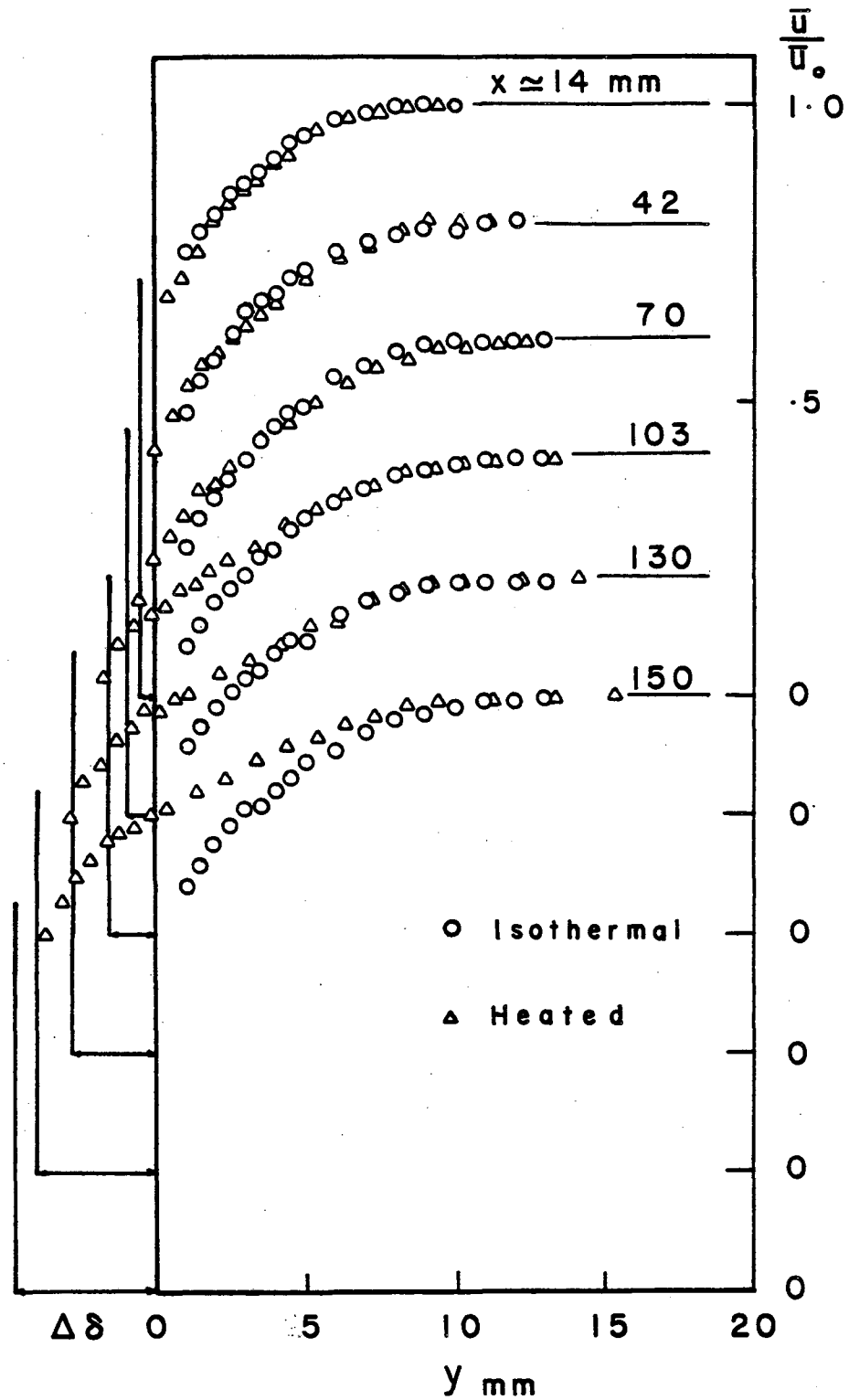
Fig. 29   Mean Velocity Profiles of the Isothermal and the
Heated Boundary Layer with the Origin of the Latter
Being Shifted by $\Delta\delta$ ($= \delta_{heated} - \delta_{iso}$) in the
y-Direction
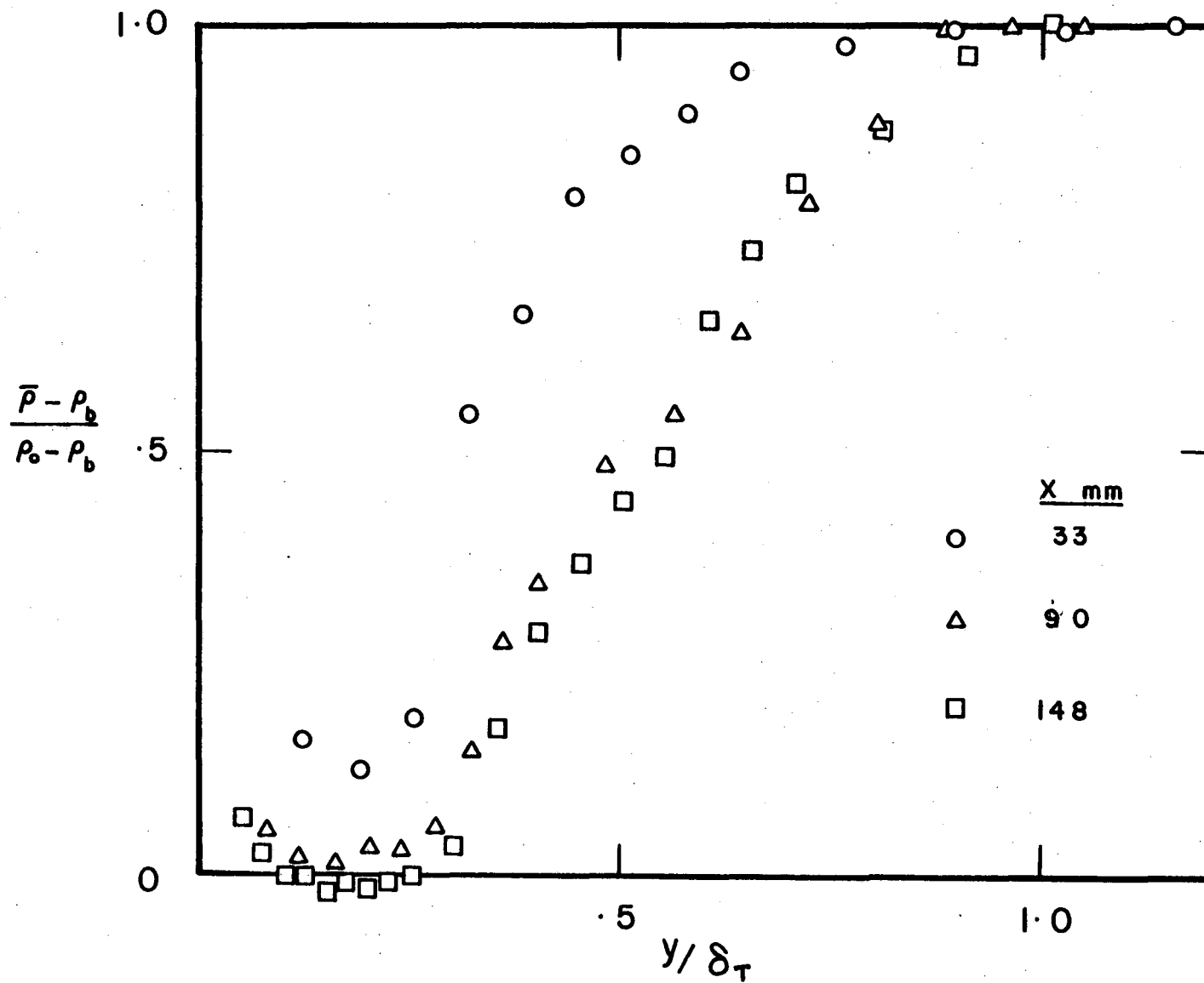
Fig. 30   Typical Mean Density Profiles of the Reacting Boundary Layer
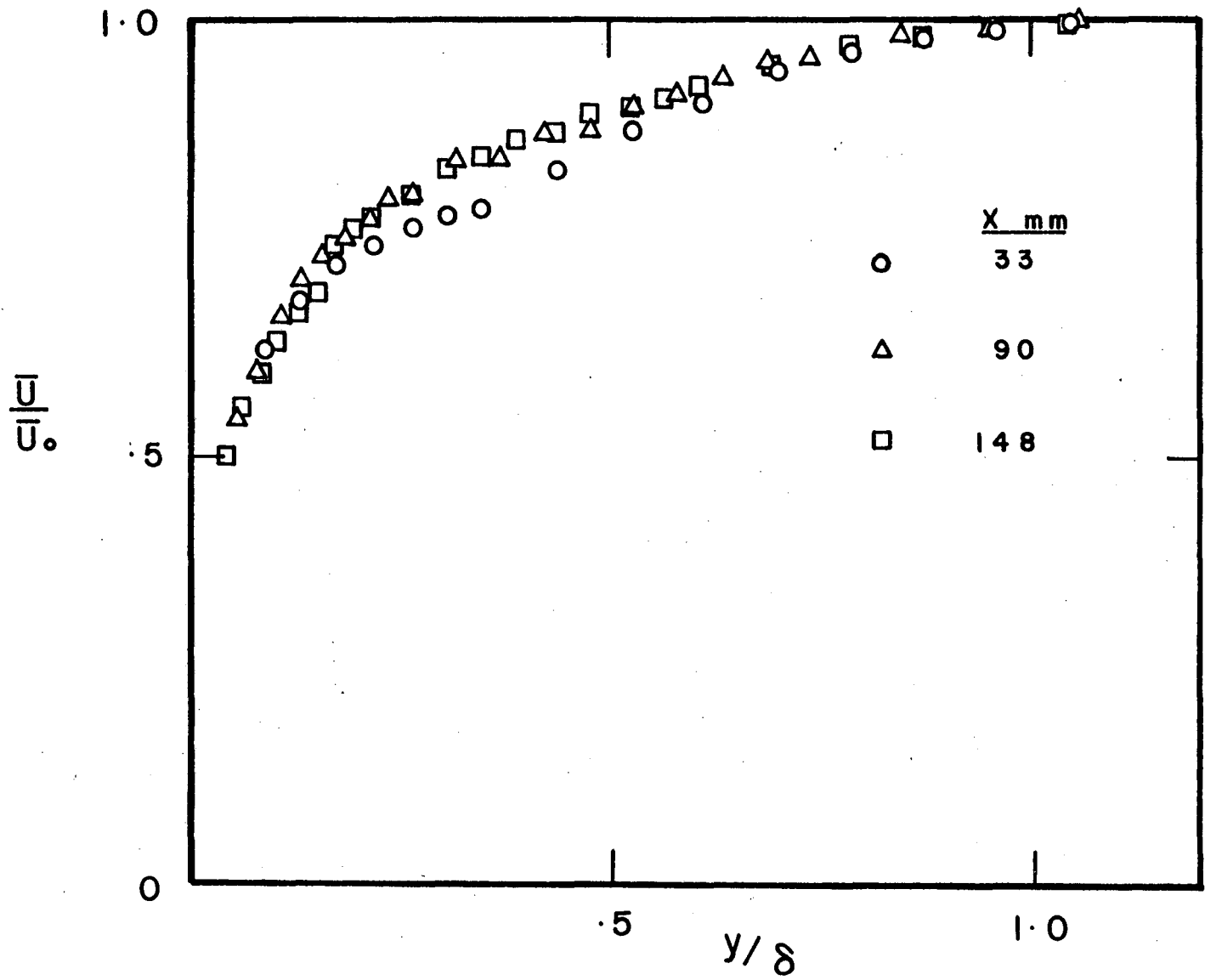
Fig. 31   Typical Mean Velocity Profiles of the Reacting Boundary Layer
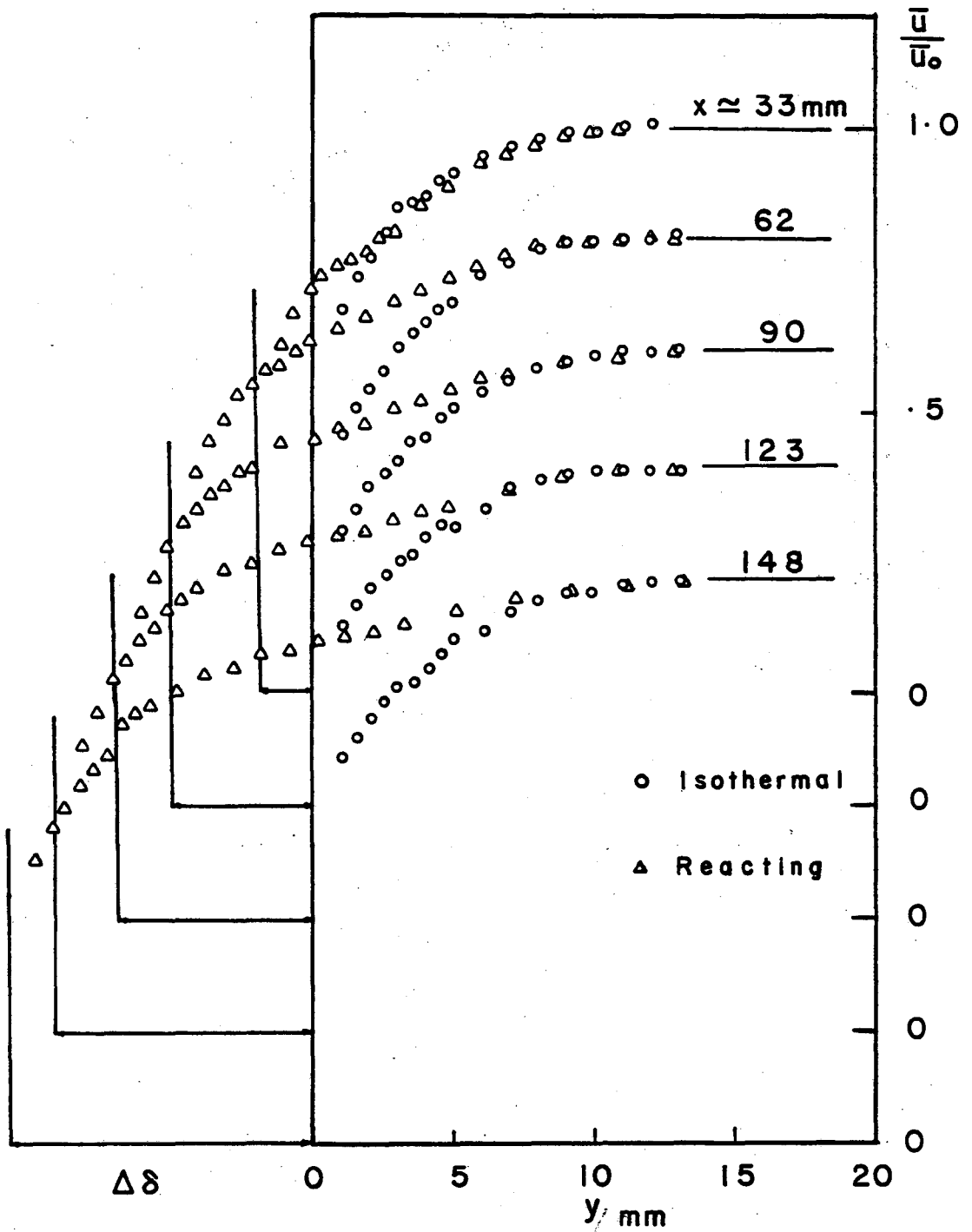
Fig. 32   Mean Velocity Profiles of the Isothermal and the
Reacting Boundary Layer with the Origin of the Latter
Being Shifted by $\Delta\delta$ ($= \delta_{react} - \delta_{iso}$) in the
y-Direction
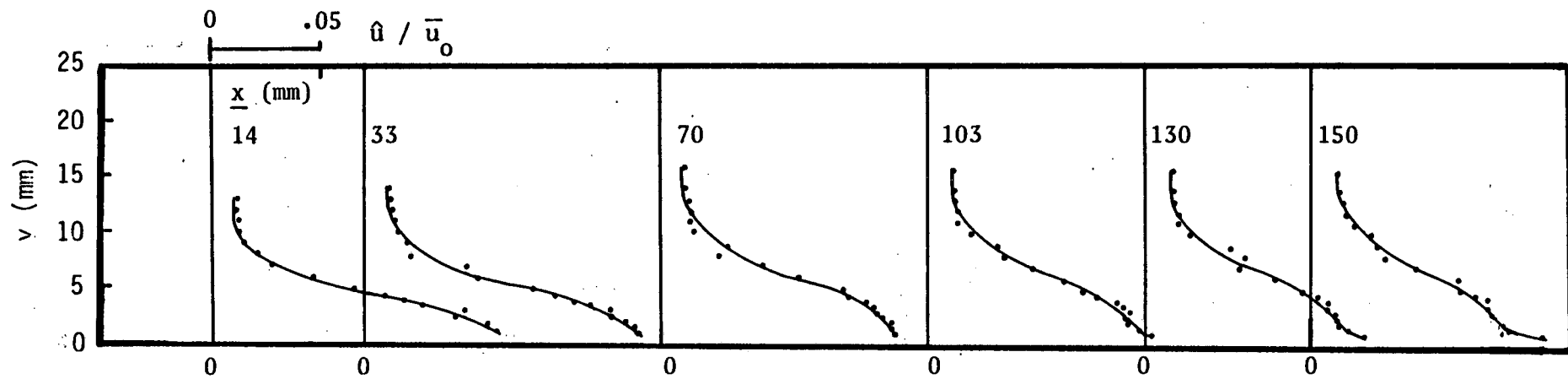
a. Isothermal
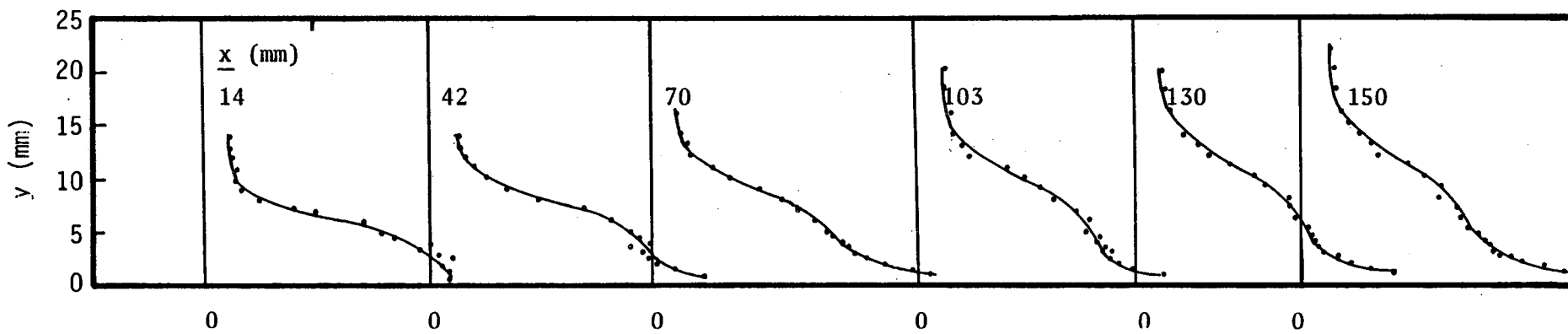
b. Heated

Fig. 33   Root-Mean-Square (RMS) Streamwise Velocity Profiles
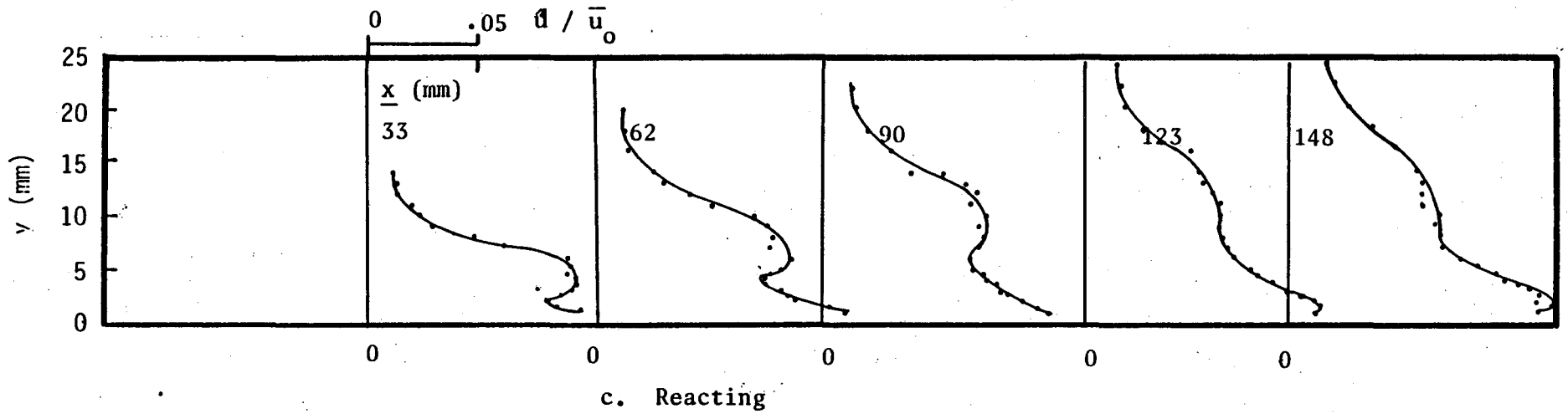
Fig. 33   Root-Mean-Square (RMS) Streamwise Velocity Profiles
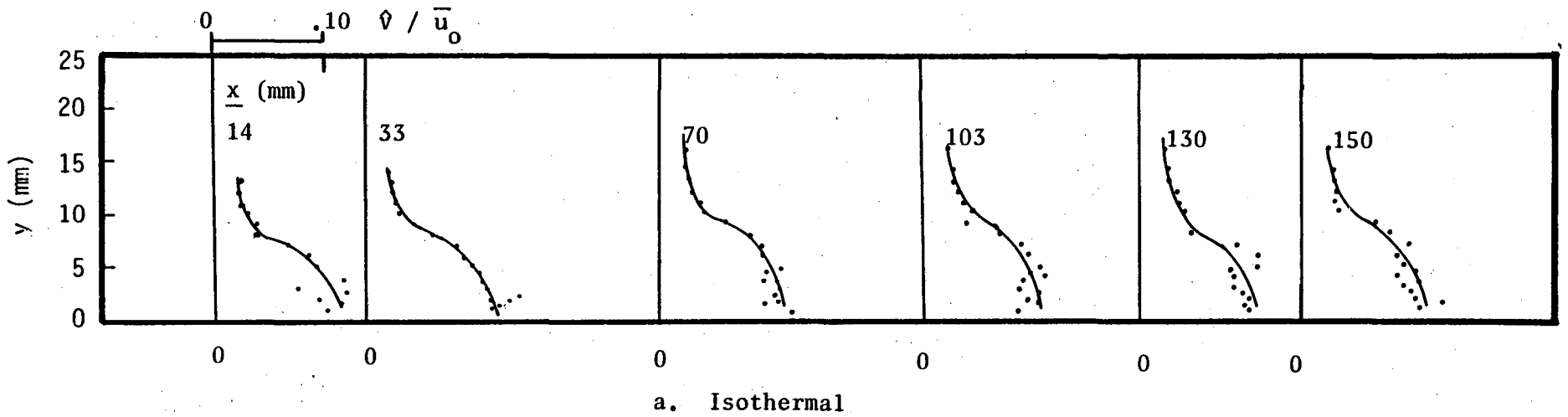
Fig. 34   RMS Cross-Stream Velocity Profiles
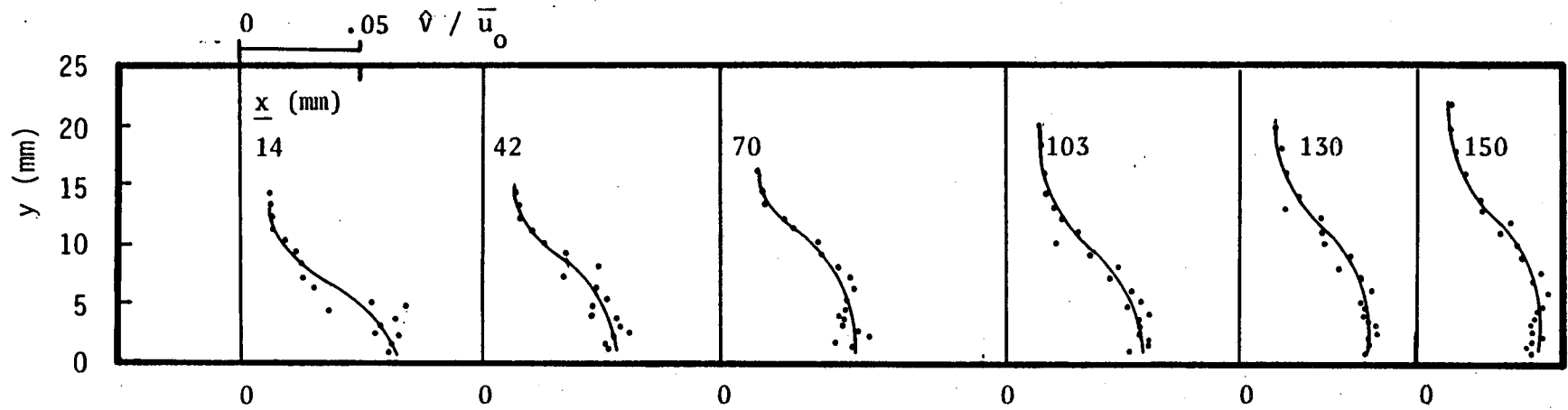
b. Heated
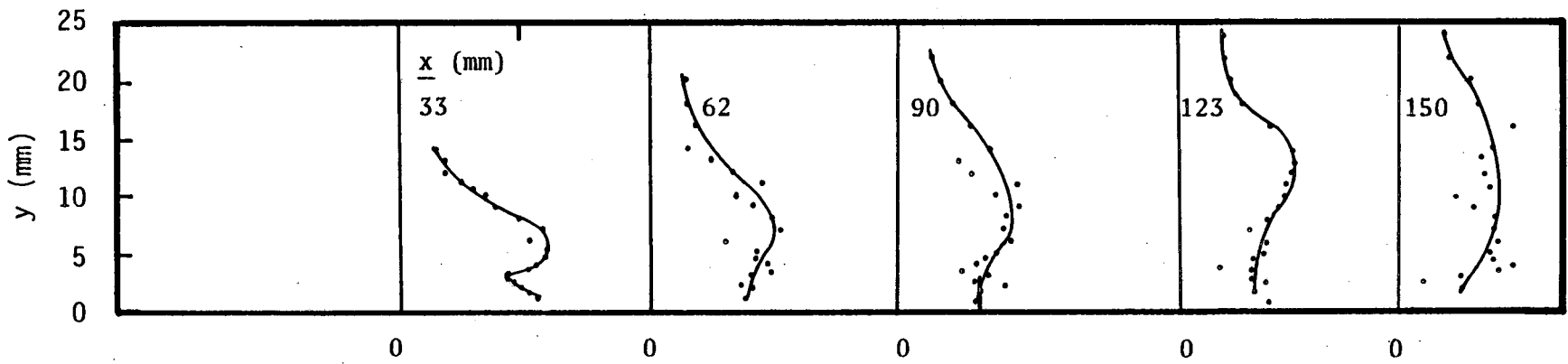
c. Reacting

Fig. 34   RMS Cross-Stream Velocity Profiles
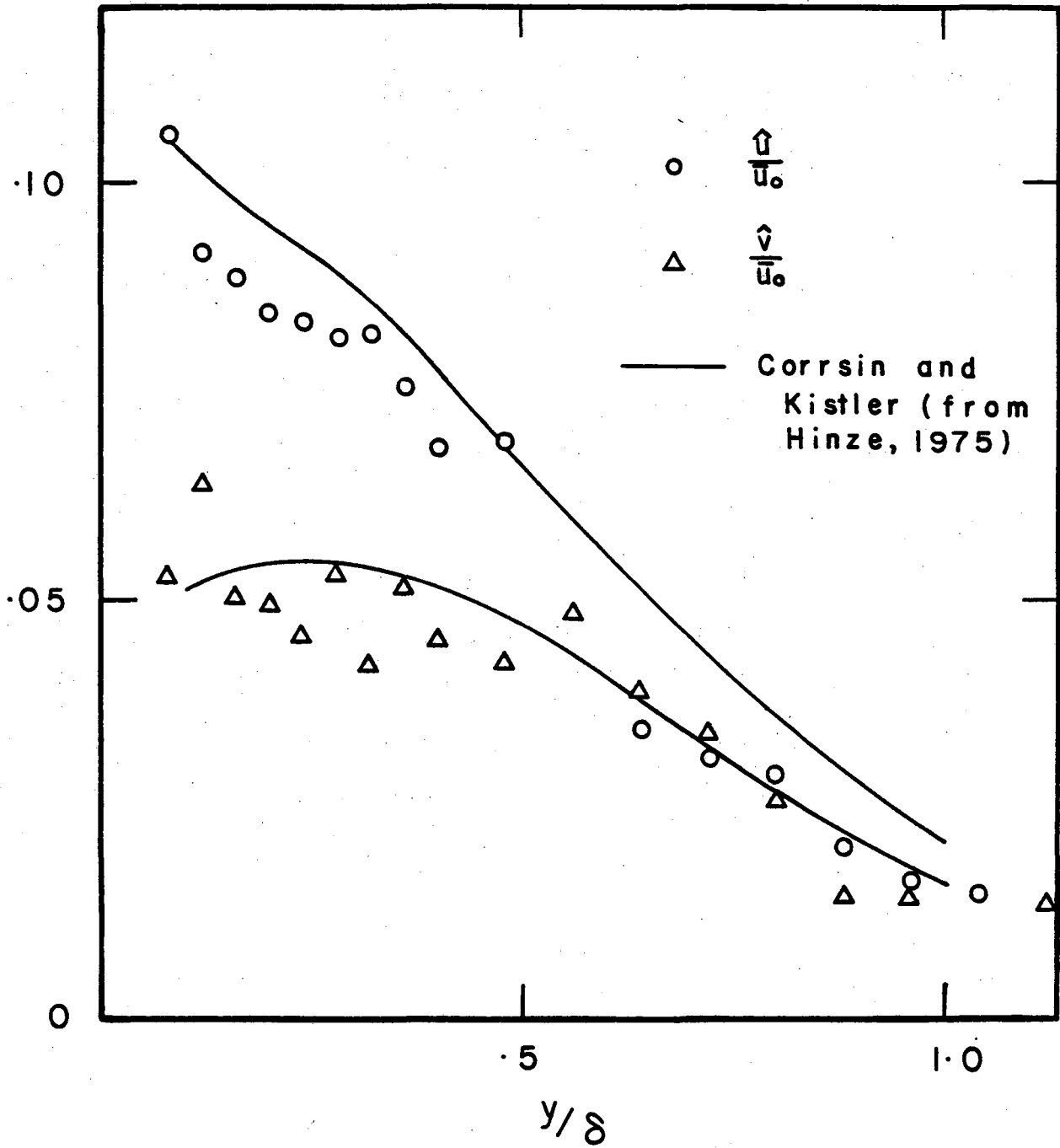
Fig. 35   RMS Velocity Profiles of the Isothermal Boundary Layer as
          Functions of y/δ at x = 150 mm
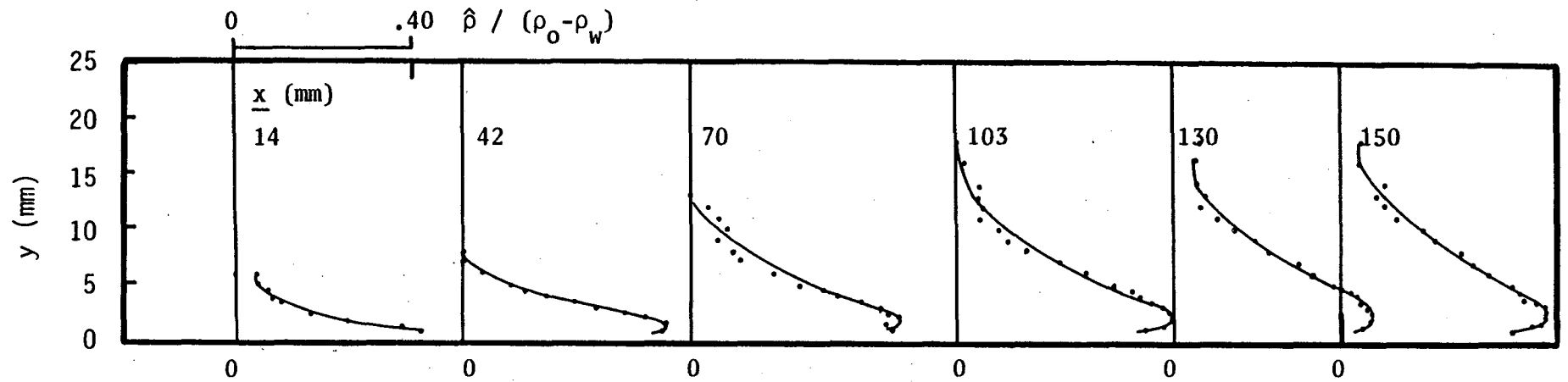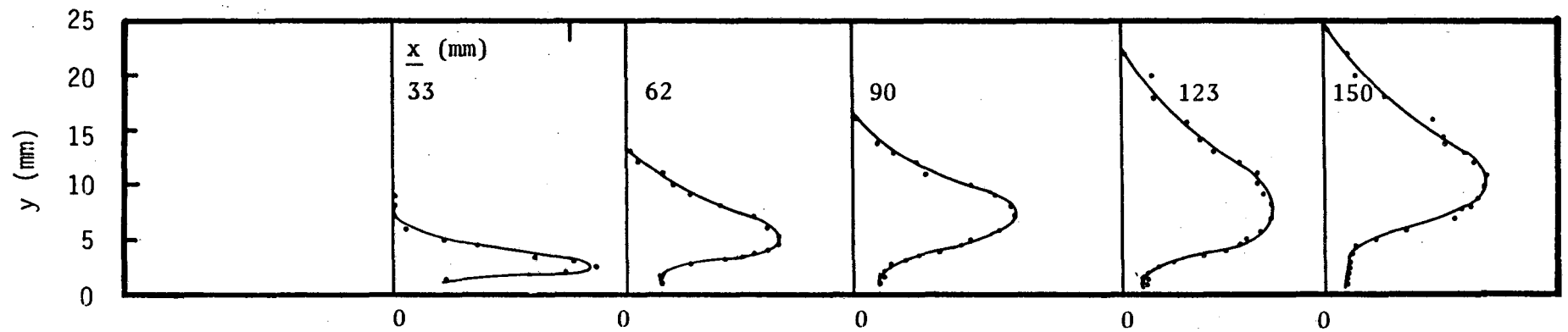
Fig. 36   RMS Density Profiles
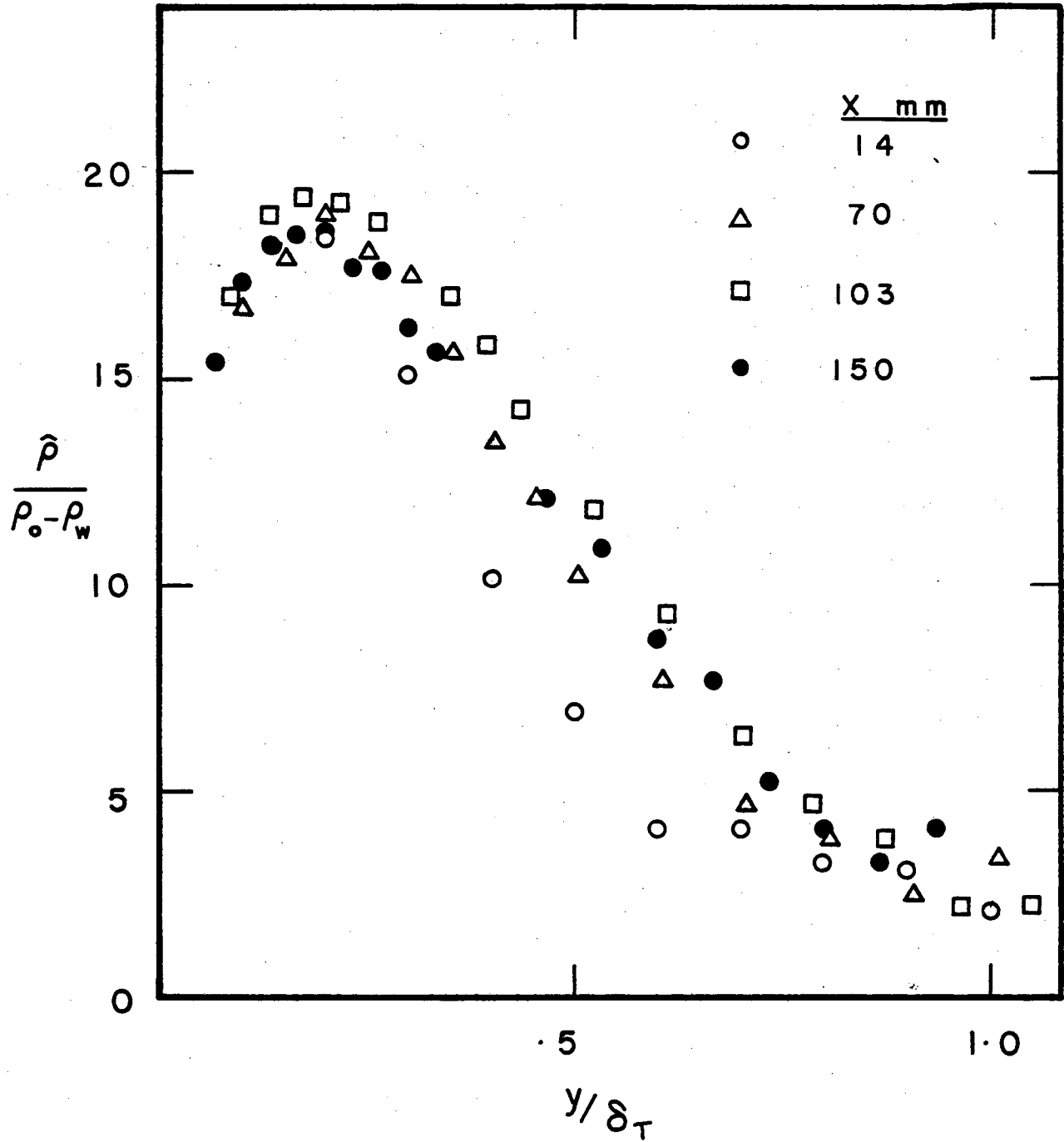
Fig. 37   Typical RMS Density Profiles of the Heated
Boundary Layer
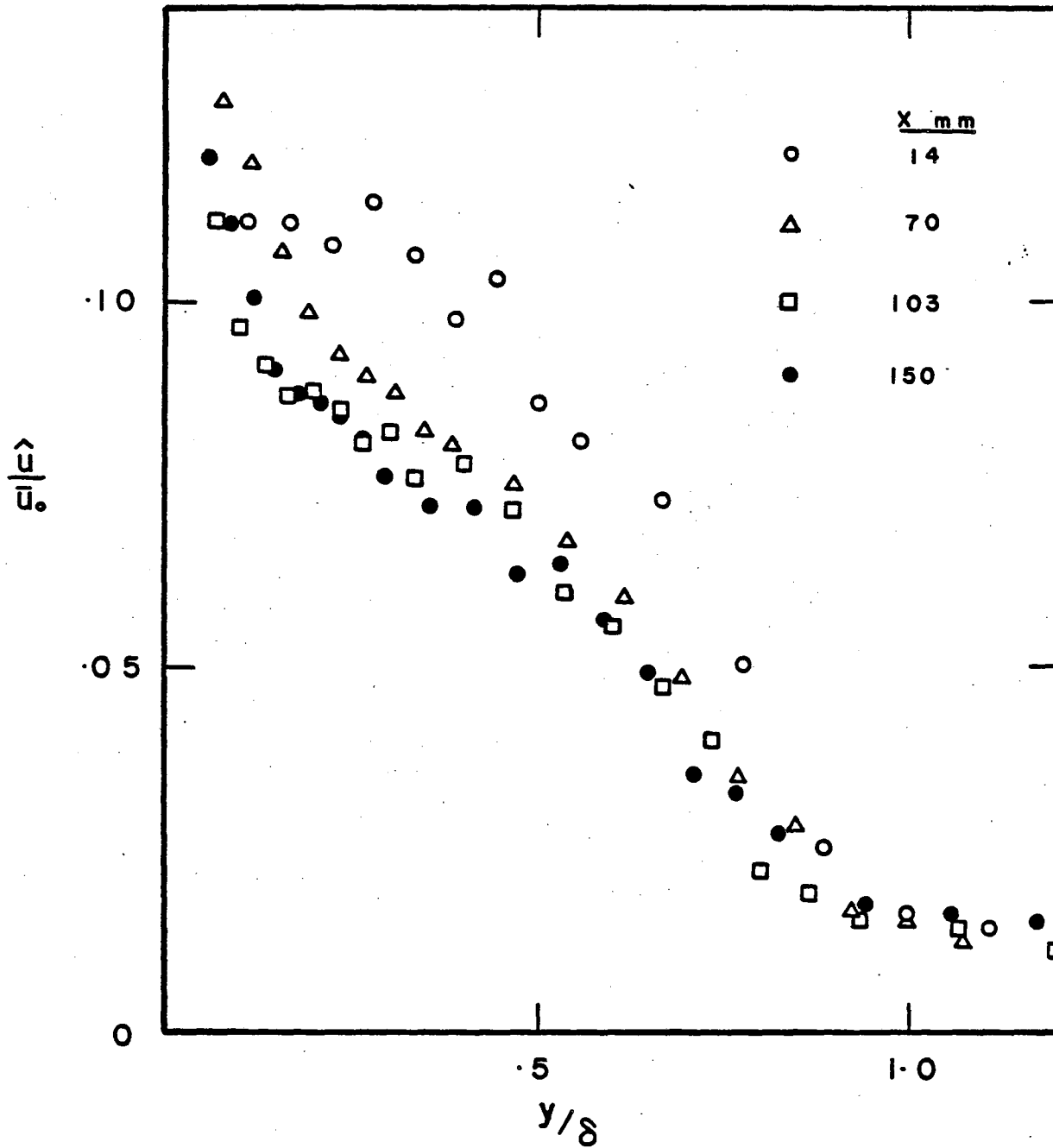
Fig. 38 Typical RMS Velocity profiles of the Stepwise Heating Boundary
Layer as Functions of y/δ
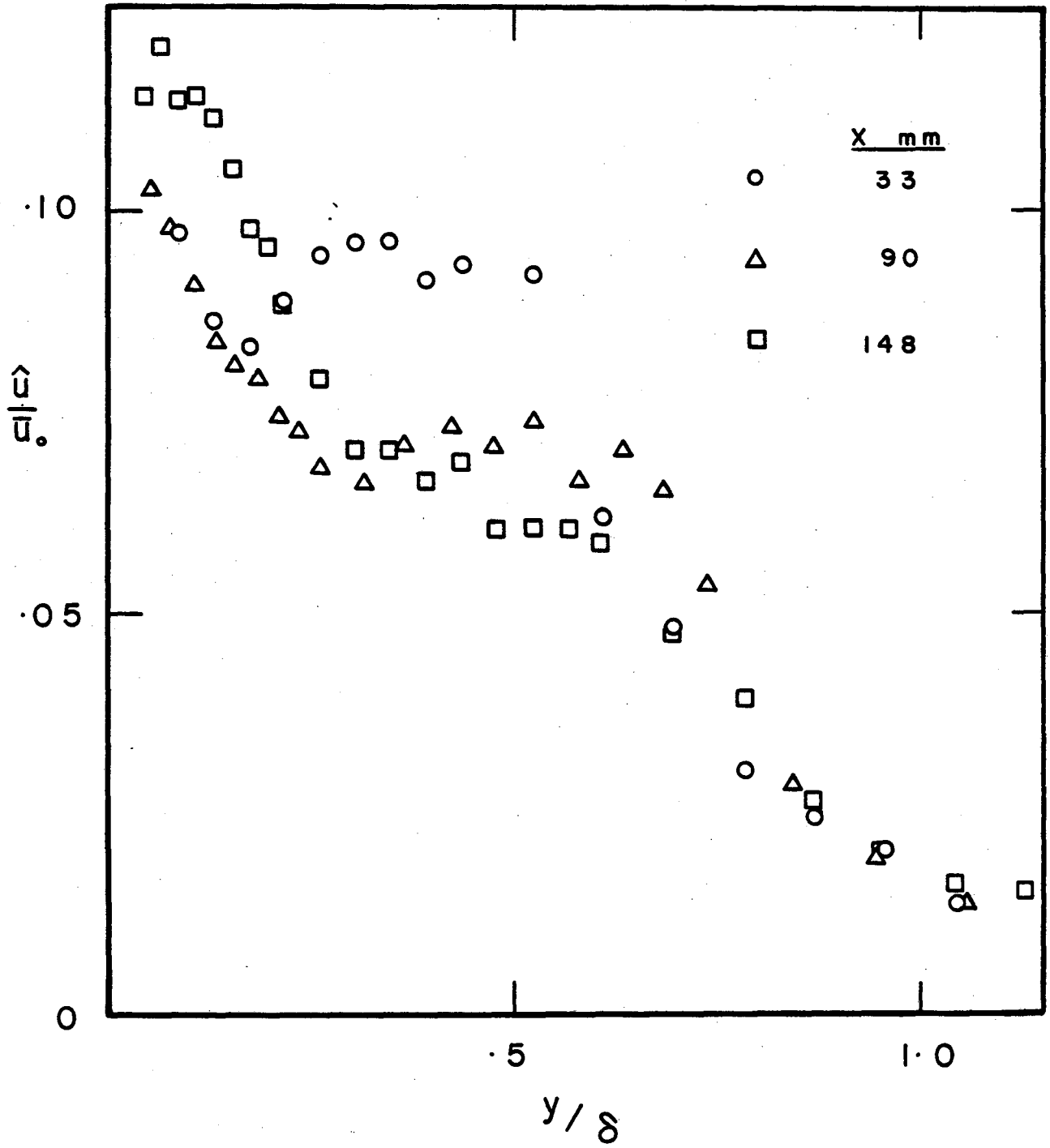
Fig. 39   Typical RMS Streamwise Velocity Profiles of the Reacting
Boundary Layer
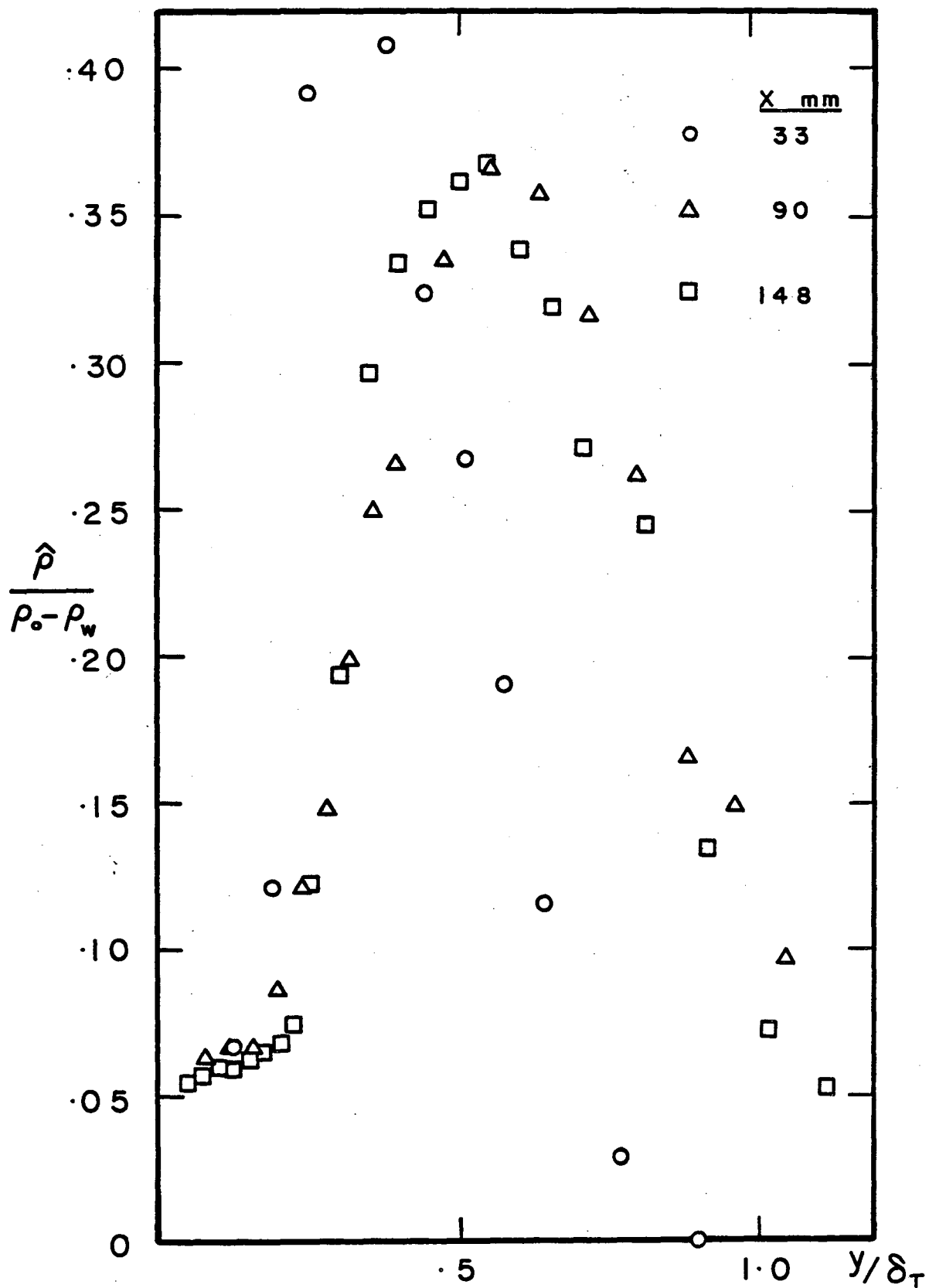
Fig. 40   Typical RMS Density Profiles of the Reacting
           Boundary Layer

$$-2\overline{\rho u'v'}/\rho_o \overline{u}_o^2$$

a. Isothermal
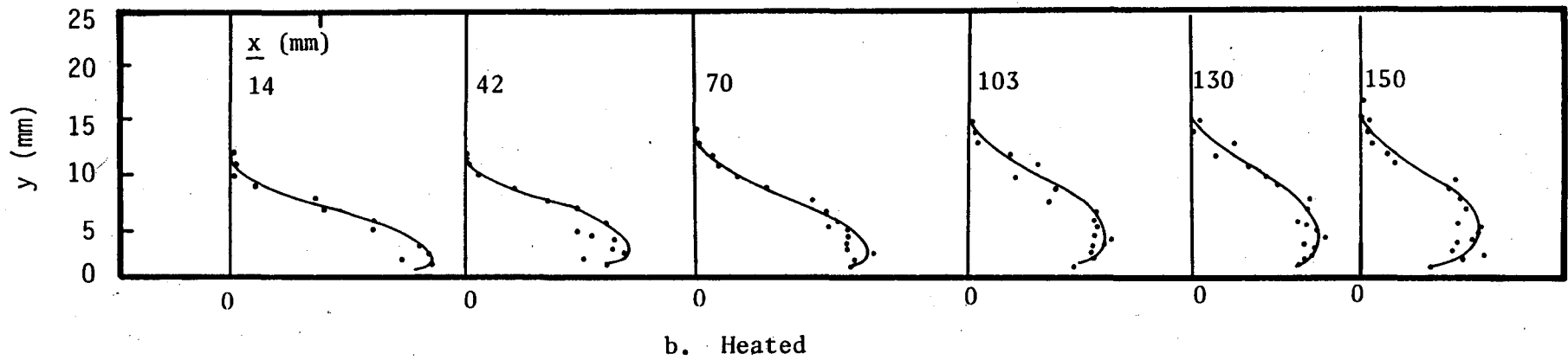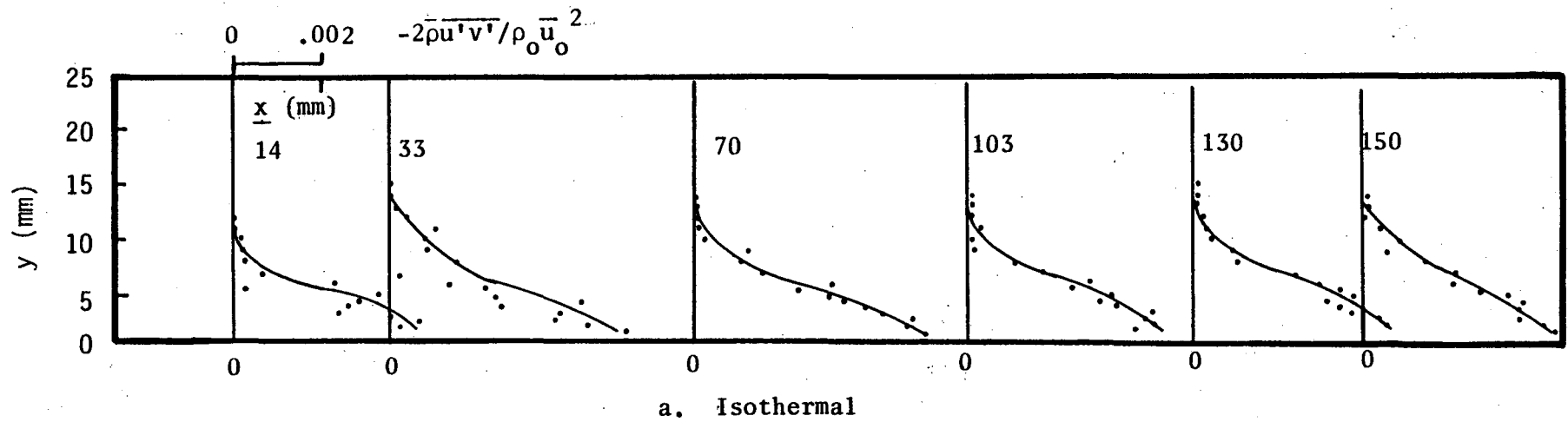
b. Heated

Fig. 41   The Reynolds Stress
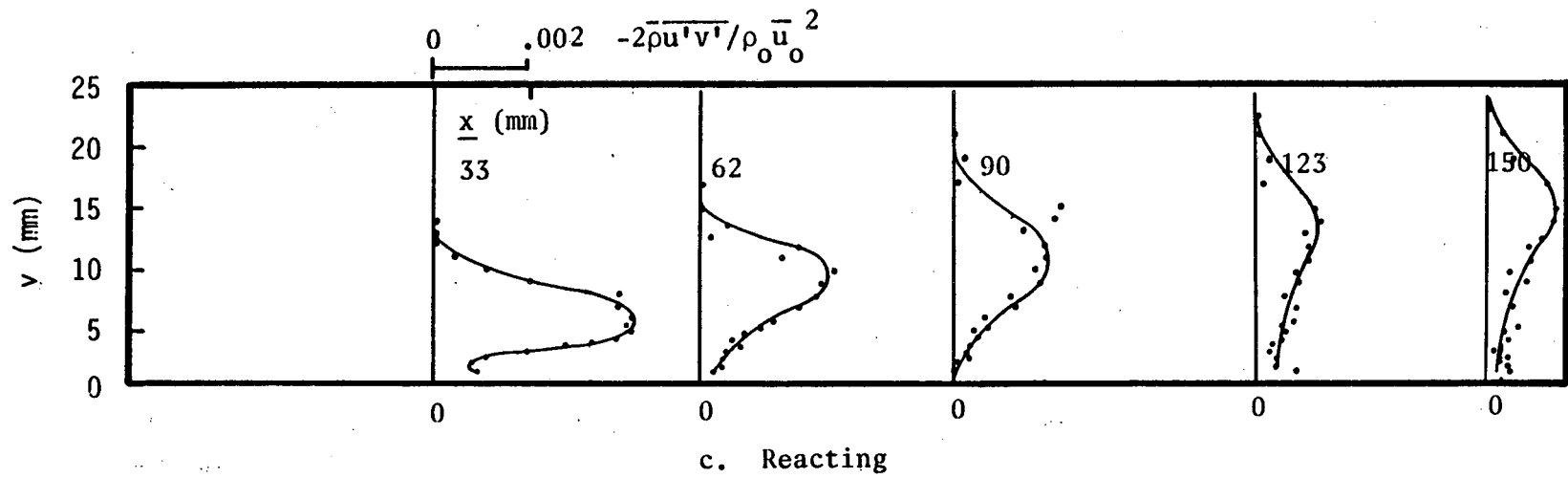
Fig. 41   The Reynolds Stress
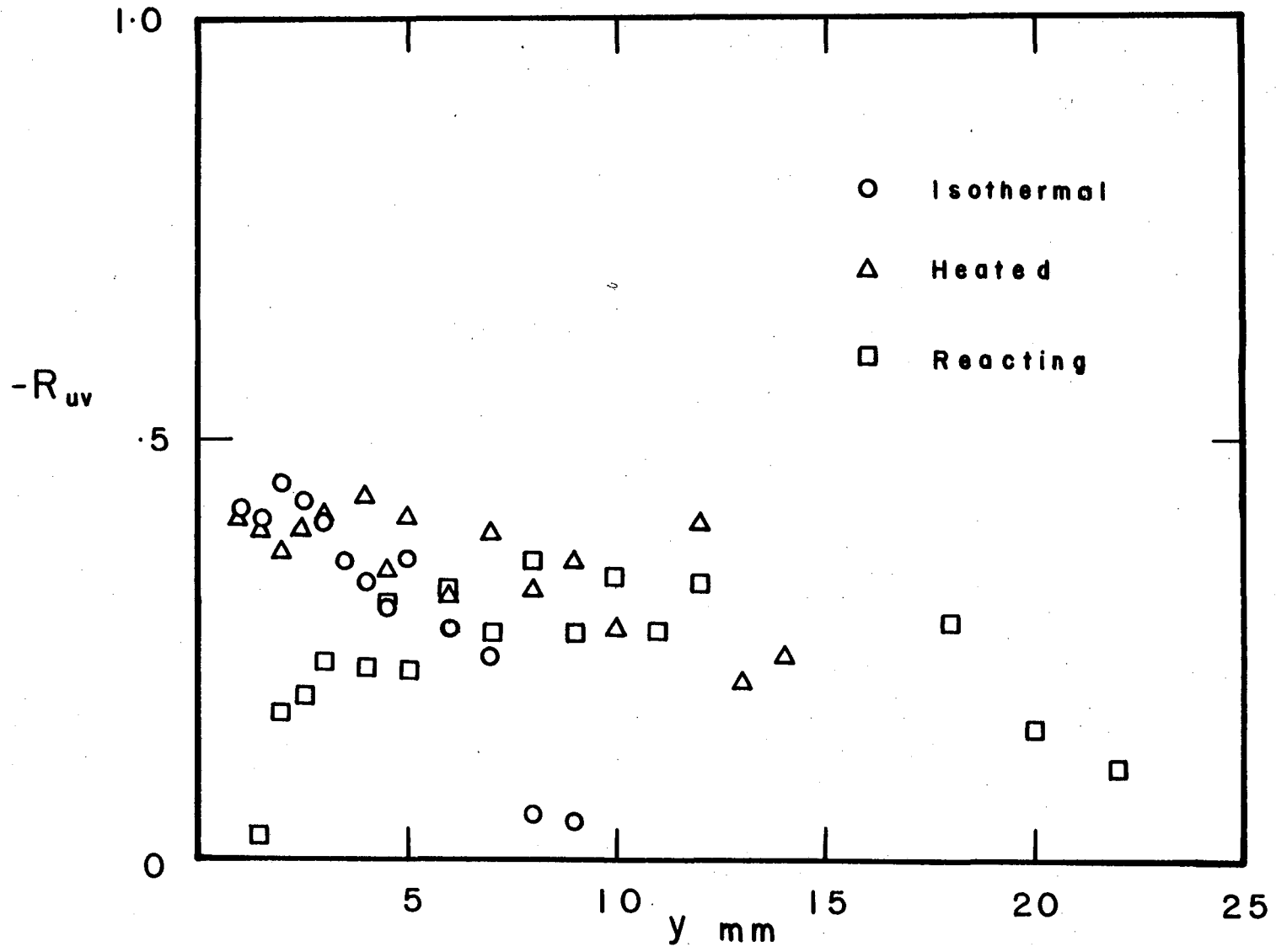
Fig. 42 The Correlation Coefficient Between u' and v' at x = 100 mm
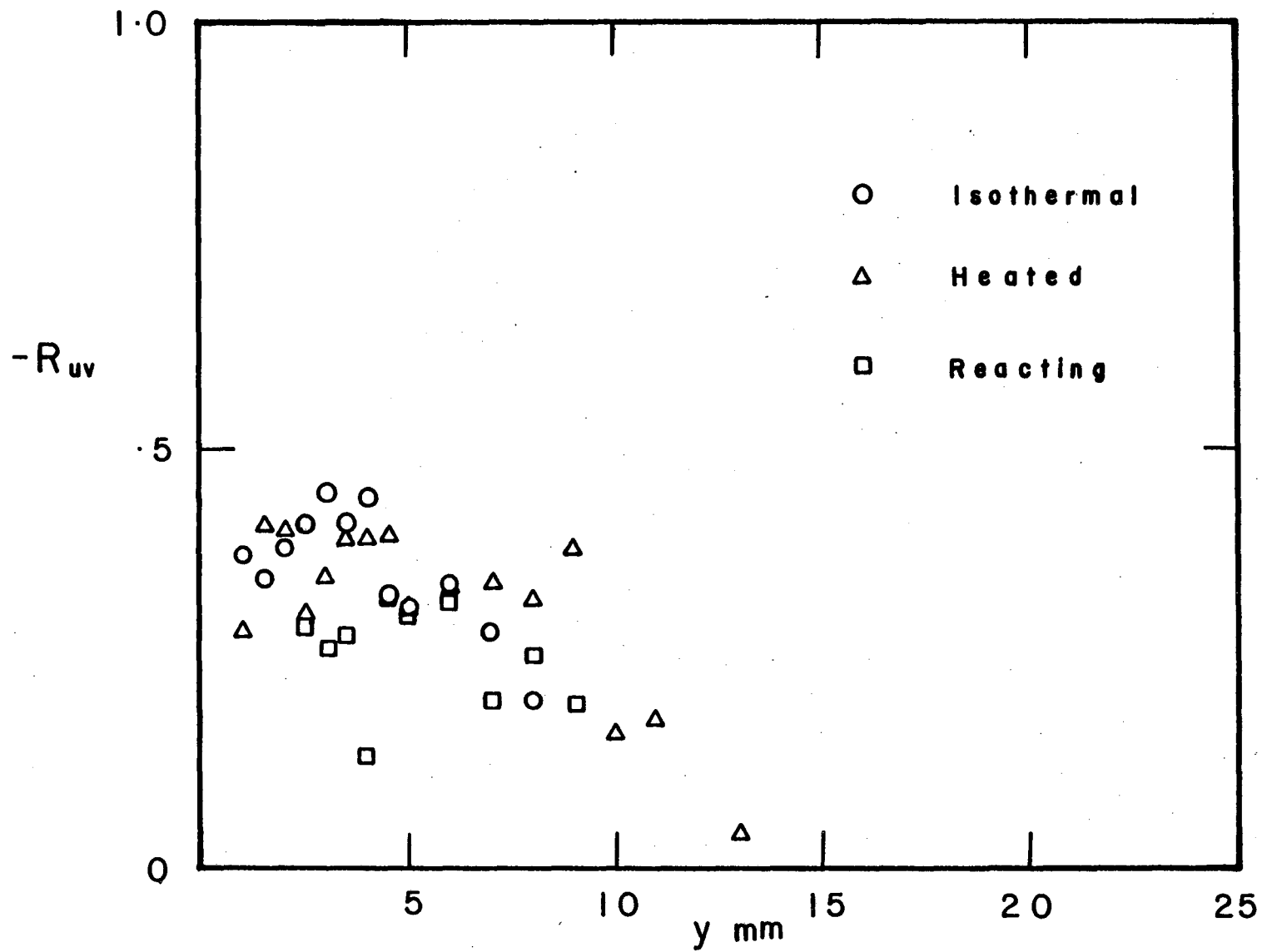
Fig. 43   The Correlation Coefficient Between u' and v' at x = 150 mm

The graph contains the following labels and annotations:

Vertical axis: $\dfrac{l_m}{\delta}$ with values $\cdot 10$, $\cdot 05$, 0

Horizontal axis: y/δ with values $\cdot 5$, $1 \cdot 0$

Escudier Formula: ──

$y/\delta < \gamma/\kappa$, $\quad l_m/\delta = \kappa y/\delta$

$y/\delta > \gamma/\kappa$, $\quad l_m/\delta = \gamma$

$\gamma \simeq .09$

$\kappa \simeq .41$

○   Isothermal

△   Heated

□   Reacting

──   Escudier Formula (From Launder and Spalding, 1972)
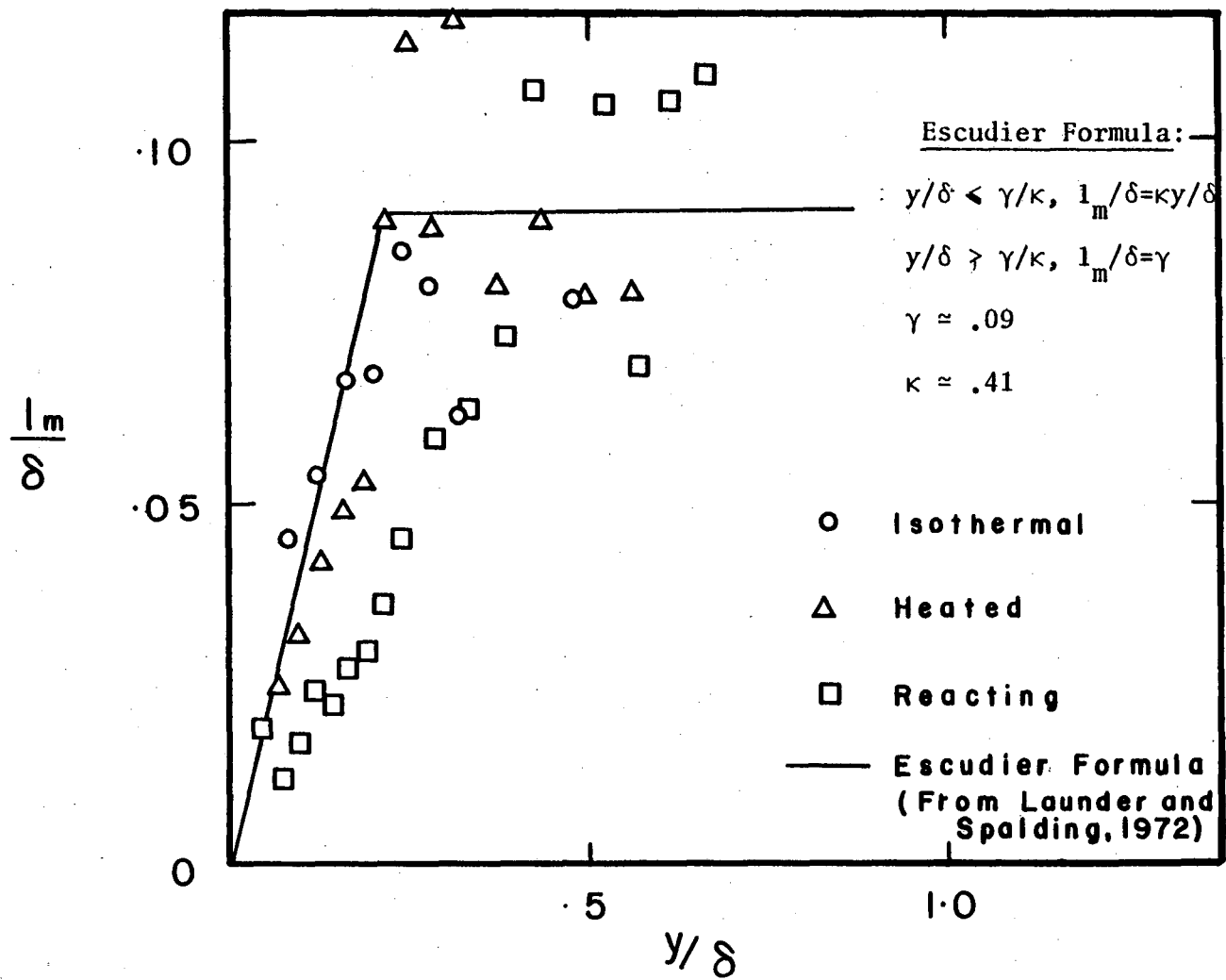
Fig. 44   The Mixing Length at x = 130 mm

Fig. 45   Turbulent Kinetic Energy Profiles

$0 \qquad .01 \quad \bar{\rho}\bar{k}_1/\bar{\rho}_o\bar{u}_o^{\,2}$

$\dfrac{x}{33}$ (mm) 62 90 123 148

y (mm)
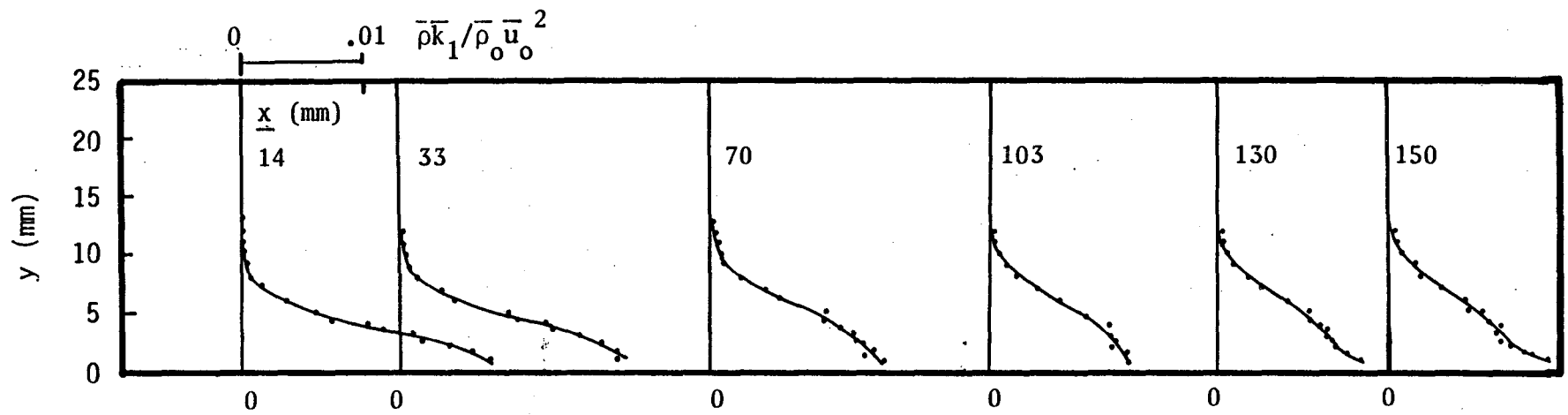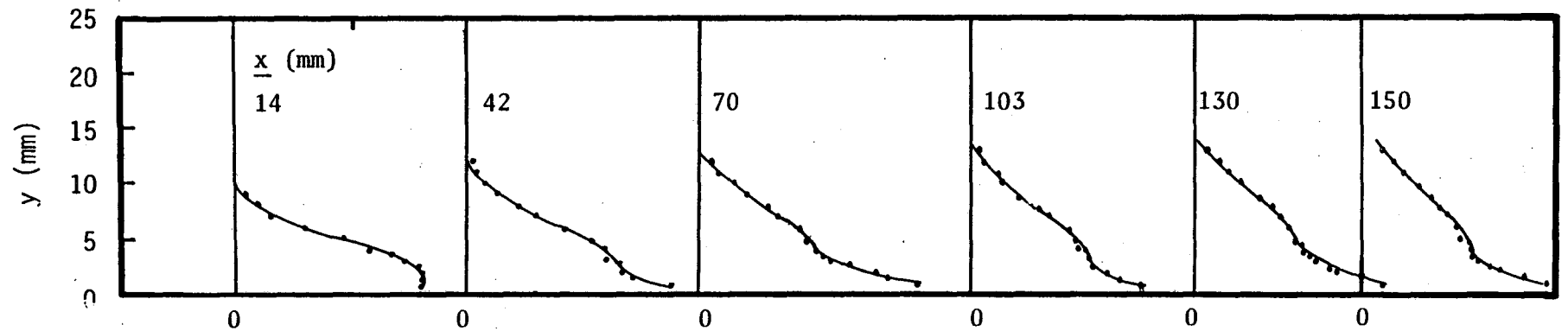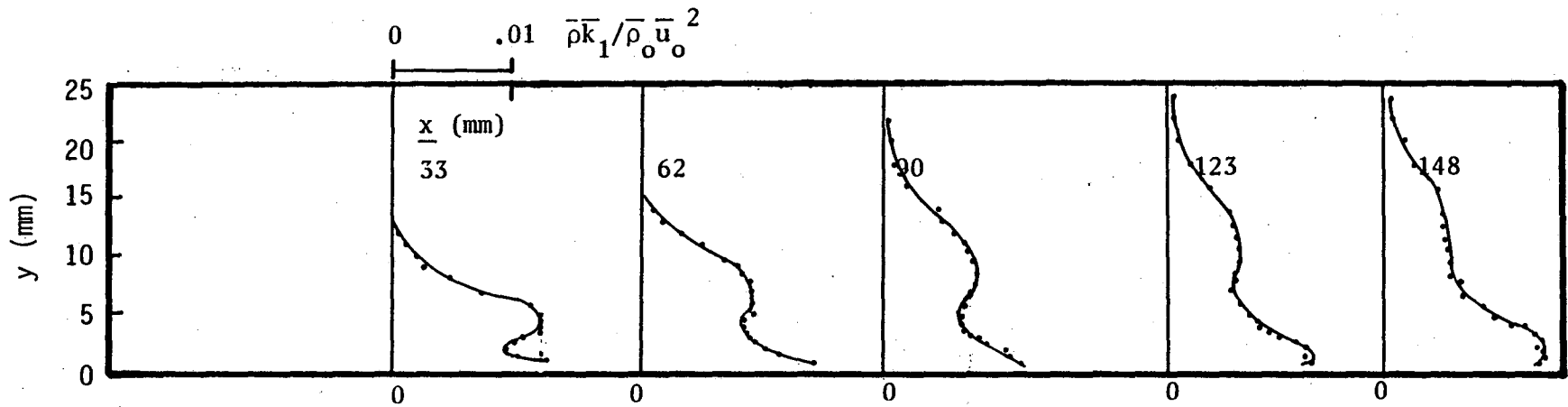
c. Reacting

Fig. 45   Turbulent Kinetic Energy Profiles

$0 \qquad .0005 \quad -\overline{u'k}_1/\,\bar{u}_o^{\,3}$

$\dfrac{x}{14}$ (mm) 33 70 103 130 150

y (mm)
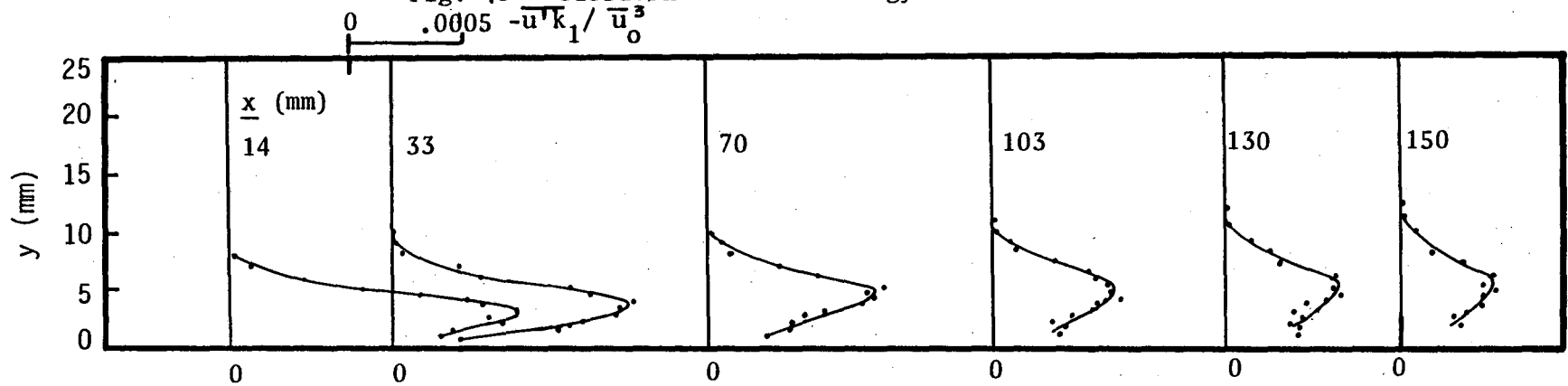
a. Isothermal

Fig. 46 $\overline{u'k}_1$ Profiles

$-\overline{u'k_1}/\overline{u}_o^3$
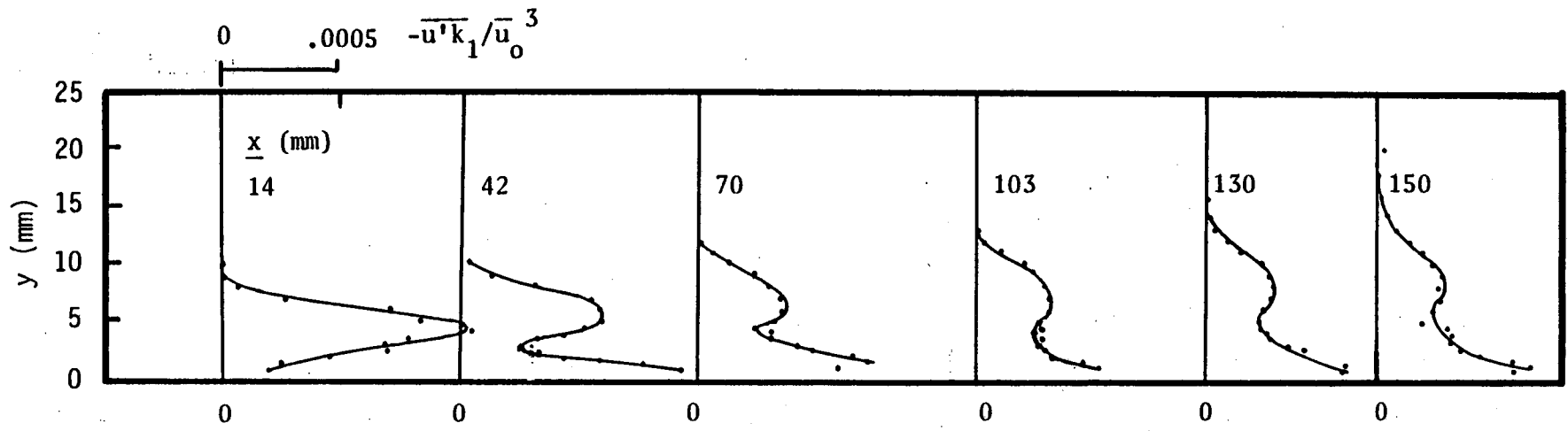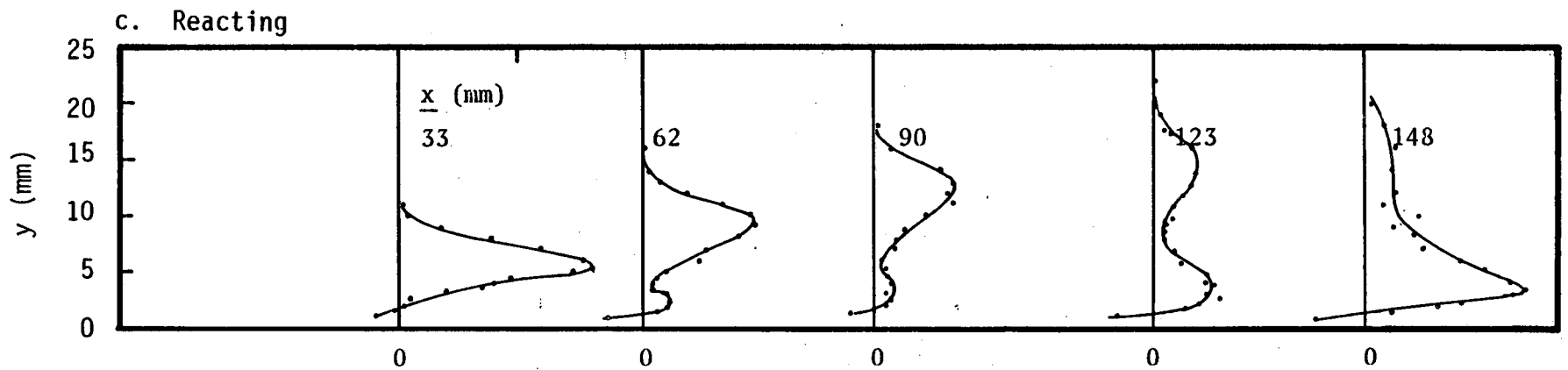
b. Heated

c. Reacting

c. Reacting

Fig. 46 $\overline{u'k_1}$ Profiles
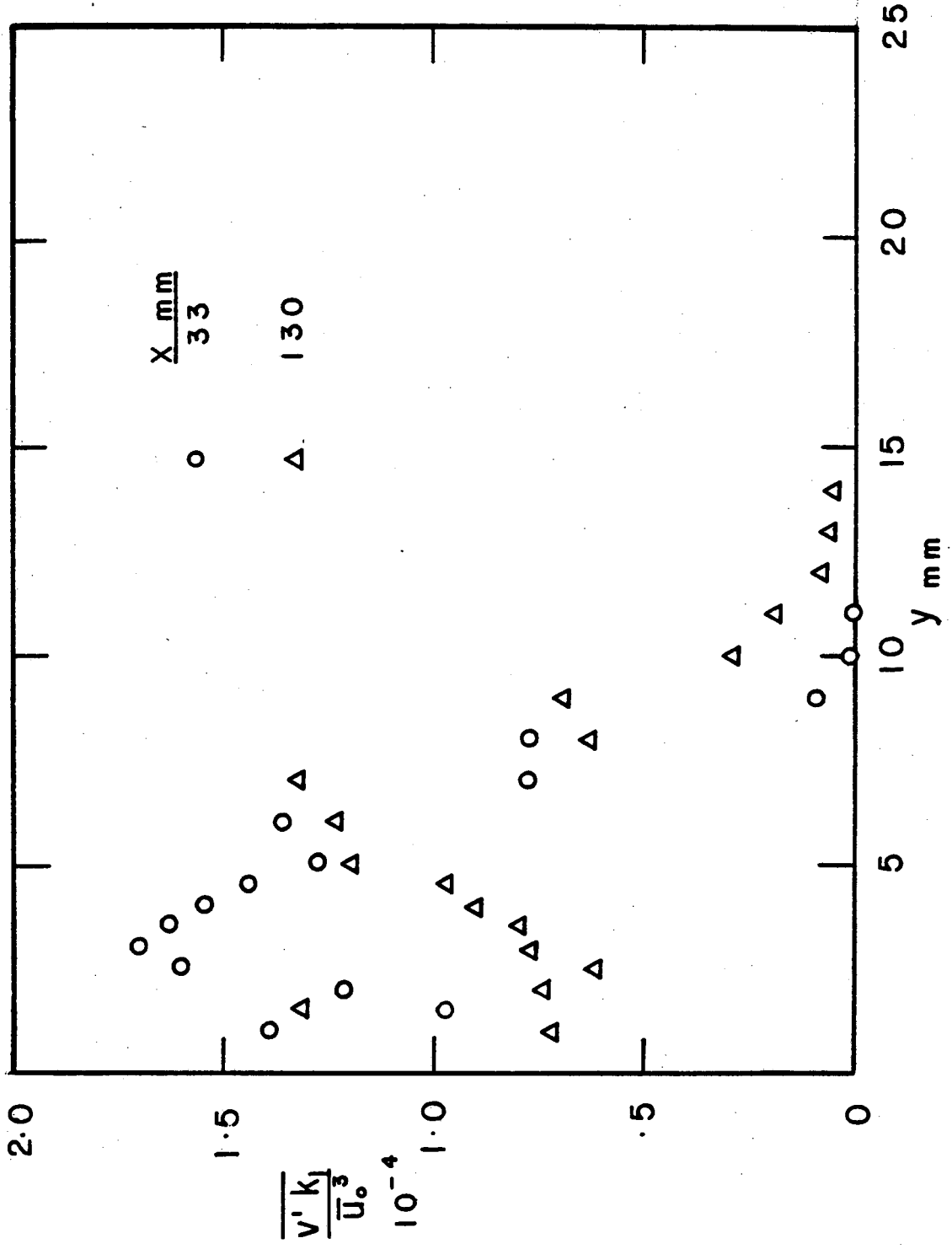
Fig. 47a $\overline{v' k_1}$ Profiles of the Isothermal Boundary Layer
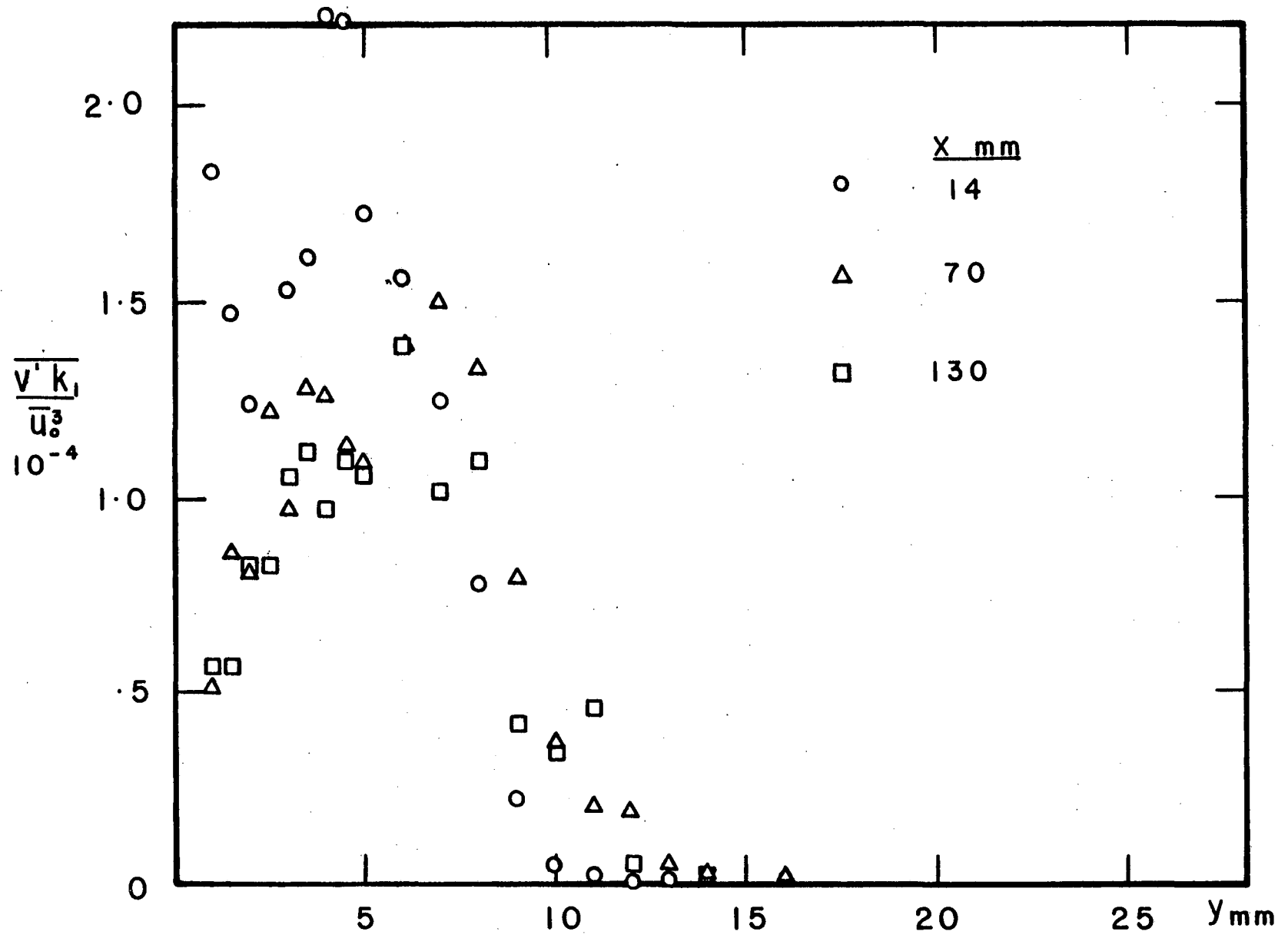
Fig. 47b $\overline{v'k_1}$ Profiles of the Heated Boundary Layer
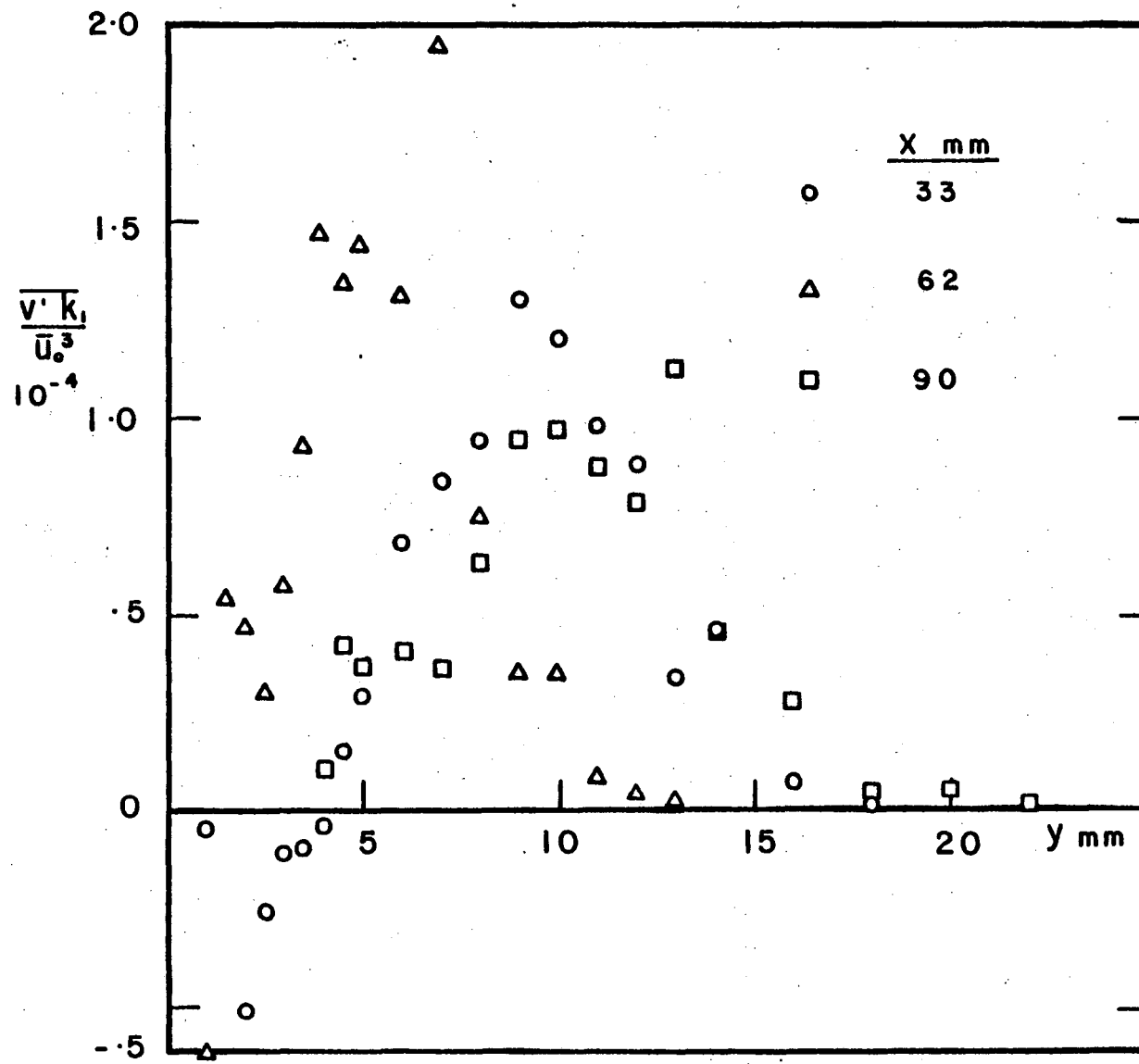
Fig. 47c $\overline{v'k_1}$ Profiles of the Reacting Boundary Layer
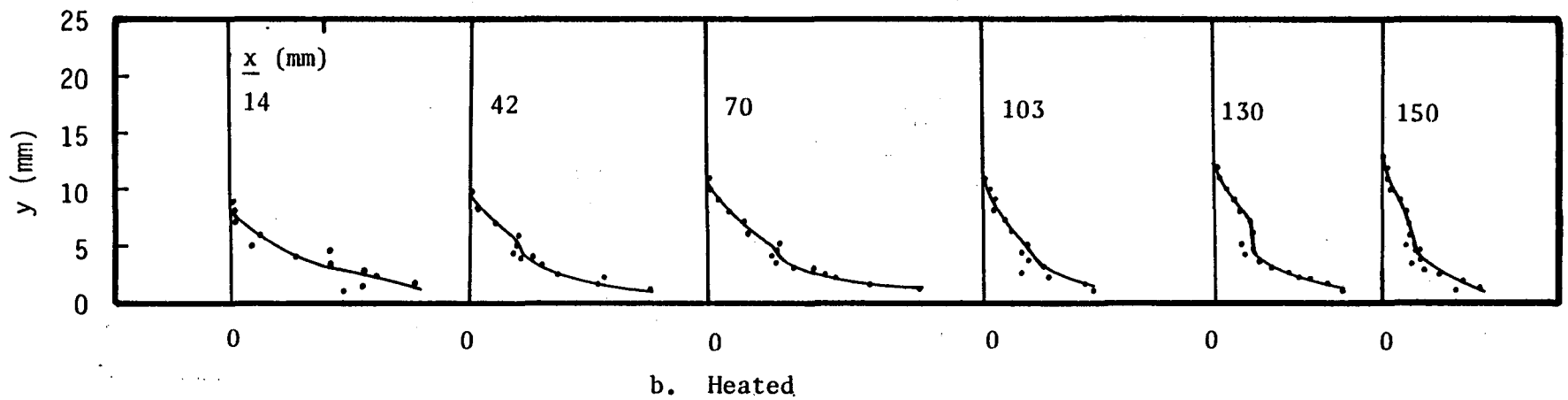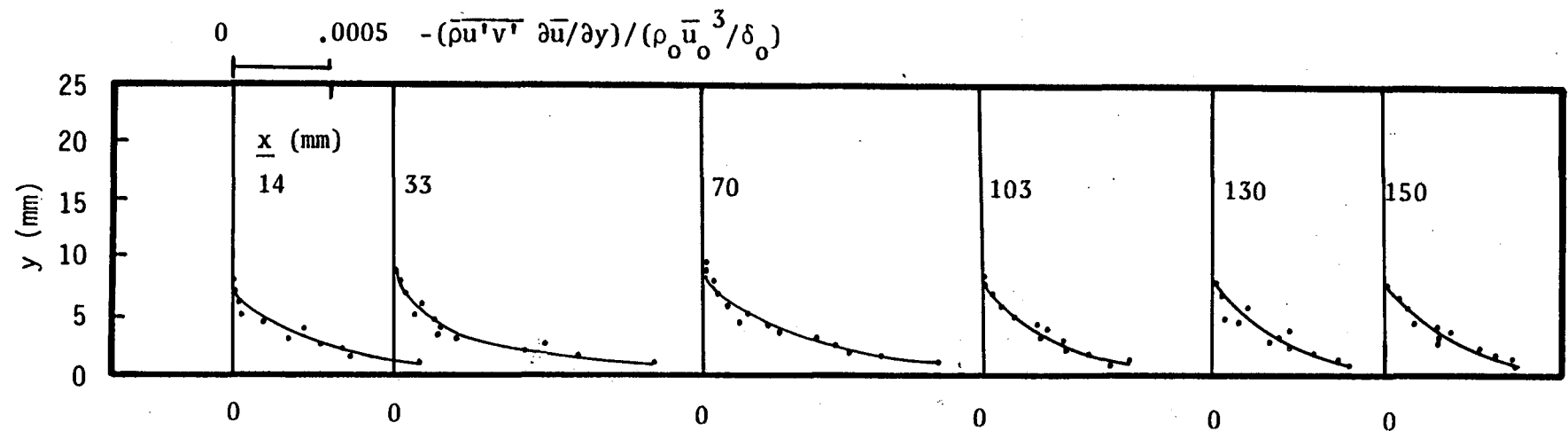
Fig. 48   Turbulent Kinetic Energy Production by Turbulent Stress

Fig. 48   Turbulent Kinetic Energy Production by Turbulent Stress

2·0

$- \dfrac{\overline{u'v'k_1}}{u_o^4}$

10^{-4}

1·0

0

X mm

○ 33

△ 103

□ 160

·5

y/δ

1·5
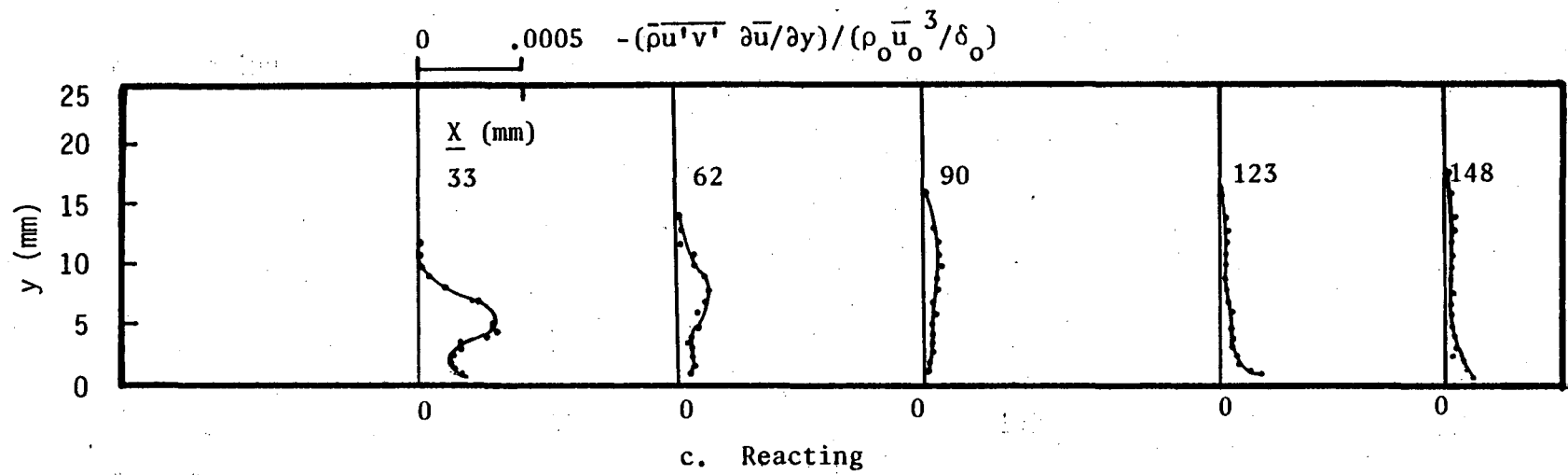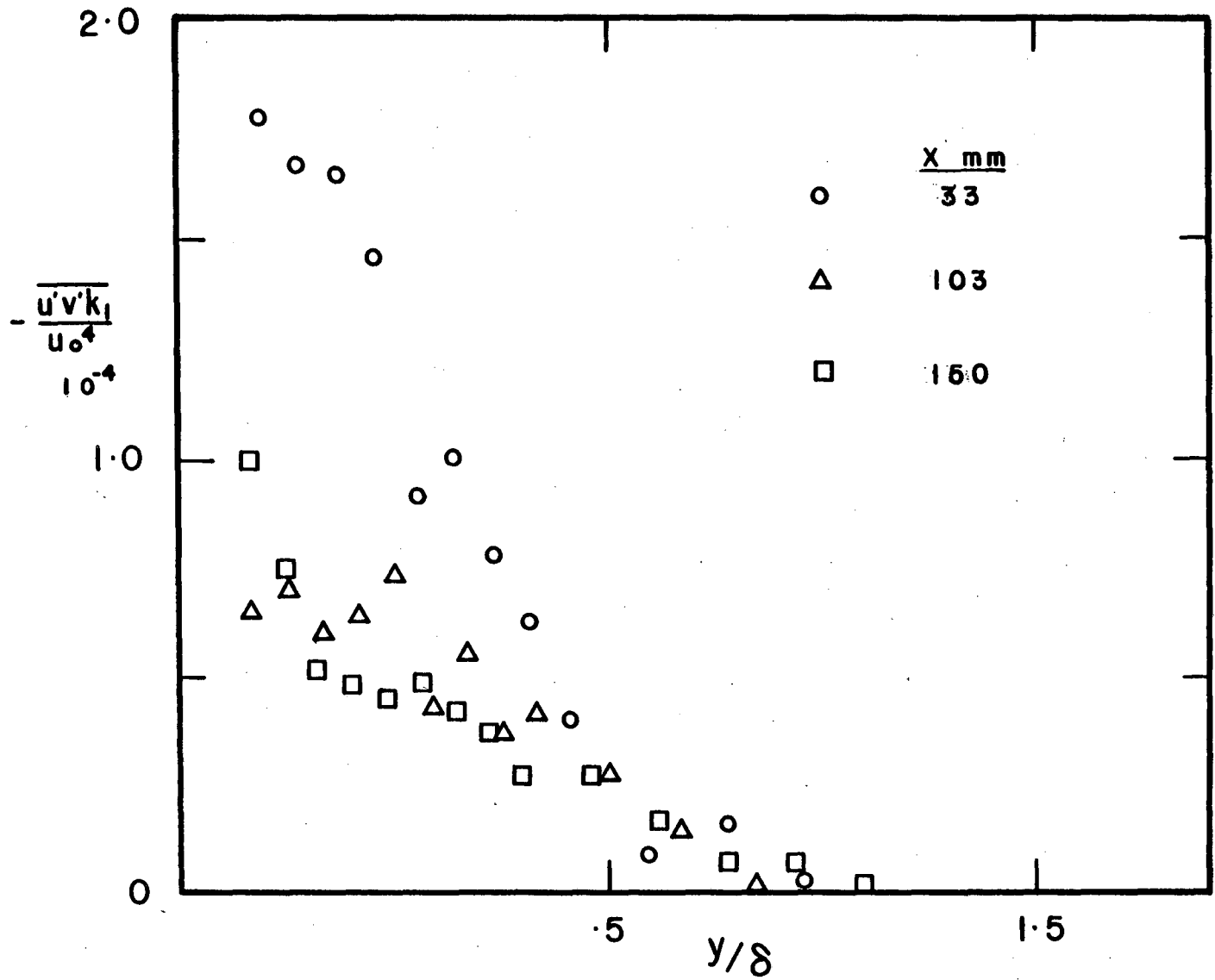
Fig. 49a $\overline{u'v'k_1}$ Profiles of the Isothermal Boundary Layer
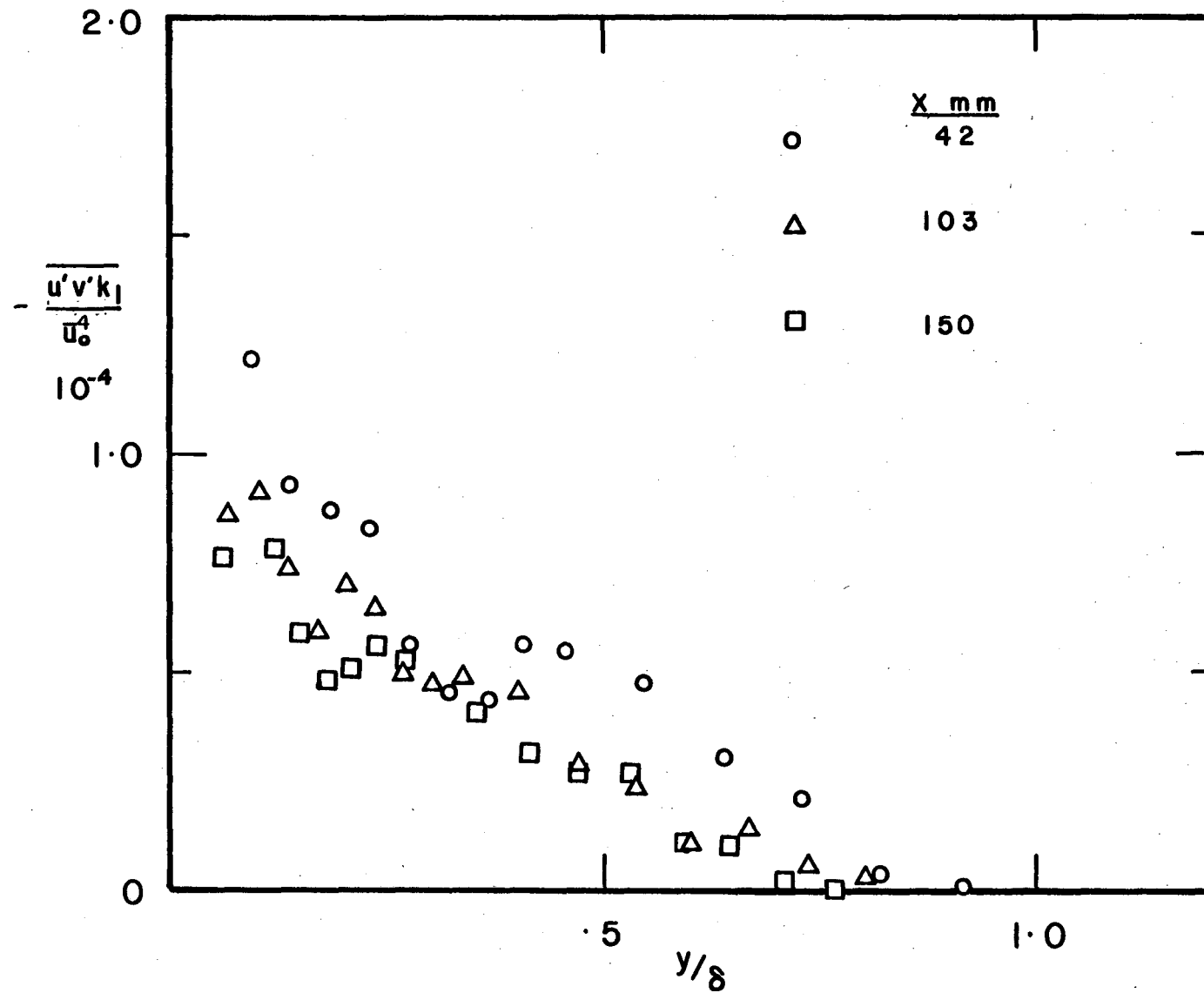
Fig. 49b $\overline{u'v'k_1}$ Profiles of the Heated Boundary Layer
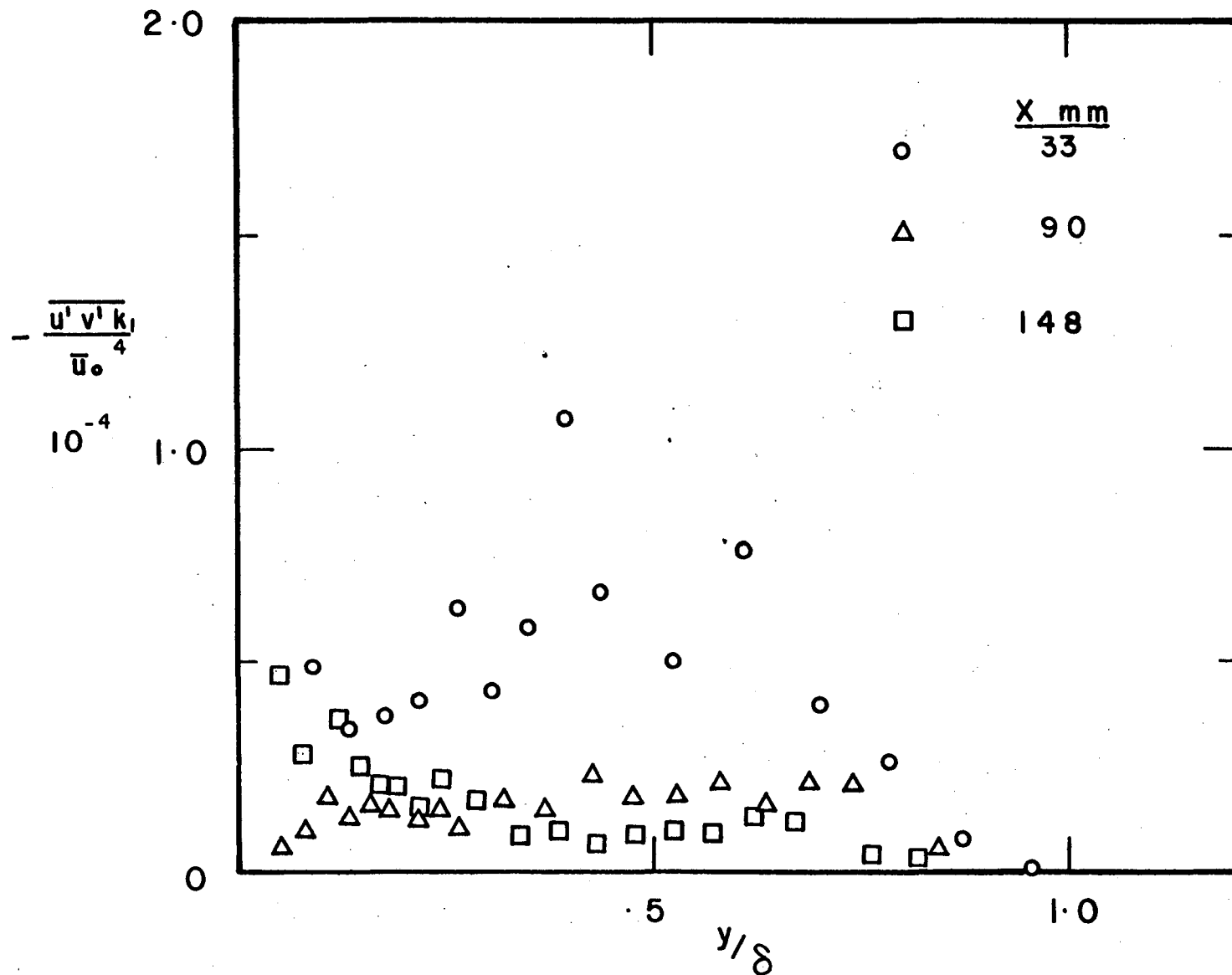
Fig. 49c $\overline{u'v'k}_1$ Profiles of the Reacting Boundary Layer
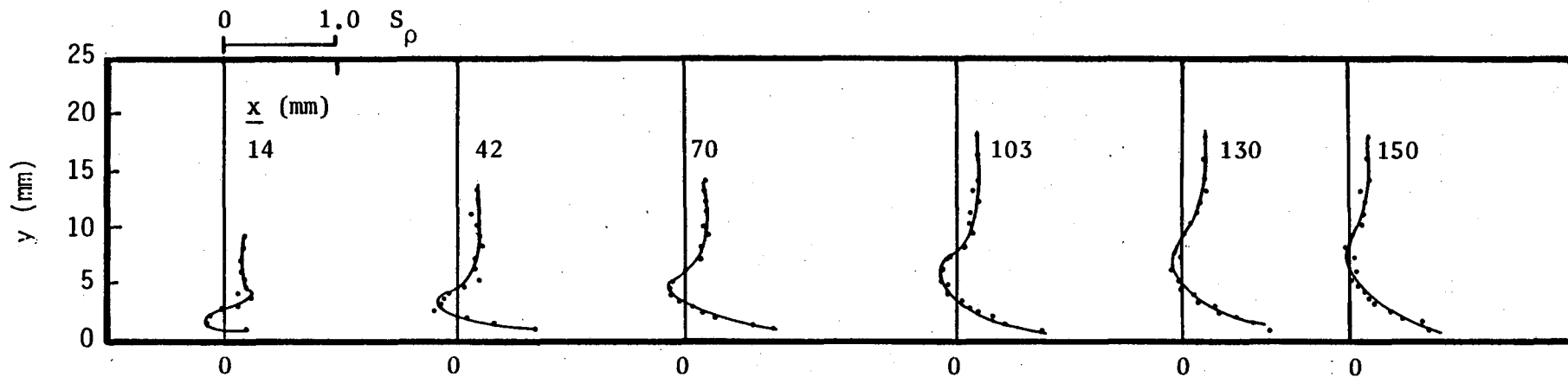
Fig. 50   Skewness Factors of the Density Measurements

0   5 $(F_\rho - 3)$

x (mm)
14   42   70   103   130   150

0   0   0   0   0   0

a. Heated

x (mm)
33   62   90   123   150

0   0   0   0   0
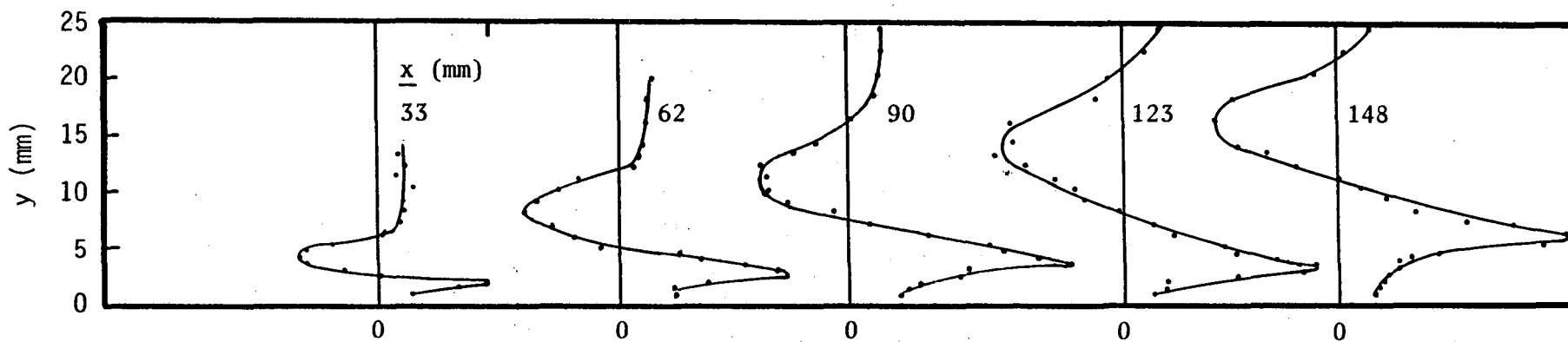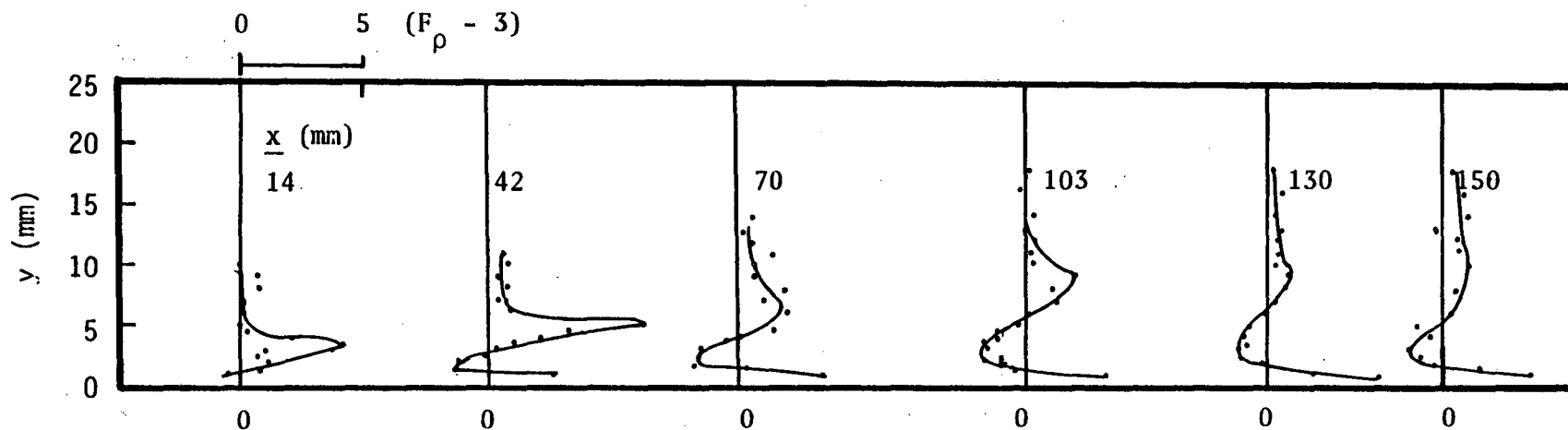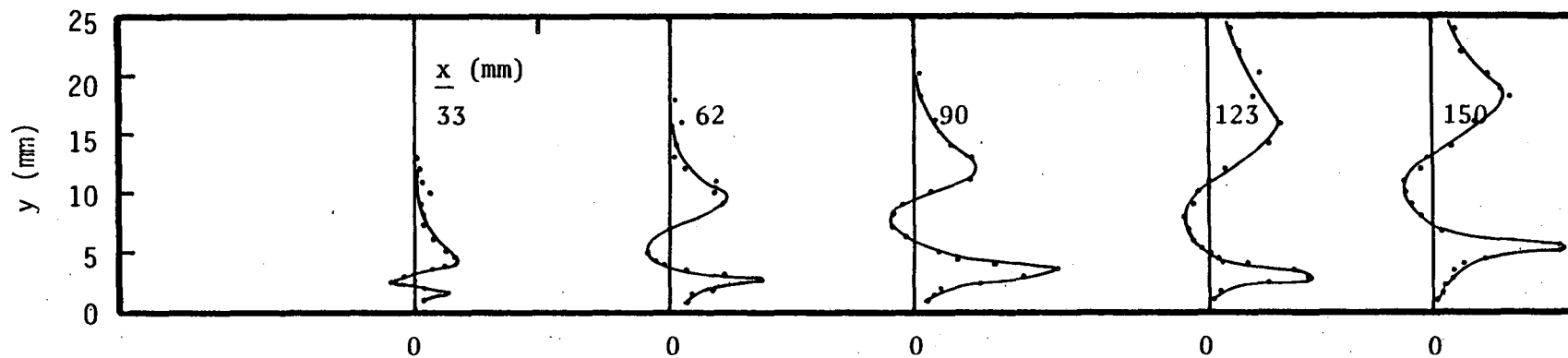
b. Reacting

Fig. 51   Flatness Factors of the density Measurements
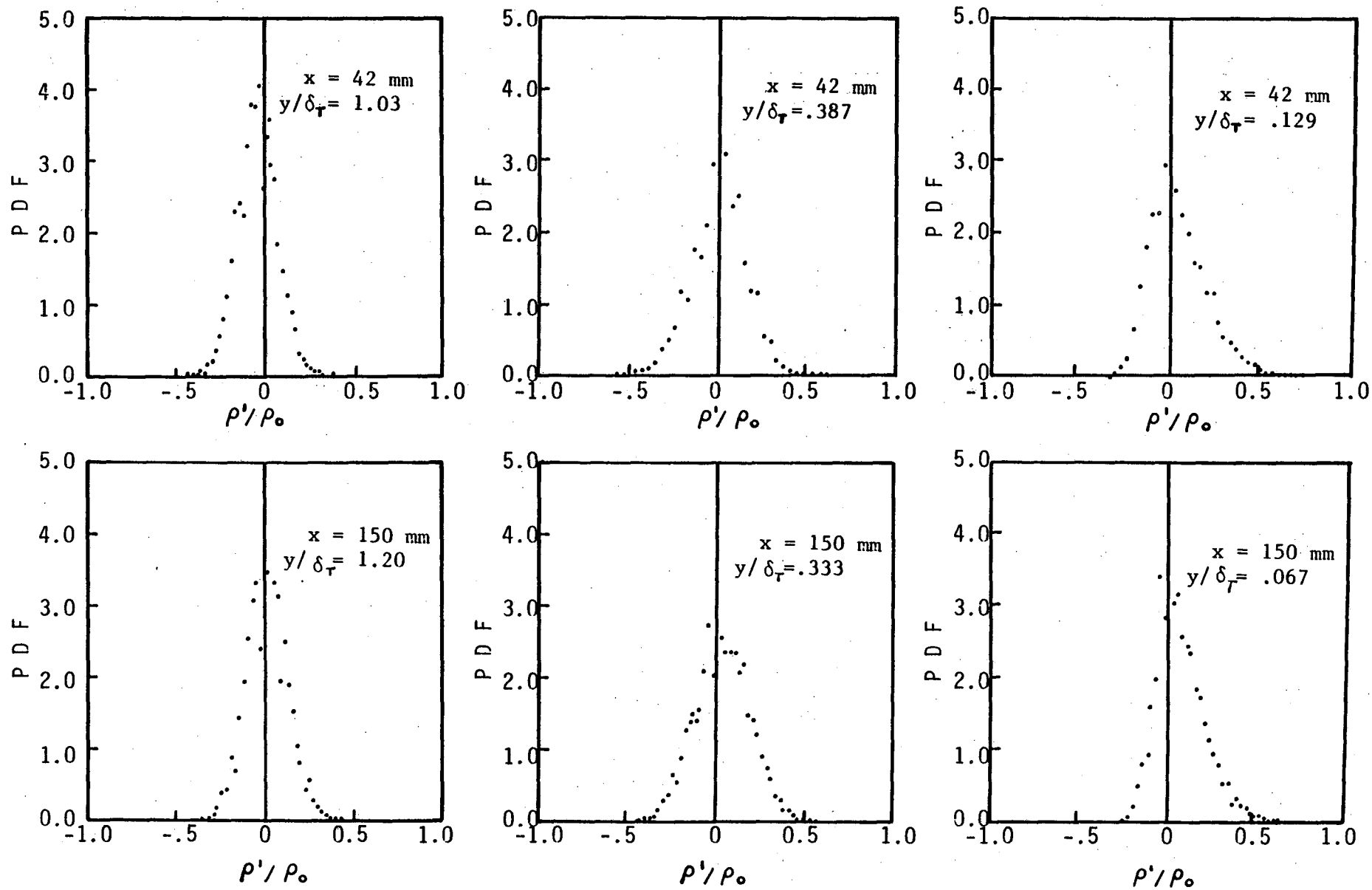
Fig. 52   Density Probability Density Functions (PDF's) of the Heated Boundary Layer
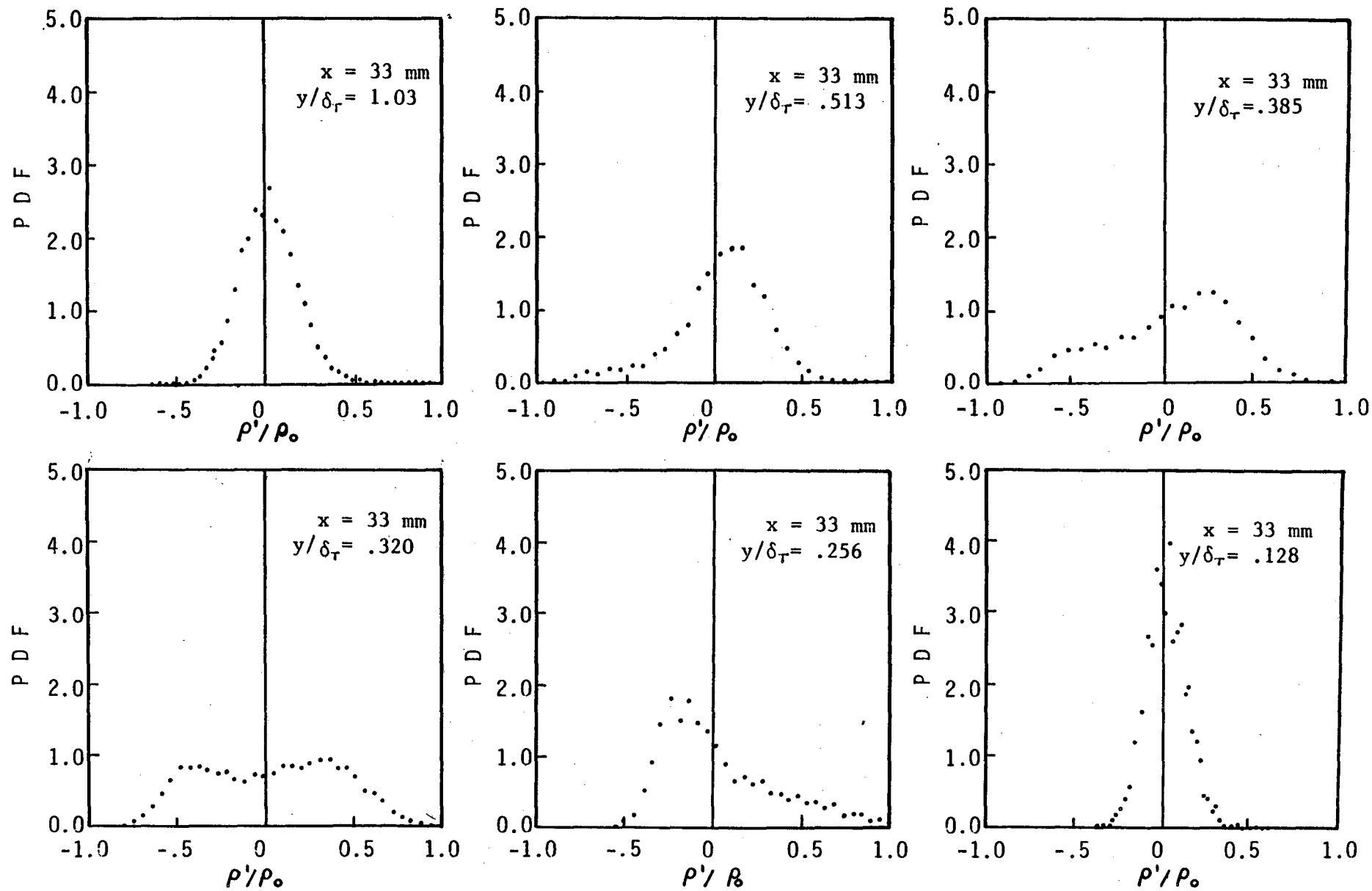
Fig. 53   Density PDF's of the Reacting Boundary Layer at x = 33 mm
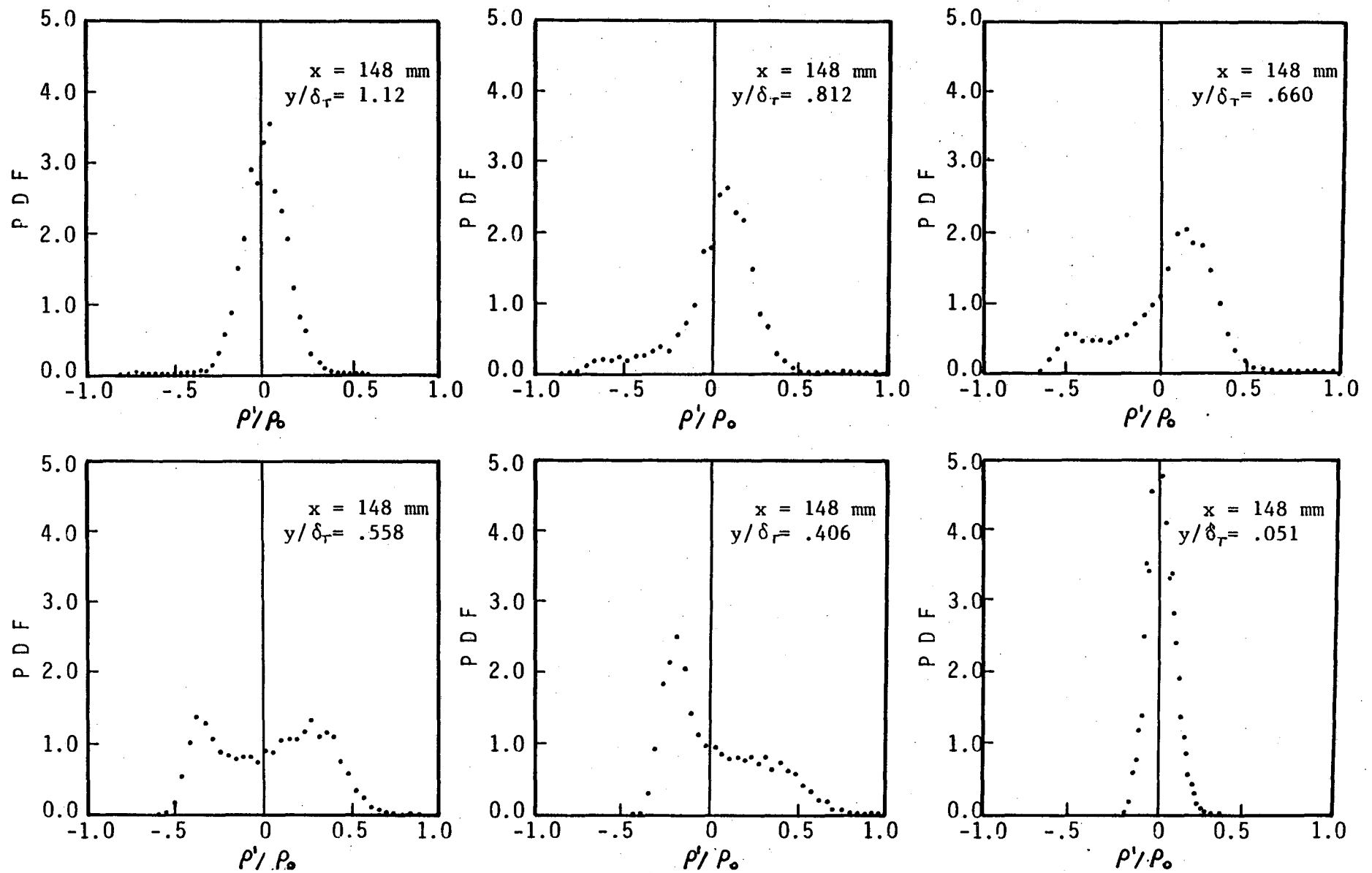
Fig. 54   Density PDF's of the Reacting Boundary Layer at x = 148 mm
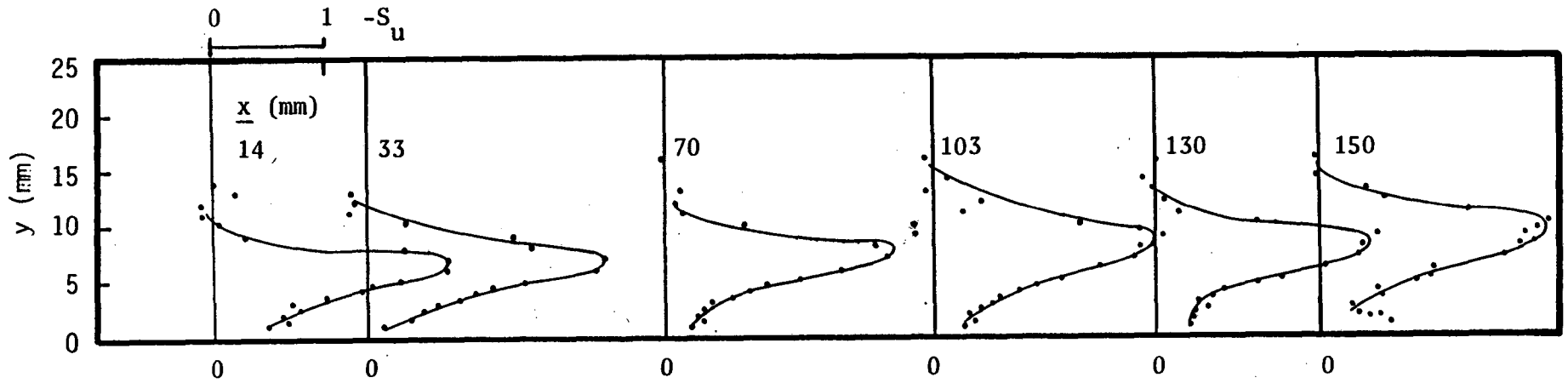
a. Isothermal
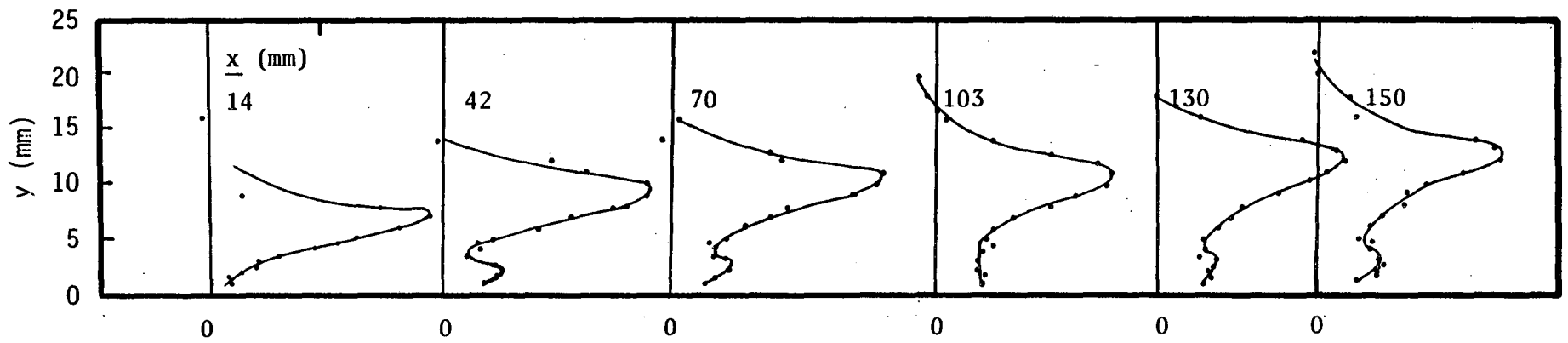
b. Heated

Fig. 55   Skewness Factors of the Streamwise Velocity

c. Reacting

Fig. 55   Skewness Factors of the Streamwise Velocity
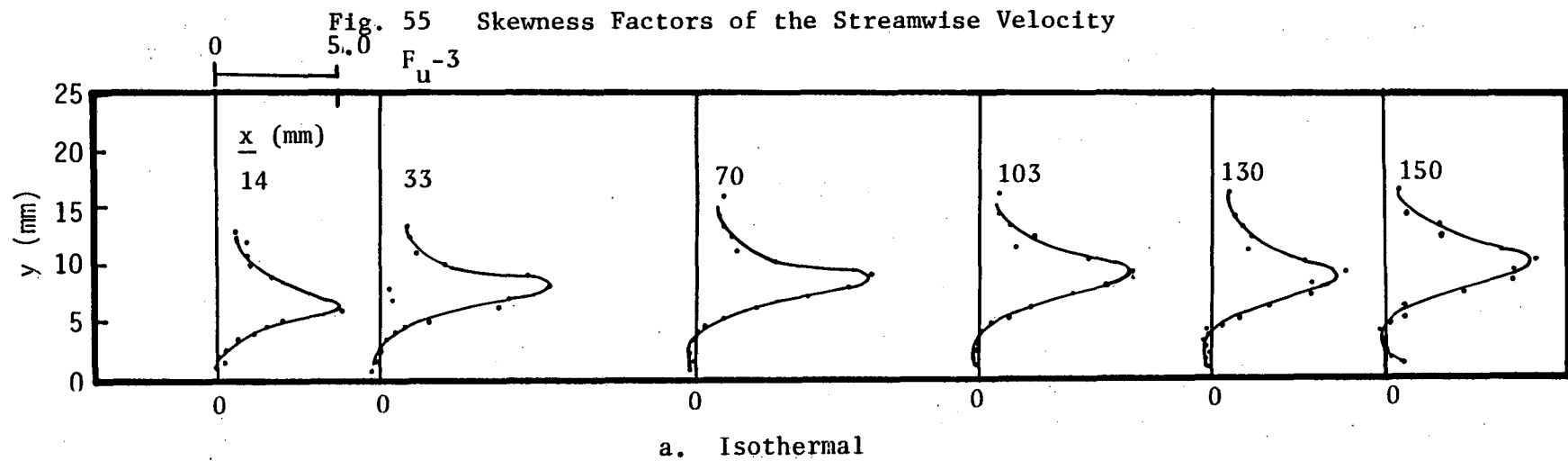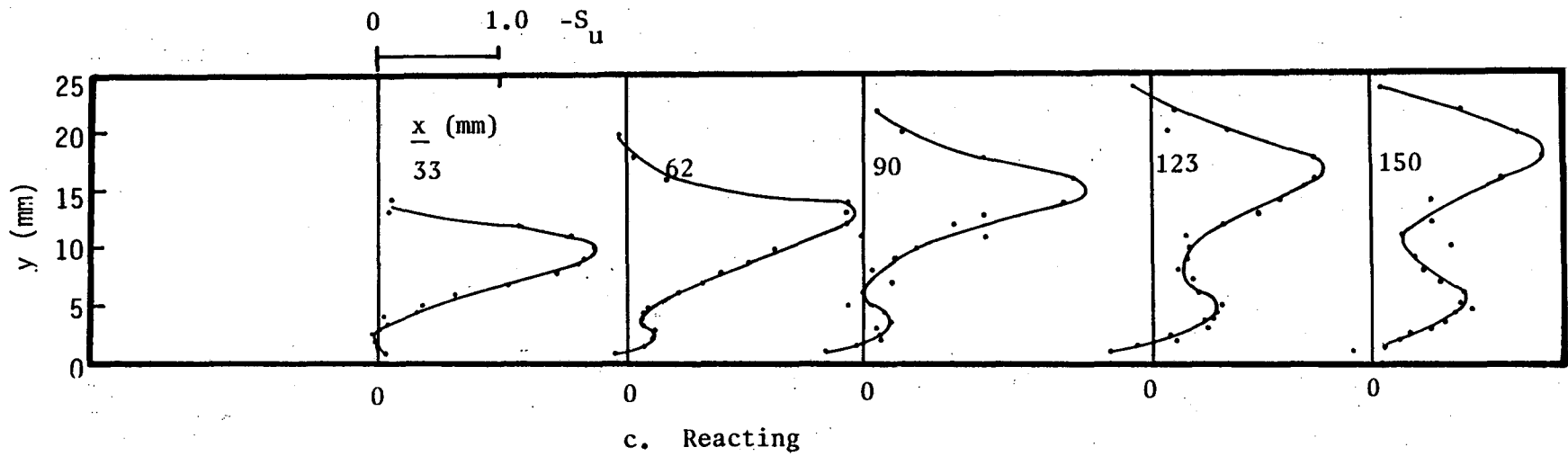
a. Isothermal

Fig. 56   Flatness Factors of the Streamwise Velocity
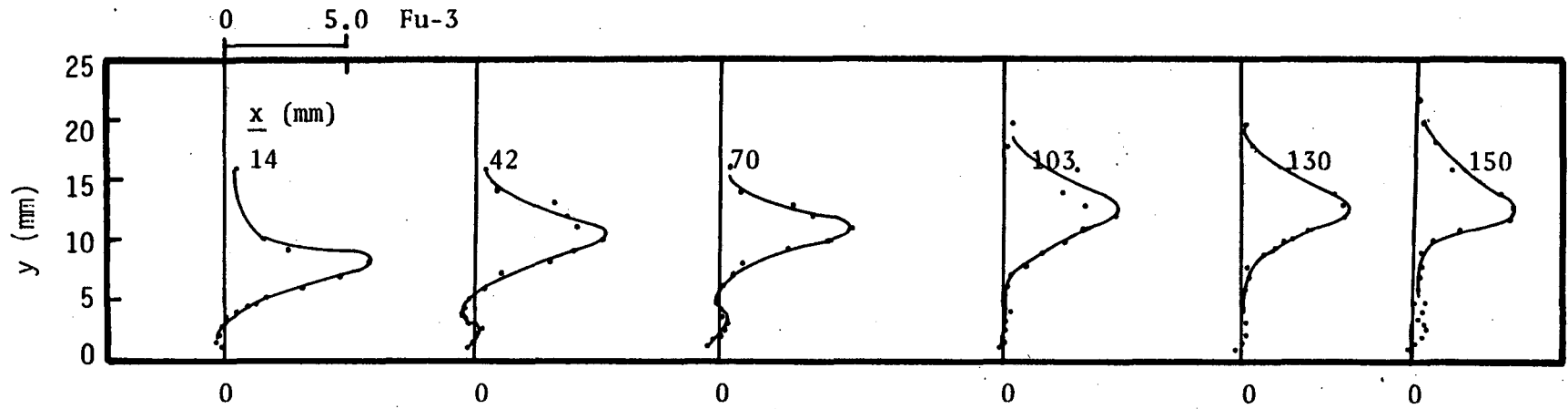
b. Heated
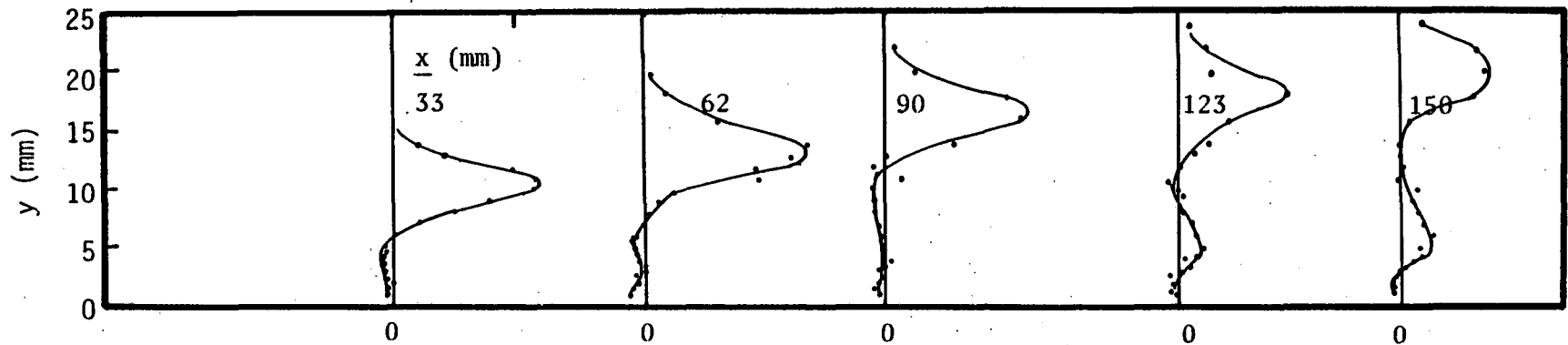
c. Reacting

Fig. 56   Flatness Factors of the Streamwise Velocity
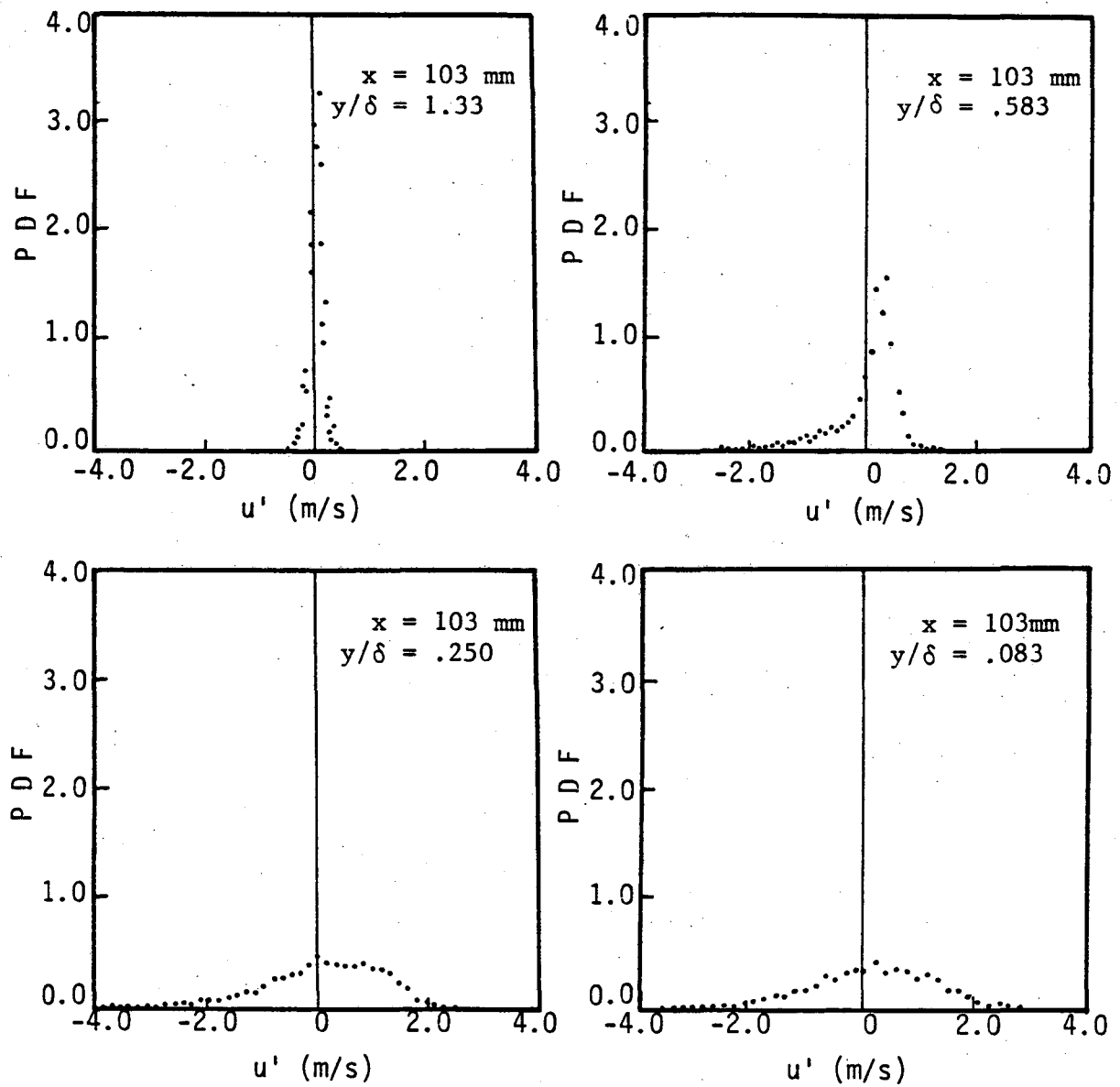
Fig. 57   Velocity PDF's of the Isothermal Boundary Layer at
x = 103 mm
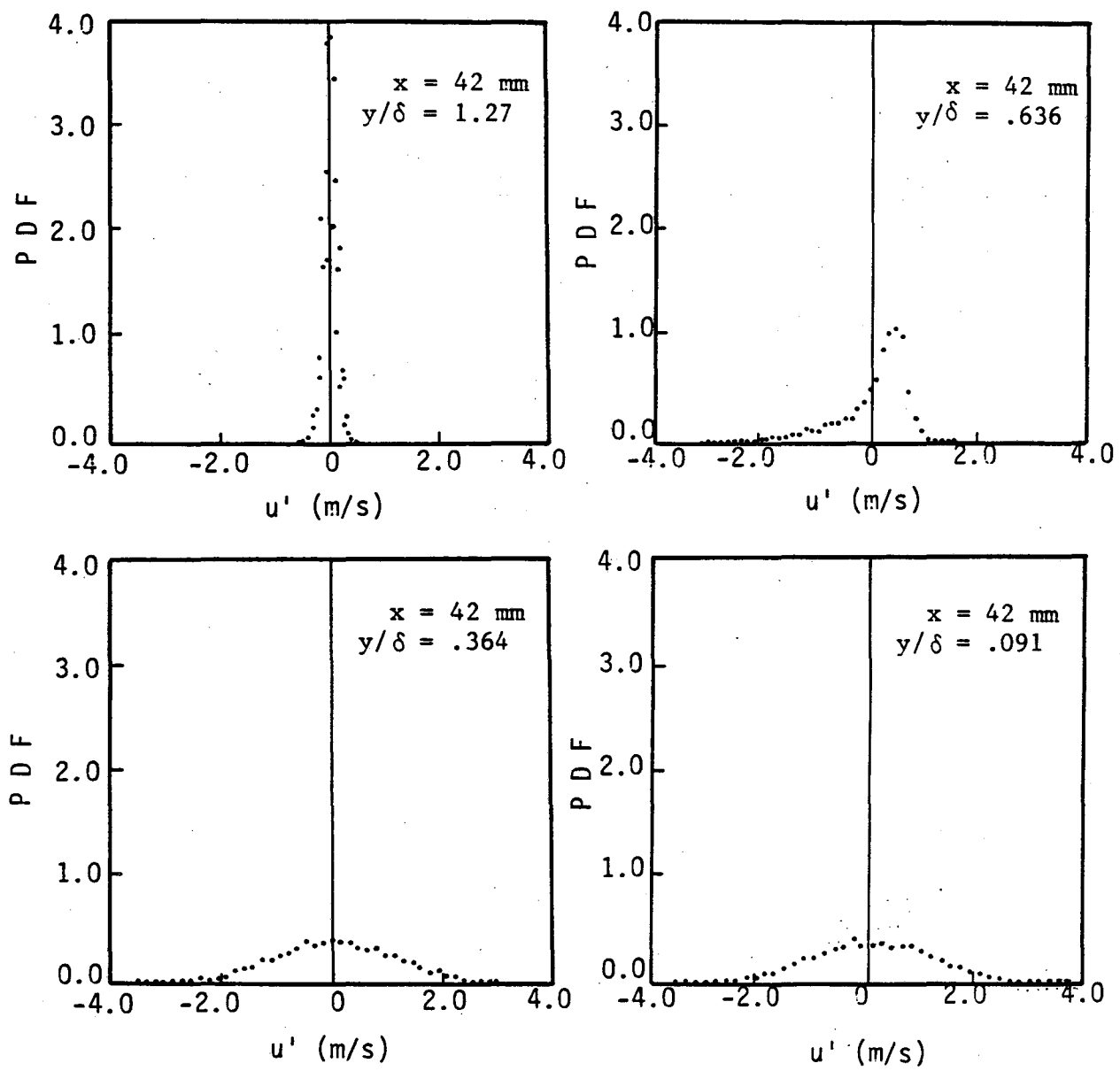
Fig. 58   Velocity PDF's of the Heated Boundary Layer at x = 42 mm
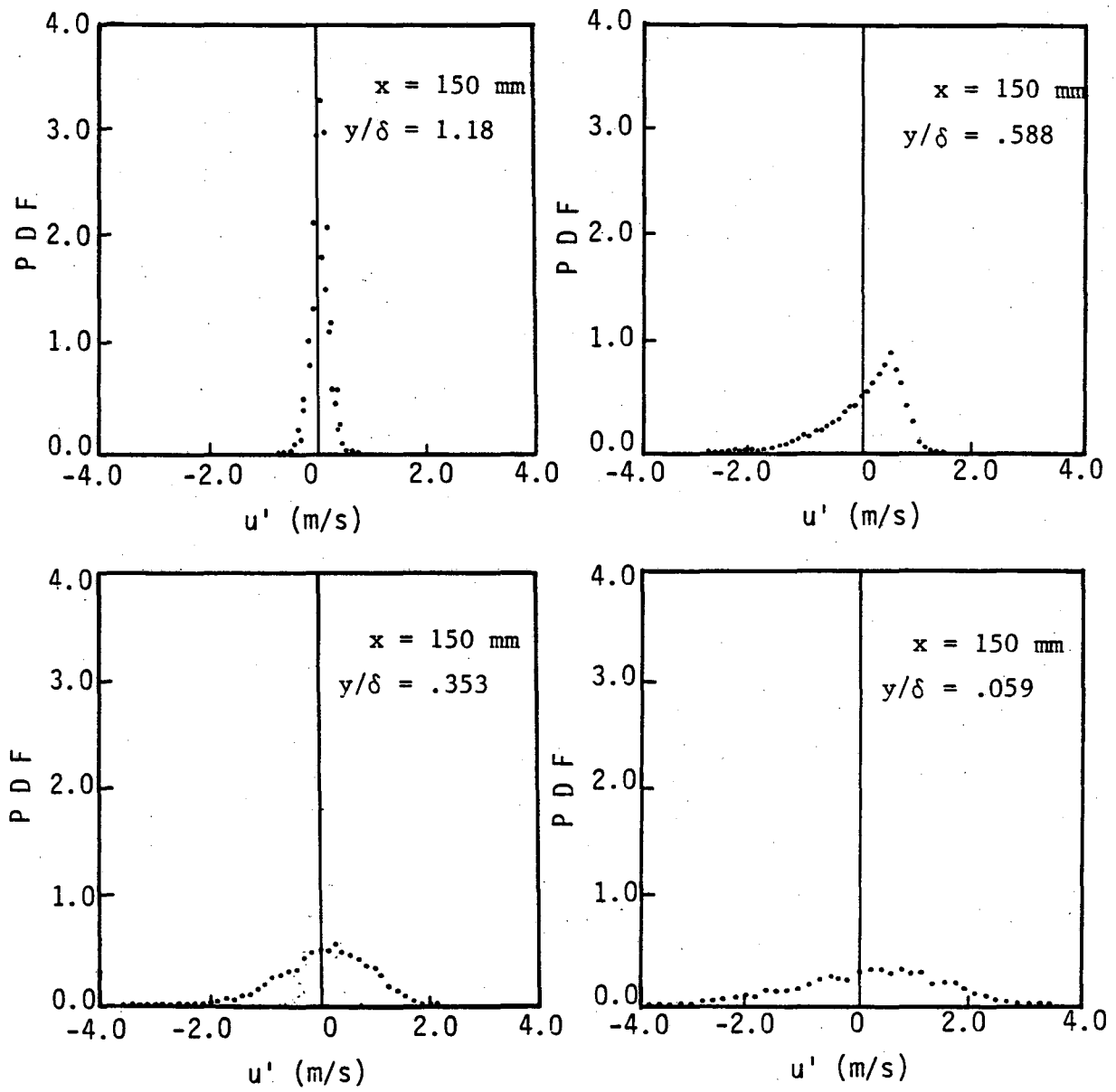
Fig. 59   Velocity PDF's of the Heated Boundary Layer at x = 150 mm
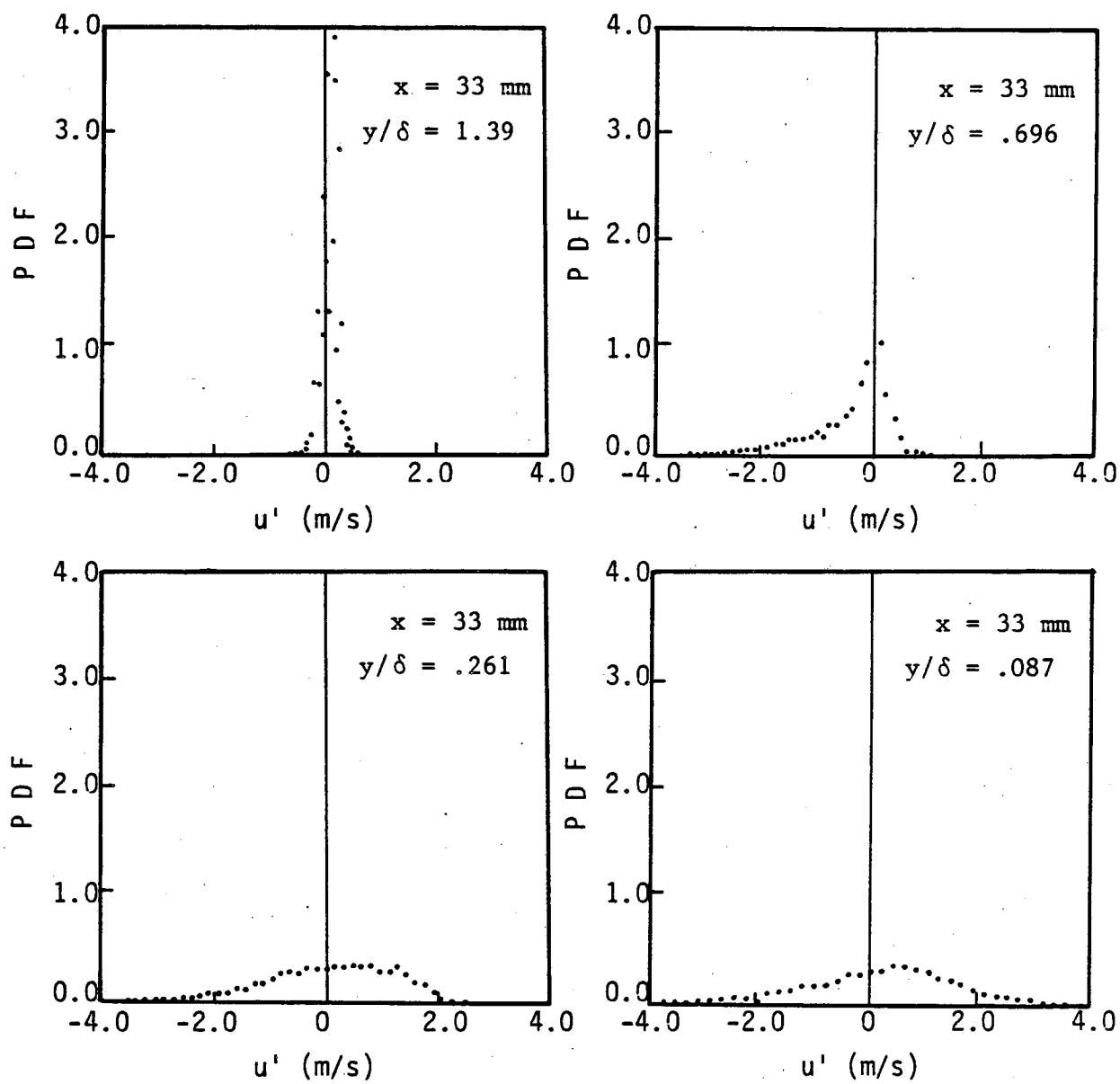
Fig. 60   Velocity PDF's of the Reacting Boundary Layer at x = 33 mm
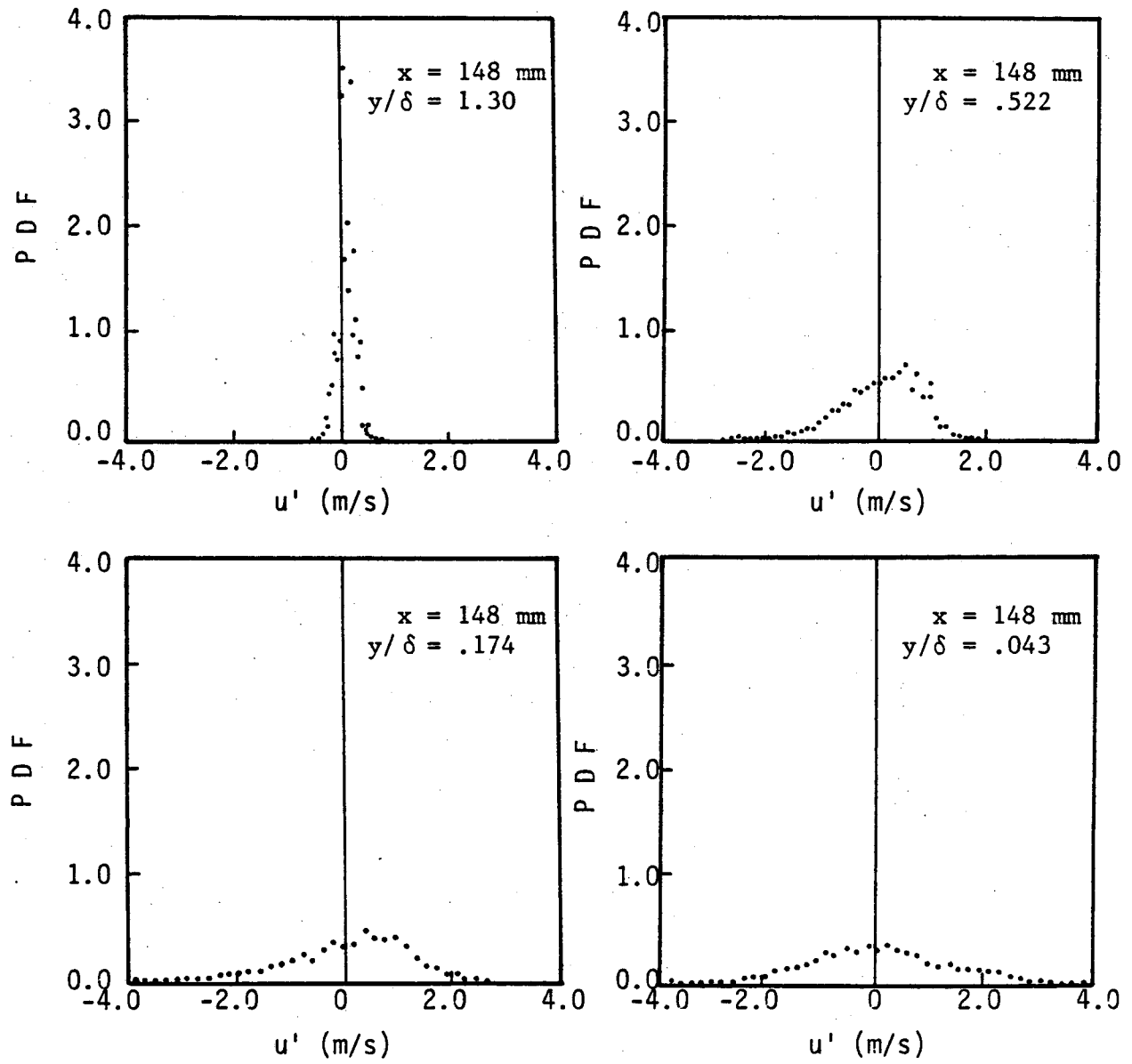
Fig. 61   Velocity PDF's of the Reacting Boundary Layer at x = 148 mm
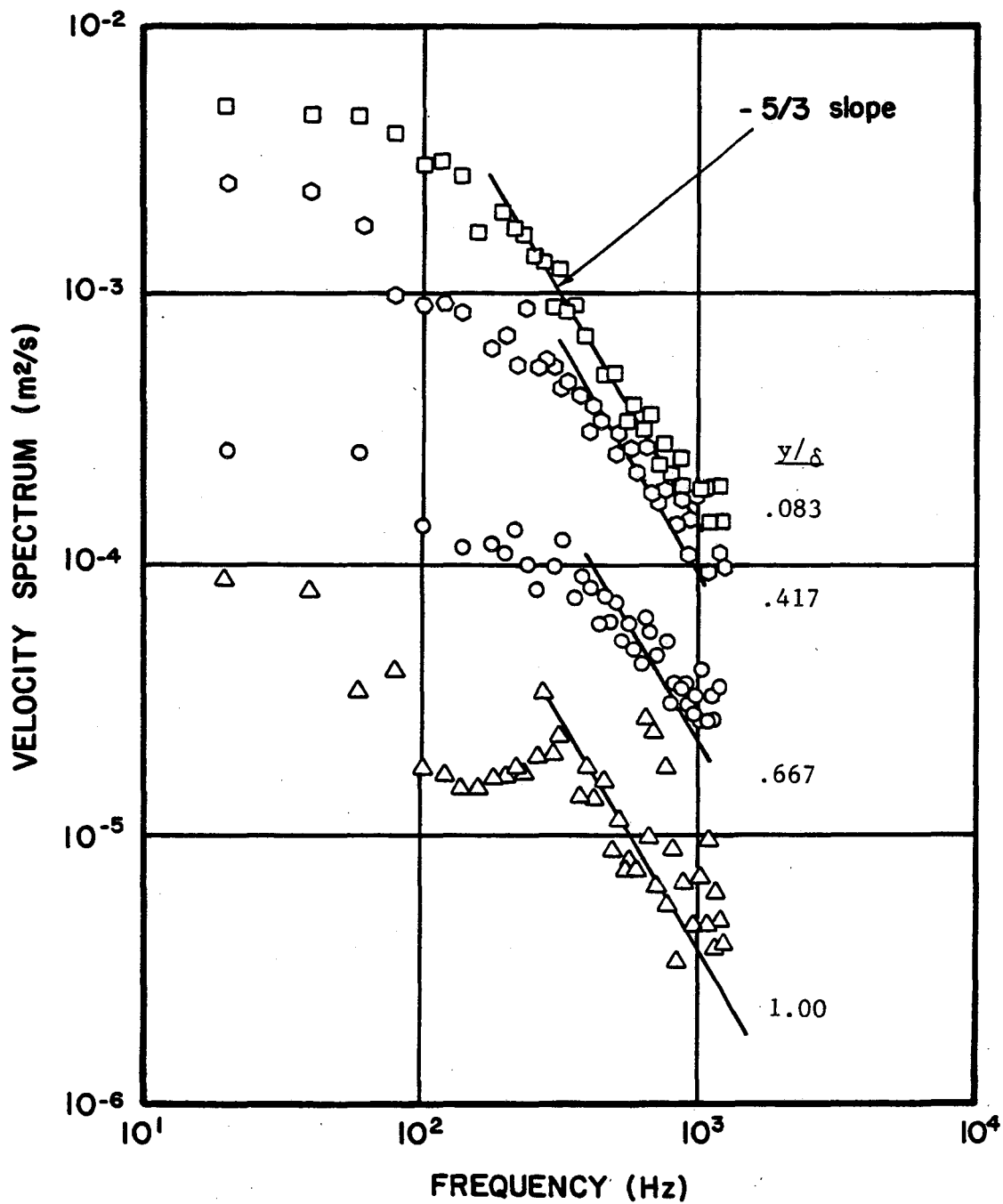
Fig. 62   Velocity Spectra of the Isothermal Boundary Layer at
x = 103 mm
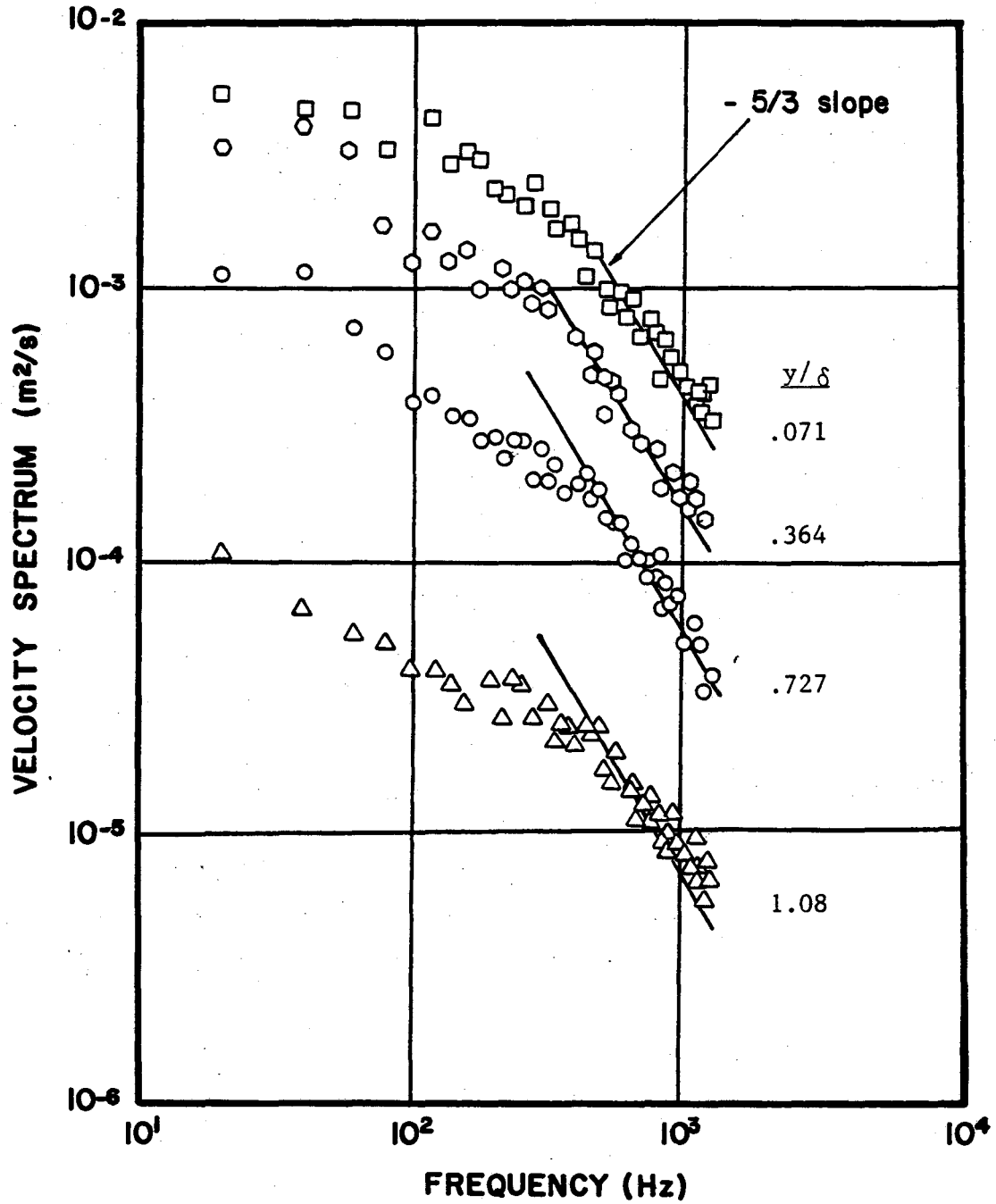
Fig. 63a   Velocity Spectra of the Heated Boundary Layer at
            x = 42 mm
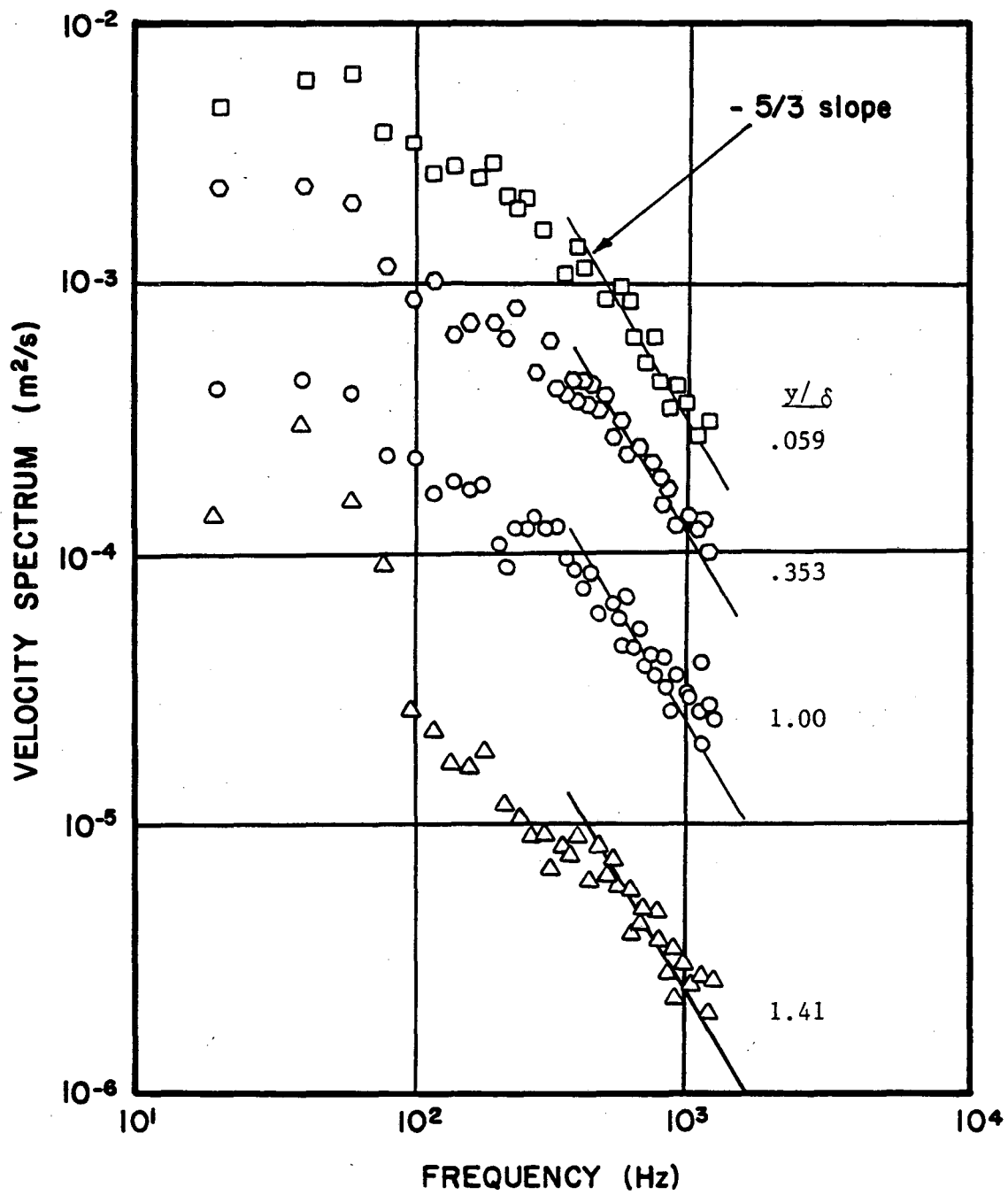
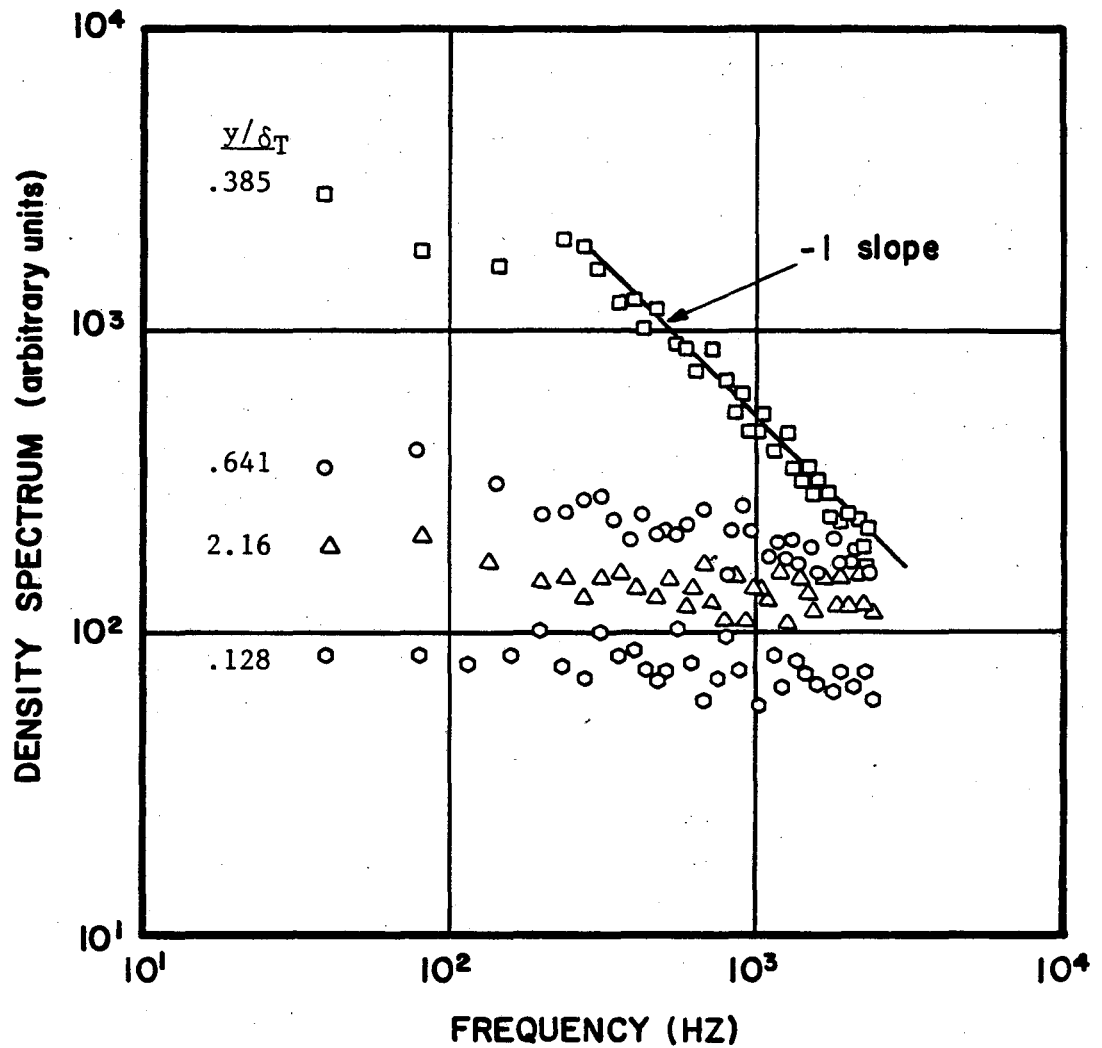Fig. 63b   Velocity Spectra of the Heated Boundary Layer at x = 150 mm
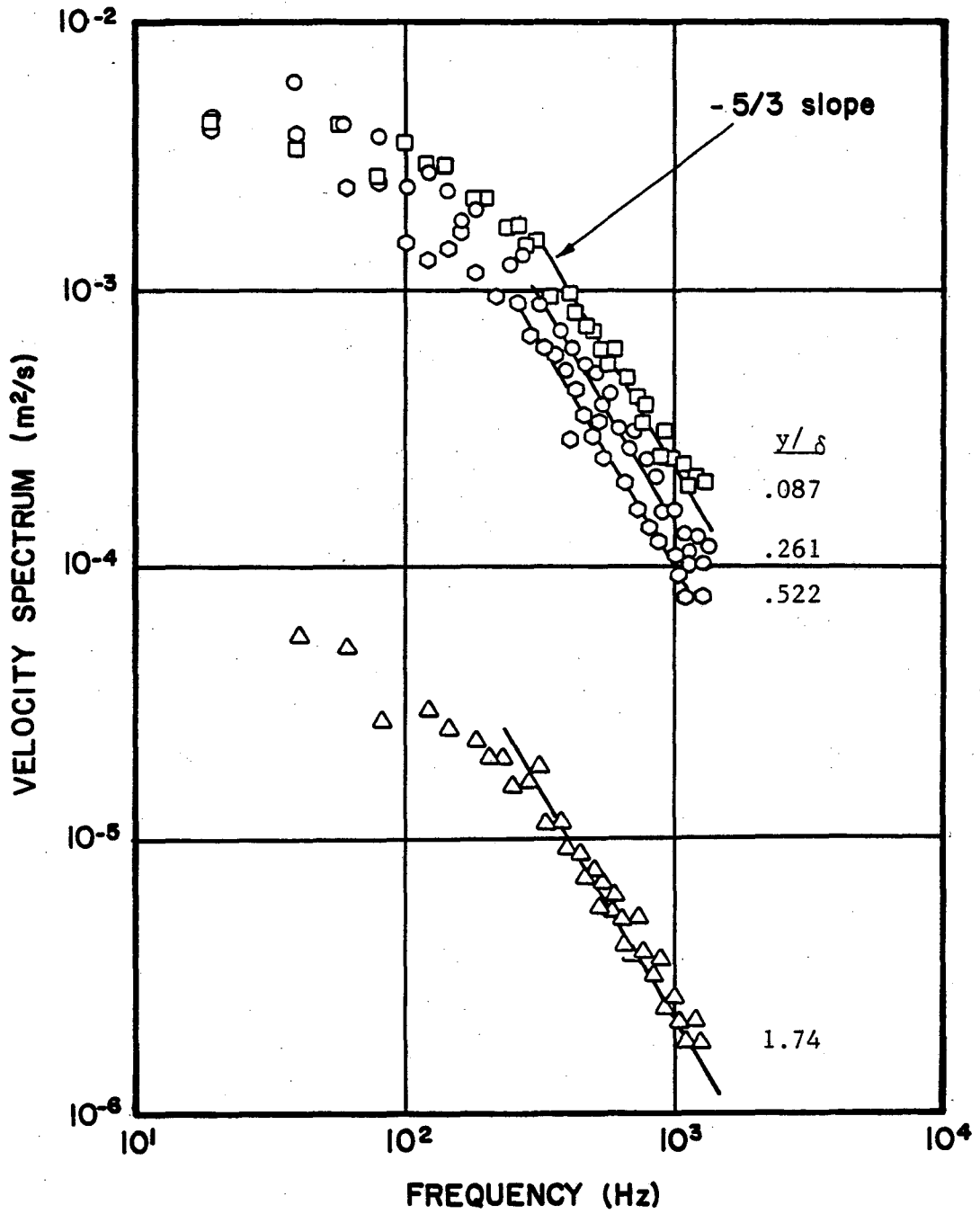
Fig. 64a   Velocity Spectra of the Reacting Boundary Layer at x = 33 mm
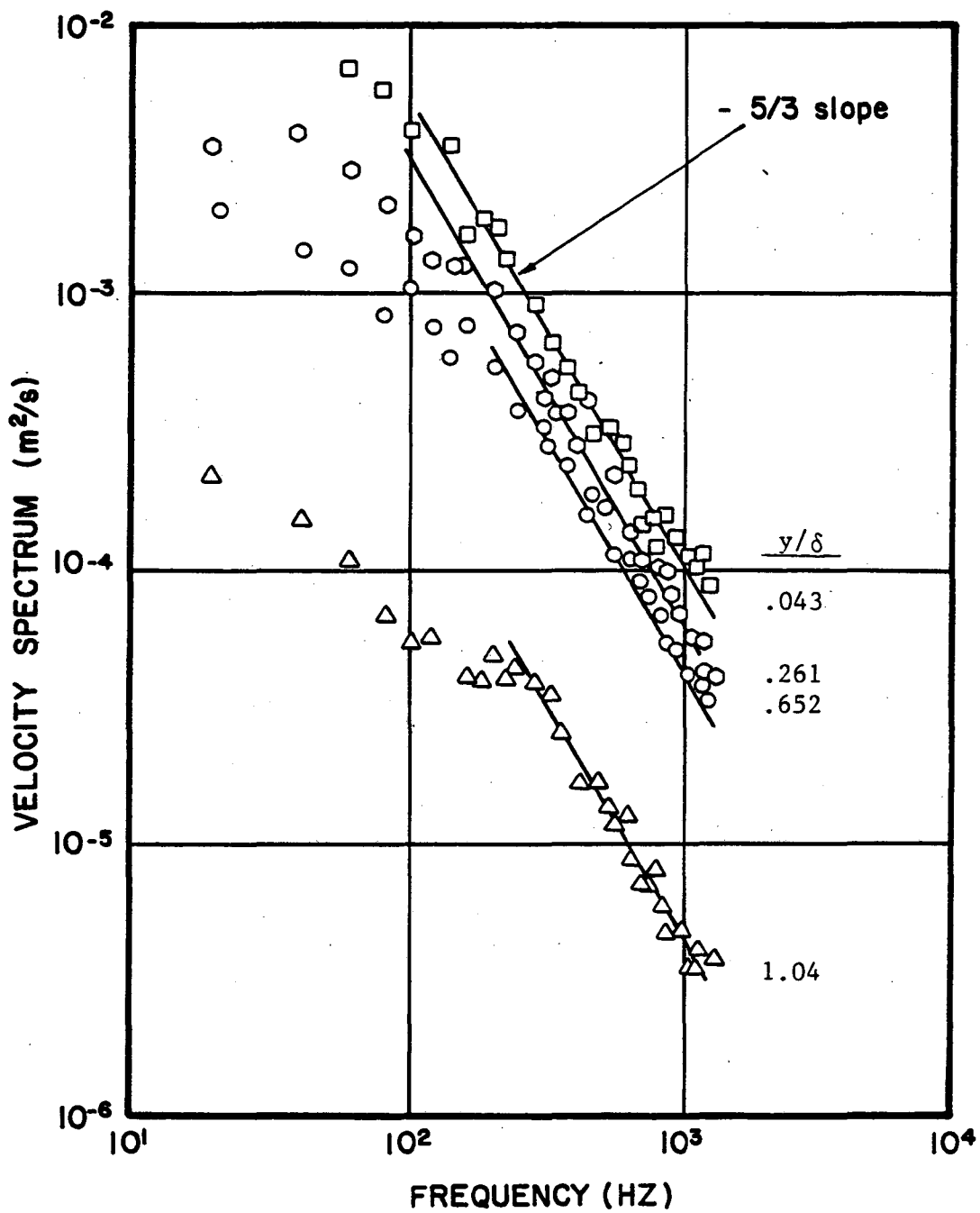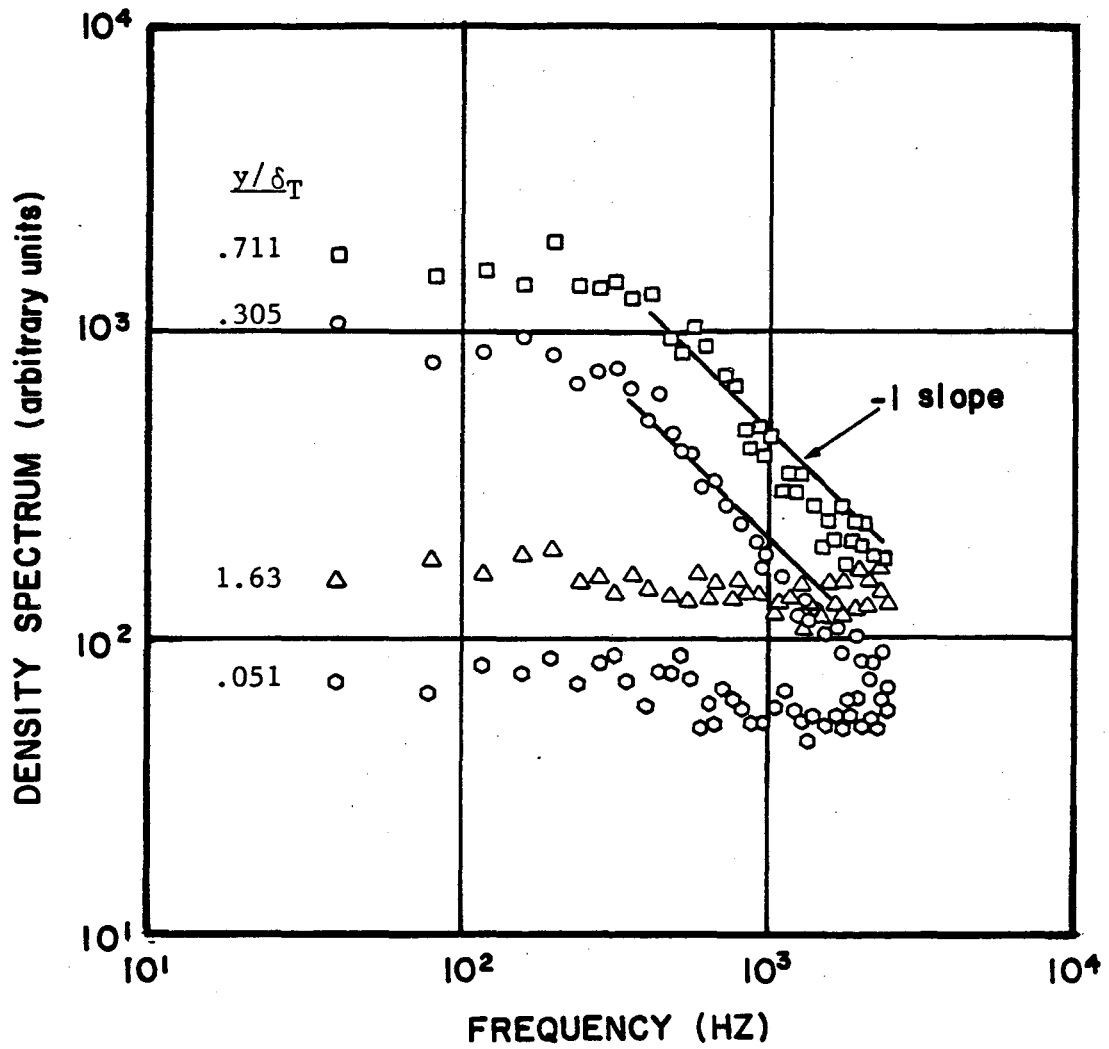
Fig. 64b   Velocity Spectra of the Reacting Boundary Layer at
            x = 148 mm
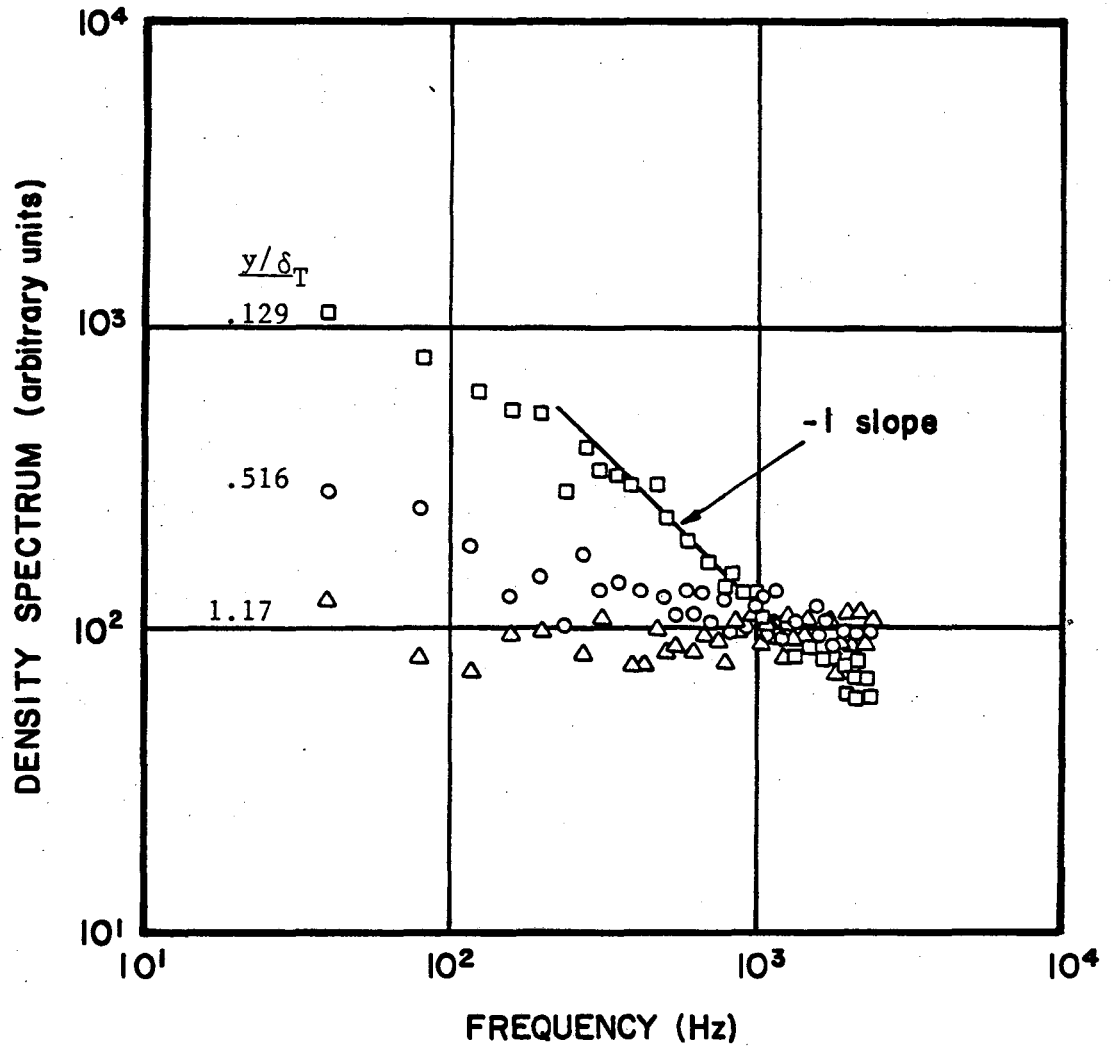
Fig. 65a   Density Spectra of the Heated Boundary Layer at
x = 42 mm
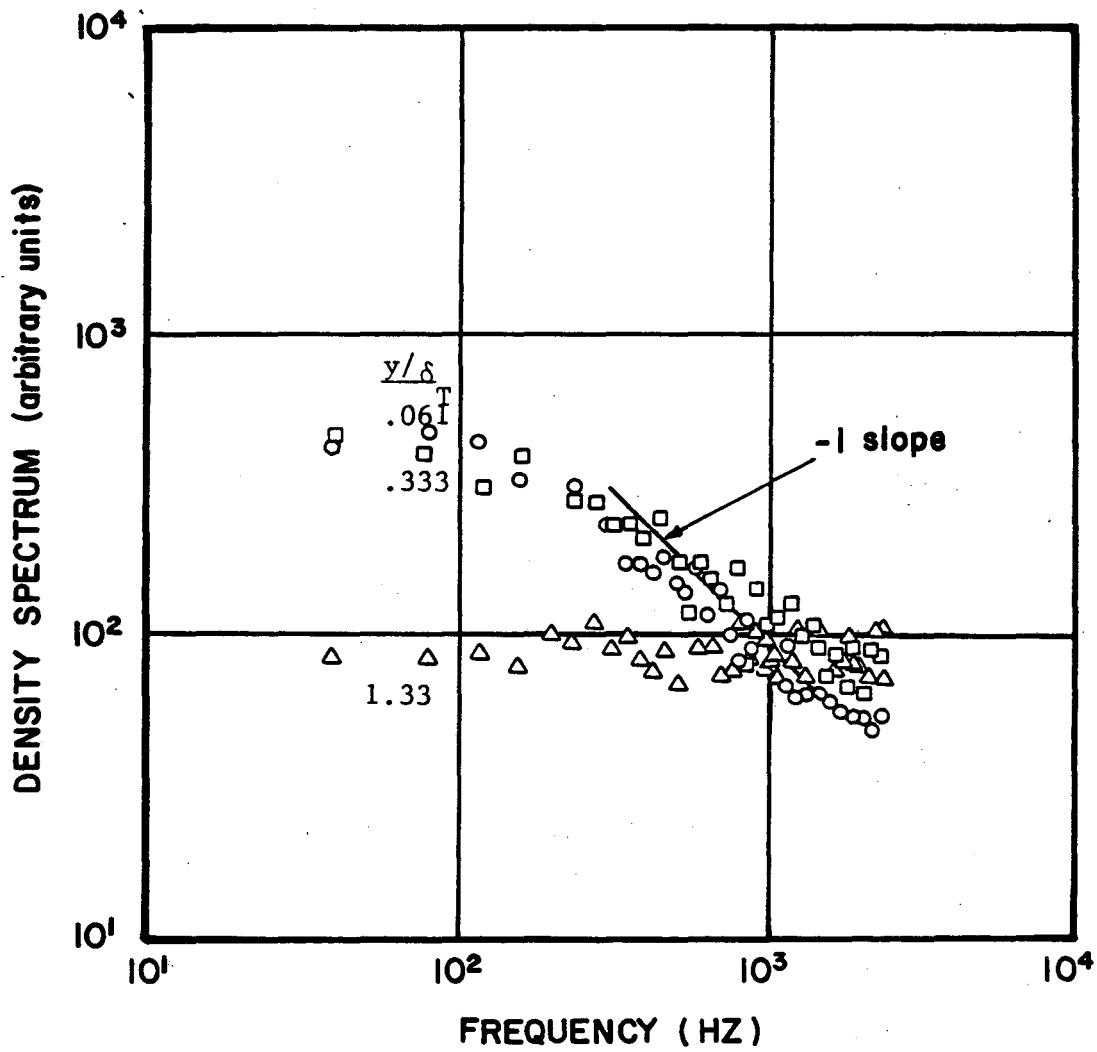
Fig. 65b   Density Spectra of the Heated Boundary Layer at
           x = 150 mm

Fig. 66a Density Spectra of the Reacting Boundary Layer at
x = 33 mm

Fig. 66b   Density Spectra of the Reacting Boundary Layer at
            x = 148 mm